RADAR POLARIZATION PROPERTIES AND LUNAR SECONDARY CRATERING

A Dissertation

Presented to the Faculty of the Graduate School

of Cornell University

In Partial Fulfillment of the Requirements for the Degree of

Doctor of Philosophy

by

Kassandra Martin-Wells

January 2013

RADAR POLARIZATION PROPERTIES AND LUNAR SECONDARY CRATERING

Kassandra Martin-Wells, Ph. D.

Cornell University 2013

Age dating of planetary surfaces relies on an accurate correlation between lunar crater size-frequency distributions and radiometric ages of samples returned from the Moon. For decades, it has been assumed that cratering records are dominated by "primary" impacts of interplanetary bolides [*McEwen et al*., 2005]. Unlike primary craters, secondary craters, which originate as ejecta from large primary events, occur in large clusters in both space and time. It was long believed that the majority of secondary craters formed at low velocities near their parent crater, resulting in a class of craters with morphologies which are easily distinguished from primary craters of a similar size [*McEwen et al.*, 2005]. However, recent work by *Bierhaus et al.* (2005), *McEwen et al.* (2005) argues that cratering records in the Solar System may be strongly contaminated by hard-to-identify secondary craters. They advise caution when relying on counts at small diameters [*McEwen et al*., 2005; *Bierhaus et al.*, 2005].

Despite the difficulties, something must be done to improve the accuracy of age dates derived from size-frequency distributions of small craters. In this thesis, a method of secondary crater identification based on radar circular polarization properties is presented. The radar polarization and photographic studies of lunar

secondary craters in this thesis reveal that secondary cratering is a widespread phenomenon on the lunar surface. Tycho and Copernicus secondary craters occur at non-negligible densities in and outside of obvious albedo rays and clusters for distances of many parent crater radii. Extreme caution should be used when counting small diameter lunar craters, as the level of secondary contamination can lead to overestimates in age of lunar surfaces with true ages of less than 1 Ga. Impact-initiated debris flows highlighted by the radar CPR reveal the significant role that secondary craters play in global surface modification and transport of local materials. The same is likely true on other airless bodies with substantial regoliths, such as Mercury. More work is needed to address these phenomena on bodies such as Mars, where impact cratering is not the only active geologic process.

BIOGRAPHICAL SKETCH

Kassandra was born in January of 1985 in the town of Rochester, Minnesota. She spent a very happy childhood with her family and friends—drawing, pretending, and exploring the woods behind her house. At age nine, she began golfing with her father, a passion which would lead to a successful high school and college career, including an individual berth in the NCAA Division Three National Championship. She graduated from Rochester Century High School in 2003 and went on to Carleton College, where she majored in Physics and Astronomy. At Carleton, she had the opportunity to research at the Arecibo and Parkes Observatories with Joel Weisberg, where she studied pulsars and the interstellar medium. Her interest in radar science and impact cratering began during a summer research internship at Cornell University, following which she made the decision to attend graduate school in planetary science. During the summer of 2011, Kassandra married the love of her life, Ross Martin-Wells, who received a PhD in Atomic and Molecular Optics from The Pennsylvania State University. They look forward to a long, happy life together.

When not investigating problems in planetary science, Kassandra is an avid writer, photographer, and amateur musician. She has been playing piano since the age of five and the guitar since fifteen. Recently, she has taken up the mandolin and will miss the sunny Saturday afternoons spent playing it in Cascadilla Park. Following graduate school, Kassandra has accepted a visiting professorship in Physics and Astronomy at her alma mater, Carleton College, where she will share her passion for science and the liberal arts with a new generation of students.

Every explosion has shrapnel.

—The Doctor

For my amazing family and friends.

I couldn’t have done this without you.

ACKNOWLEDGMENTS

I would like to thank my advisor, Don Campbell, for his guidance and assistance throughout my graduate career. I deeply appreciate your trust in my abilities, as well as the great freedom you've allotted me in my studies.

I would also like to acknowledge the assistance of Lynn Carter and Bruce Campbell, who have been valuable assets in all things radar remote sensing. Thank you, Lynn, for having been a great mentor to me. I've learned so much from our interactions. Thanks to Bruce for teaching me the ins-and-outs of radar observing and for our discussions on data processing. Someday, we will get three consecutive good days of S-band at the GBT. Special thanks to Jim Bell, both for sharing his LROC targeting access and for his invaluable guidance and support. Many thanks are also due to Martha Haynes for her career guidance and unwavering encouragement throughout my graduate career.

Finally, I would like to thank my family and friends for their incredible support and patience. In particular, I thank my husband, Ross, and my dear friend, Melina Blees. Without the two of you, this never would have been possible. My deepest thanks go out to my parents, Sandy and Jeff, for a lifetime of love and trust. You guys are the best. Thanks for believing in me.

TABLE OF CONTENTS

CHAPTER 1

INTRODUCTION

The impact craters which scar the surface of the Earth's moon represent one of the most complete records of our Solar System's bombardment history. Together with Mercury, the surface of the Moon is the type-example of a landscape shaped predominantly by impact cratering. Here, billions of years of impact-dominated modification offer clues not only into the impact process, but also the ways in which cratering shapes its surroundings, from regolith development to so-called "ballistic sedimentation" [*Oberbeck*, 1975]. In the case of the Moon, the information contained in the impact record is augmented by samples returned from its surface by the Apollo and Luna missions. With these samples, the relative surface ages derived from measurements of impact crater size-frequency distributions can be calibrated to an absolute scale. It is the radiometric ages of lunar impact crater materials, ascertained from these samples, which provide the basis for all absolute age-dating in our Solar System [*Melosh*, 1989].

For this reason, the lunar impact record has taken on special significance. Any inaccuracies in the conversion from the measured absolute age to lunar crater size-frequency, or in the conversion from that size-frequency distribution to the underlying impactor flux, have compounded repercussions on the absolute chronologies of other terrestrial bodies in our Solar System [*Bierhaus et al.*, 2005; *McEwen et al.*, 2005]. One of several outstanding questions pertaining to this conversion process is the influence of secondary cratering on the overall lunar cratering record. Unlike primary

craters, which form when a bolide from space impacts a planetary surface, the fragments which excavate secondary craters originate as ejecta thrown ballistically from larger craters. In his preliminary work studying lunar crater distributions, Eugene Shoemaker identified these two populations of craters [*Shoemaker,* 1965]. Impact crater populations are often expressed in size-frequency distributions (SFDs), where crater size is plotted against crater frequency [*Crater Analysis Techniques Working Group*, 1975]. *Shoemaker* (1965) found that the cumulative SFDs of primary and secondary craters expressed different slopes when plotted in log-log space. Craters above a few kilometers in size exhibited a shallow slope ($b \sim -2.0$; the "primary" branch), while smaller craters plotted with a much steeper slope ($b \sim -4.0$; the "secondary" branch) [*Shoemaker*, 1965]. The exact cut-off diameter varied depending on location, but it was generally observed around 1 km in crater diameter [*Shoemaker*, 1965]. Shoemaker hypothesized that secondary craters dominated the lunar cratering record below a diameter of about 200 m [*Shoemaker*, 1965]. He attributed the steepening of the lunar SFD between about 200 m and 1 km to an undetermined population of small, steep-sloped primary craters [*McEwen et al.*, 2005]. The exact location and cause of this kink in the lunar SFD remains an open topic of research. Part of the difficulty in answering what appears to be a simple question is, as we will see, the inherent challenge in discerning between secondary and primary craters in this size range.

Since the early work in the Apollo era, crater counting and classification has become increasingly important. Shoemaker's hypothesis concerning the origin of the steep "secondary" branch has come under scrutiny. Some workers [*McEwen et al.*,

2005; *Bierhaus et al.*, 2001; *Bierhaus et al.*, 2005; *Hurst et al.*, 2004] claim that secondaries dominate this portion of the cratering record, while others suggest that secondary contamination of the steep branch is minimal [*Werner et al.*, 2009]. *Dundas and McEwen* (2007) investigated the density of distal Tycho craters in rays in Mare Cognitum and near Ptolemaeus crater and estimated that Tycho produced at least 10^6 secondary craters with diameters greater than 63 m. They stressed that this is a lower-limit on secondary crater production since it did not include secondary craters between or beyond albedo or compositional rays [*Dundas and McEwen*, 2007]. Work on Mars [*McEwen et al.*, 2005; *Preblich*, 2005] and Europa [*Bierhaus et al.*, 2001; *Bierhaus et al.*, 2005] suggests that populations external to obvious rays may dominate the secondary crater production of any given primary event. An order of magnitude more secondary craters belonging to the small, rayed martian crater Zunil lie between obvious rays than in them, out to distances of 700 km [*Preblich*, 2005]. Three times more secondary craters can be found beyond these rays entirely (distances >700 km) [*Preblich*, 2005].

Because they do not represent the flux of interplanetary bolides, the presence of so many secondary craters in the impact record can result in either an over or under-estimation of surface age. Assuming accurately calibrated lunar isochrons—the size-frequency functions that link crater counts to absolute ages—the inclusion of many additional craters to a given surface creates an artificially elevated crater density, corresponding to a measured age which is older than the true age [*McEwen et al.*, 2005]. Alternatively, the isochrons themselves may be contaminated by unidentified secondary craters. In this case, the crater density corresponding to a given absolute

age is artificially high [*McEwen et al.*, 2005]. Ages computed using such isochrons will be younger than the true age for surfaces with few or no secondary craters.

Because of the potential for secondary craters to affect ages measured using impact crater size-frequency distributions, it is important to be able to distinguish between primary and secondary features. However, this is a more difficult task than it may at first appear. As Melosh points out in his treatise, *Impact Cratering: A Geologic Process*, teasing details about the projectile and impact conditions from the morphology of an existing crater can be a challenge:

> The near-independence of the final crater's shape, size, etc., from the details of the energy source means that parameters such as the impactor's velocity, mass, or even angle of impact (within broad limits) cannot be separately determined from the final crater. This is either a blessing or a hindrance, depending upon whether one is interested in the final crater or the initial projectile [*Melosh*, 1989, pg. 49].

This property has allowed workers to draw important conclusions about the impact process that might have been difficult if final crater morphologies were more sensitive to impact conditions [*Melosh*, 1989]. However, many of the details of the collision are masked by the inherent symmetries of the shock-dominated excavation process, an inconvenient truth when it comes to determining whether a given impact has a primary or secondary origin. There are, however, a handful of things we can say about primary vs. secondary formation and how differences in these processes are reflected in the resulting craters. First, the impact velocities of primary craters can be very great, bounded on the minimum end by the escape velocity of the target body and exceeding speeds of 40 km/s for cometary impacts in the inner Solar System [*Melosh*, 1989]. In contrast, the impact velocity of a secondary crater cannot exceed the target

body's escape velocity, or its genetic ejecta fragment will become unbound from the planet's gravitational well and its trajectory would not re-impact with the surface [*Melosh,* 1989]. Because they inhabit the low range of the velocity spectrum, secondaries represent lower energy impacts than most primary craters. Impact energy is a dominant factor in shaping crater morphology, so many secondary craters exhibit a unique appearance by which they may be identified [*Shoemaker,* 1965; *Melosh,* 1989]. These morphologies include high ellipticities, shallow profiles, tendency to form in clusters, and the presence of "herringbone" or chevron-shaped ridges pointing back toward the primary [*McEwen et al.,* 2005; *Pike and Wilhelms,* 1978; *Oberbeck and Morrison,* 1973].

Unfortunately, the generalization that secondary craters represent low-energy events with their own unique morphologies may not hold in all cases. Very distal secondary craters impact the surface near the escape velocity of the target body [*Melosh,* 1989]. The morphology of such craters may be more like those of small primary craters than secondary craters within a few crater radii of their parent events [*Bierhaus et al.,* 2005]. Distal secondary craters are also more circular than "traditional" secondary craters [*McEwen et al.*, 2005]. *Bierhaus et al.* (2005) and *McEwen et al.* (2005) claim that the majority of distal secondary craters identified in their work are "background" events that would not be identified as secondary craters based on morphology due to the high velocity of their impacts. *McEwen et al.* (2005) estimated that up to 96% of secondary craters are "background" events, occurring at ranges greater than 35 crater radii from their parent. Due to their elevated impact velocities, these events lack the characteristic "secondary" morphologies that allow

proximal secondary craters to be identified and removed from crater counts. Despite the difficulty in our ability to identify potentially large numbers of distal secondary craters using photographic morphologies, alternative identification methods do exist. Both *Bierhaus et al.* (2005) and *McEwen et al.* (2005) report spatial clustering among their secondary craters, compared to a truly isotropic distribution of events. Several workers have investigated the potential for using spatial clustering as a method of secondary crater identification [*Bierhaus et al.*, 2005; *Robbins and Hynek*, 2011].

Robbins and Hynek (2011) used a combination of THEMIS Daytime IR and CTX images to identify 10^4 secondaries with D < 800 m associated with the large martian primary Lyot (D = 222 km). In this study, craters were marked as potential members of a cluster if their fifth-nearest neighbor was within a distance of 10 crater radii. Clusters with orientations along great circles of Lyot were determined to be Lyot secondaries. The slopes of the size-frequency distributions of these craters were consistent with secondary craters. *Robbins and Hynek* (2011) determined that improper inclusion of these craters in primary size-frequency distributions would result in non-negligible overestimates of surface age. Like the work of *Bierhaus* (2005) and *McEwen et al.* (2005), this finding emphasizes the importance of quantifying secondary contamination in any study of surface age derived from crater counts. Unfortunately, given the great travel times of the ejecta fragments which form distant secondary craters, these fragments may experience lateral dispersion during flight, reducing secondary crater clustering [*Bierhaus et al.*, 2001]. Therefore, it is unclear what percentage of the total number of secondary craters are members of clusters. Despite these and other recent studies of distal secondary craters, the limited

number of methods for identifying small secondary impacts formed at high velocity continues to make it difficult to quantify the true extent of contamination of primary cratering populations by secondary events.

Luckily, measurements of the polarization properties of radar echoes can provide additional information that can be used to identify secondary craters that may evade detection with other methods. A unique radar polarization signature has been observed in association with lunar secondary craters at large distances from their parent primary craters [*Wells et al.,* 2010]. The secondary craters in this study did not exhibit traditional "secondary" morphologies on the 100 m/pixel scale (such as elliptical planforms, spatial clustering, or chevron-shaped dunes), only distinctive radar circular polarization ratio (CPR) enhancements in the downrange direction. In this context, downrange is defined as the direction away from the parent crater.

Radar CPR is a measure of the ratio between the power received in the same sense of circular polarization as transmitted to that in the opposite sense echo as transmitted. It can be used as a proxy for roughness on the scale of the radar wavelength, with rougher surfaces returning higher values of CPR [e. g., *Campbell and Campbell*, 2006]. This signature is present at 13-cm and 70-cm in Arecibo-Green Bank Telescope bi-static radar observations of the lunar near side, though it features more prominently at 13-cm. In this thesis, I will outline the properties of this radar circular polarization signature and describe how it can be used in combination with other methods to identify secondary craters. The radar CPR identification method is introduced in the second chapter, much of which has been adapted from *Wells et al.*, 2010.

Because it appears to be sensitive to distal secondary craters, which are difficult to identify with other methods, this radar polarization method has the potential to improve our understanding of the total number and distribution of secondary craters produced by a given primary event. In this thesis, I will use the radar polarization method to measure the total secondary crater production of Tycho crater (D=86 km) and Copernicus crater (D=93 km). These are two of the largest rayed lunar craters, with ages of ~100 Ma and 800 Ma, respectively [*Arvidson et al.*, 1976; *Bogard et al.*, 1994]. Their young ages means that the secondary crater networks of these primary events remain well-preserved, providing a reliable record of total secondary crater production. The ray systems of these craters have also been studied by numerous other workers [e.g., *Shoemaker*, 1965; *Pieters et al.*, 1985; *Vickery*, 1986; *Campbell et al.*, 1992; *Hirata and Nakamura*, 2005; *Dundas and McEwen*, 2007; etc.], so ample room for comparison exists. I will use the radar CPR method to characterize the number density of secondary craters as a function of range from the parent crater. In turn, this number density can be used to extrapolate the total secondary crater production, as well as compute the cross-over diameter as a function of distance. The cross-over diameter is defined as the size below which the local SFD will be dominated by secondary craters [*McEwen et al.*, 2005]. It has been shown to vary with terrain age [*McEwen et al.*, 2005], and should also change with distance from the largest primary crater contributing secondary craters to the SFD.

In addition to its relevance to Solar System chronologies, secondary cratering also plays an important role in the formation of crater rays and, therefore, global surface modification of airless bodies such as the Moon and Mercury. During the last

fifty years, numerous studies have addressed the important questions surrounding lunar rays and other impact-related surface features, including the formation, erasure, and retention mechanisms of high-albedo rays; the mixing ratios of primary vs. local material along rays; the total volume and thickness of ray deposits; and the origin of unusual morphologies (i.e., flow fronts, braided textures, light-colored mantling deposits, and smooth inter-crater plains) often associated with rays [e.g., *Oberbeck*, 1975; *Morrison and Oberbeck*, 1976; *Lucchitta* , 1976; *Pieters et al.*, 1985; *Campbell et al.*, 1992; and *Hawke et al.*, 2004]. But what is the importance of lunar rays? *Dundas and McEwen* (2007) mapped 560,000 km^2 of Tycho rays. The Copernicus ray system is also extensive [e. g., *Pieters et al.*, 1985; *Campbell et al.*, 1992]. As the albedo-bright rays of Tycho and Copernicus craters reveal, impact crater rays can stretch for thousands of kilometers from their parent crater [*Dundas and McEwen*, 2007]. Over the large distances that high-albedo rays stretch, they play an important role in the modification of the local surface. Rays result from the deposition of primary material and the reworking of the local surface, both adding to and subtracting from existing features [e. g., *Oberbeck*, 1975; *Pieters et al.*, 1985; *Campbell et al.*, 1992; and *Hawke et al.*, 2004]. Because rays represent the transport and intimate mixing of primary and local materials across the surface of the Moon, it is important that we understand the ratios of this mixing and its effect on regolith development and the erosion of the crater record. Specifically, workers have been interested in the deposition mechanisms of rays, the ratio of primary to local materials in rays, and their thickness and longevity.

Detailed investigations of lunar rays began during the Apollo era, when workers made use of high-resolution optical images taken by Ranger and the Apollo missions to explore rays in detail for the first time [e.g., *Shoemaker*, 1965; *Oberbeck*, 1975]. Among these workers was Eugene Shoemaker, whose pivotal role in framing the secondary crater contamination problem has already been discussed. Verne Oberbeck also extensively studied lunar cratering during this era. Oberbeck posited the theory of ballistic sedimentation, a process by which ejecta fragments scour local surfaces upon impact, intimately mixing primary and secondary materials in the resulting ray deposits and initiating "debris surges" [*Oberbeck*, 1975; *Morrison and Oberbeck*, 1975]. These surges of local materials follow the primary ejecta curtain in a ground-hugging flow and produce light-mantled smooth plains [*Oberbeck*, 1975]. In Oberbeck's original interpretation of ballistic sedimentation, mixing was initiated by the impact of large, intact ejecta blocks [*Oberbeck*, 1975]. However, this mechanism leads to a dearth of primary ray material compared to what has been measured by more recent investigations [*Campbell et al.*, 1992]. *Schultz and Gault* (1985) noted that these large spall-blocks may fracture easily during ballistic flight, resulting in "swarms" of smaller impacting blocks, a mechanism which greatly increases the percentage of local ray materials. In practice, ballistic sedimentation is likely a combination of these two end-member processes [*Campbell et al.*, 1992].

In the intervening years since these initial studies of secondary crater morphologies, workers have made use of a variety of datasets to examine lunar rays. *Pieters et al.*, (1985) used ground-based telescopic IR spectrometry to observe the mineral composition of several Copernicus rays. They were able to roughly constrain

the thickness of the Copernican rays emplaced on Mare Imbrium based on the presence of "dark-haloed" craters puncturing the ray deposits [*Pieters et al.*, 1985]. Dark-haloed craters are impacts which have excavated through the lighter ray material into the mare basalts below and ejected these materials as a dark ring or "halo" surrounding their continuous ejecta. As simple lunar craters can be expected to excavate to ~1/10 of their transient diameter, measuring of the size of each dark-haloed feature constrains the maximum thickness of the ray in that locality [*Melosh*, 1989].

Hawke et al. (2004) also studied lunar rays in order to understand the origin and duration of their HIGH albedos. They identified two endmember categories of lunar rays: maturity rays and compositional rays [*Hawke et al.*, 2004]. Compositional rays are the result of a difference in composition between primary ray material and the surrounding local material, for example, when rays from a highlands target extend across a mare surface [*Hawke et al.*, 2004]. Maturity rays, on the other hand, are the result of immature material exposed on the surface due to the impact of primary ejecta and the formation of secondary craters. This immature material is brighter in albedo than materials which have been exposed to space weathering conditions for long periods of time [*Hawke et al.*, 2004]. Compositional rays require a larger percentage of primary material in the resulting ray, but are longer-lived than maturity rays, which darken when exposed to cosmic radiation [*Hawke et al.*, 2004]. Most rays are likely to be some combination of these two classes, with the precise mechanisms for primary ejecta transport and intimate mixing between the ejecta and local surface influencing the end result [*Hawke et al.*, 2004]. Therefore, it is important to

understand the role of secondary cratering in the creation of these rays. In this thesis, I investigate the origin of the radar CPR enhancements observed in association with lunar secondary craters and discuss the implications for transport and mixing of primary ejecta with local materials. Using a combination of radar polarization data and high-resolution LROC NAC photographs, I characterize common surface morphologies in areas of radar CPR enhancement. This investigation reveals that debris flow deposits are strongly correlated with the presence of enhanced radar CPR at both clustered and isolated lunar secondary craters. The frequency of these debris flows across the lunar nearside indicates that not only are reworked local materials an important contributor to the formation of high-albedo rays, but also that debris flow plays a more prevalent role in the erosion and modification of the lunar surface than previously believed.

In summary, then, the intimate details of the lunar impact cratering record have important implications in far-reaching corners of planetary science. Questions about the dominance of primary and secondary craters at small diameters are relevant to the ages of young surfaces and surfaces of limited spatial extent throughout the Solar System [e. g., *Bierhaus et al.,* 2005; *McEwen et al.,* 2005]. Large, well-preserved lunar ray systems such as those of Tycho and Copernicus crater provide laboratories in which total secondary crater production and the role of secondary cratering in the ray formation process can be studied [e. g., *Campbell et al.,* 1992; *Hawke et al.,* 2004]. By investigating the correlation between fresh lunar secondary craters and radar CPR enhancements, this thesis aims to address these and other outstanding questions about the role of secondary cratering in the lunar environment.

CHAPTER 2

RADAR CPR ENHANCEMENTS AT DISTAL LUNAR SECONDARY CRATERS

2.1 Introduction

One of the outstanding questions about the dominance of primary vs. secondary craters at small diameters on the Moon is whether most secondary craters have morphologic characteristics by which they can be distinguished from primary craters. In the introductory chapter, we briefly discussed the ways in which secondary craters are different from primary craters. On a crater-by-crater basis, there are a number of ways secondary craters which form at low energies can be distinguished from primary craters [*Melosh*, 1989]. Because of their low impact energies, the shock wave and subsequent release wave that dominate the excavation process of higher-velocity primary craters are less important for secondary craters near their parent crater [*Melosh*, 1989]. It is the symmetry of the shock and release waves that create the exceptionally circular planforms of most primary craters [*Melosh*, 1989]. Statistical studies of impact crater shape on the Moon reveal that crater planform shapes are remarkably insensitive to impact angle, with craters retaining an overall circular shape down to near grazing incidence angles of $\theta < 15°$ from the horizontal [*Herrick and Forsberg-Taylor*, 2003]. It is worth noting that the highest velocity ejecta of any impact will be most sensitive to the obliquity of the impact angle [*Melosh*, 1989]. This is because high-velocity ejecta (including melted and vaporized materials) is produced very early in the cratering process, when the initial coupling of

the projectile and target energy occurs [*Melosh*, 1989]. Therefore, the effects of obliquity appear at higher incidence angles for ejecta facies and impact melt than for the crater shape itself. *Herrick and Forsberg-Taylor* (2003) found that crater ejecta blankets began to exhibit uprange notches or zones of avoidance at θ=30°, with a downrange notch also appearing at θ=20°, resulting in a "butterfly" ejecta morphology, symmetric across the impact direction.

The planform shapes of proximal secondary craters are a different matter. Because of the lower impact velocities, they are much more sensitive to impact conditions, such as impact angle. The primary ejecta fragments that form secondary craters move away from the parent crater in an inverted cone shape called the ejecta curtain [*Melosh*, 1989]. The material at the base of the ejecta curtain is comprised of the lowest velocity ejecta, with higher-velocity ejecta further up in the cone [*Melosh*, 1989]. The result is that proximal secondary craters not only form at low velocity, but also at impact angles much lower than the θ=45° average impact angle of primary craters. For this reason, proximal secondary craters have very distinct morphologies. Workers who first studied proximal secondary crater morphologies in high resolution photographs reported that secondary craters were shallower than primary craters, with elliptical planforms [e.g., *Shoemaker*, 1965; *Oberbeck*, 1975; *Morrison and Oberbeck*, 1975; *Lucchitta*, 1976]. They also observed characteristic uprange (in the direction of the primary impact) dunes at many of the secondary craters. These dunes formed v-shapes that circumscribed the crater rim, with the points of the v's oriented in the direction of the parent crater [*Morrison and Oberbeck*, 1975; *Lucchitta*, 1976]. Laboratory experiment with high-speed guns revealed that similar dunes formed when

two craters formed simultaneously or in very quick succession along the same impact direction [*Morrison and Oberbeck*, 1975]. Because of the thickness of the ejecta curtain in proximal regions, these secondary craters are often found in linear clusters extending along the radial direction, the same conditions which gave rise to these dunes in the laboratory setting. *Morrison and Oberbeck* (1975) also proposed that debris surge, a high-velocity flow of material following the ejecta curtain along the surface, could contribute to these dunes, as well as fill low-laying areas. In addition to these v-shaped, "chevron" or "herringbone" dunes, secondary crater clusters were often observed to create areas of "disturbed" terrain downrange from the craters [*Lucchitta*, 1976]. These disturbed terrains are composed of numerous, sub-parallel v-shaped ridges, sometimes called "braided" terrains.

As we discussed earlier, *Shoemaker* (1965) identified a steep-sloped population of craters below about 1 km in diameter in lunar crater size-frequency distributions. Of this population, he hypothesized that secondary craters were dominant below about 200m [*Shoemaker*, 1965]. For the next few decades, workers largely ignored the problem of secondary contamination of crater counts for age-dating, however, because it was believed that the majority of secondary craters occurred near their parent craters or in obvious clusters and could thus be easily removed from counts on a case-by-case basis as needed [*McEwen et al.*, 2005].

However, *Bierhaus et al.* (2005) reported that large numbers of secondary craters belonging to the crater Pywll on Jupiter's satellite Europa actually were found at great distances from the parent crater. *McEwen et al.* (2005) reported similar finding for the 10.0 km diameter martian crater, Zunil. They estimated that up to 96%

of all Zunil secondary craters occurred at distances greater than 400 km from the parent crater [*McEwen et al.*, 2005]. These studies have rekindled the community's interest in the issue of secondary contamination.

In their study, *McEwen et al.* (2005) used a unique nighttime IR signature of what appear to be Zunil rays to identify otherwise morphologically unremarkable secondary craters. Other workers have used DEMs to identify secondary craters based on their shallower depth to diameter ratios than the primary crater value of d/D~0.2 [*Robbins and Hynek*, 2011]. Spatial clustering along great circles from large primary craters has also been utilized to identify secondary craters [*Robbins and Hynek*, 2011]. Until such a time as we can accurately model the secondary crater production and distribution of individual primary craters, it is important to continue looking for more inclusive methods of secondary crater identification.

In this vein, I present 20-m resolution, SC (same sense of circular polarization as transmitted) and 100 m resolution circular polarization ratio (CPR), 13 cm radar images of the floors of lunar craters Newton (D=79 km; 76.7° S, 16.9° W) and Newton-A (D=64 km; 79.7° S, 19.7° W). These regions are not within an optical ray, but just beyond a prominent Tycho ray stretching across Clavius crater (Figure 2.1). However, many small craters on the floors of Newton and Newton-A display distinctive ejecta blankets with prominent CPR asymmetry downrange from Tycho crater (D=85 km; 43.3° S, 11.2° W) (Figure 2.2), suggesting they are secondary craters belonging to that primary. The density of these secondary craters, as well as the orientation of their ejecta blankets, is consistent with the optical ray and may represent

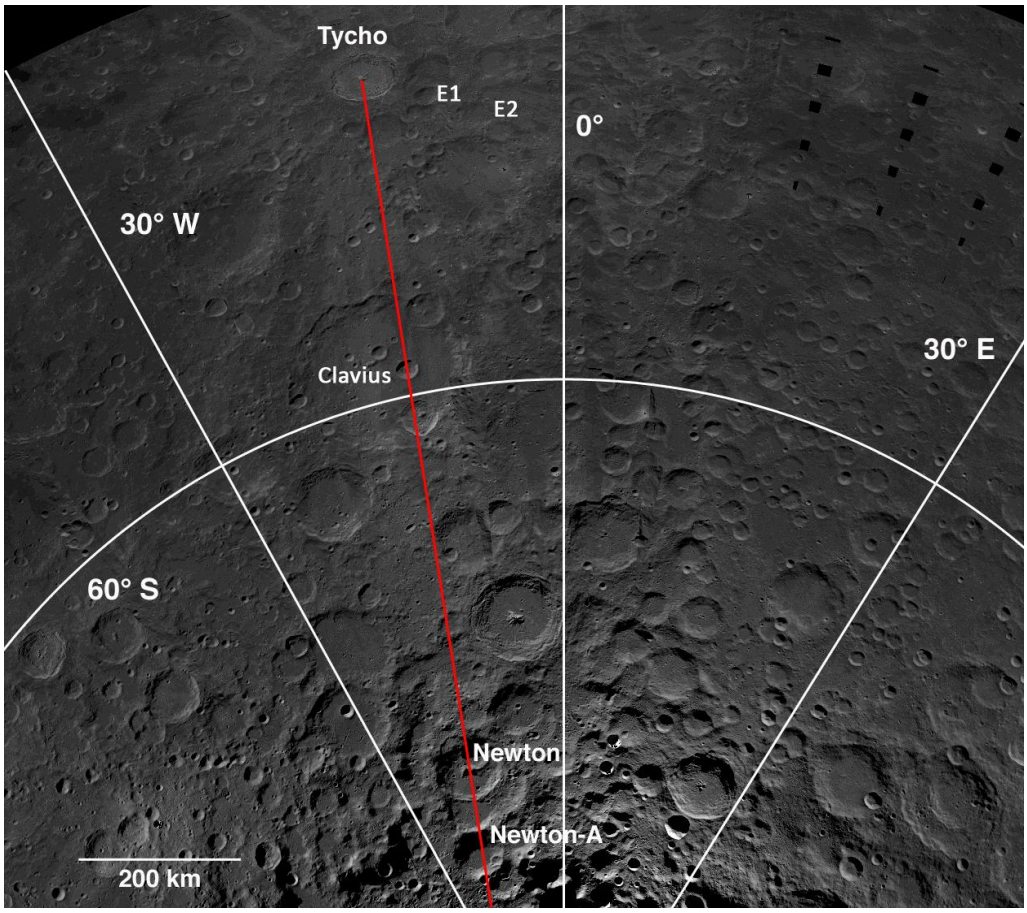

Figure 2.1. The Tycho crater ray (red line) extending south and crossing Newton and Newton-A craters as seen in a Clementine 750 nm image of the lunar South Pole. Secondary craters identified in this work were found on the floors of these craters with ejecta blankets parallel to the highlighted Tycho ray. Image courtesy of the LPI Clementine mapping project.

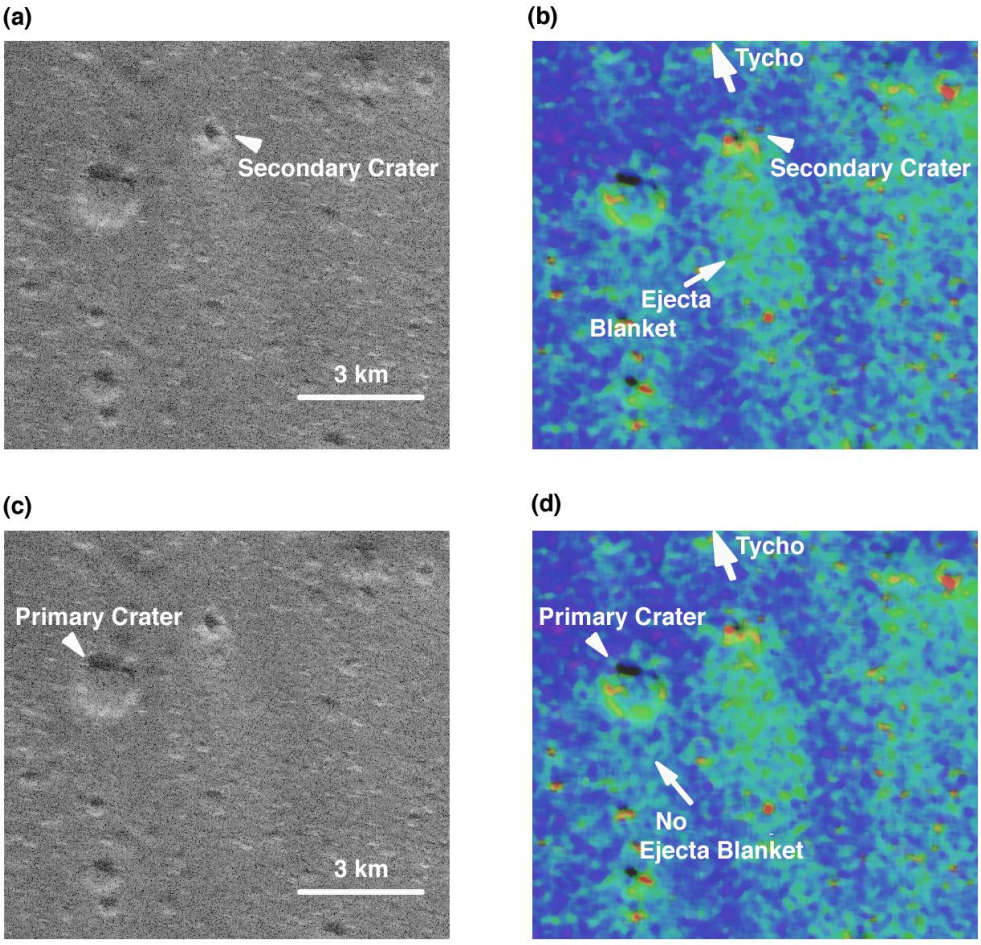

Figure 2.2. (a) A secondary crater in the SC radar channel image. (b) The same secondary crater in the CPR image. The ejecta blanket of the secondary crater, in comparison to that of the primary crater, is absent in the direction facing Tycho but elongated down-trajectory. (c) A typical primary crater in the SC radar channel image. (d) The same primary crater in the CPR image. Note that the ejecta blanket, while visible in the CPR, is highly symmetric. For additional examples, see Figures 3.1 and 3.2.

a “hidden” extension of that structure. This area may have previously been optically bright and weathered to its present condition.

2.2 Dataset

The images of the lunar South Pole used in this work were acquired on 15 September 2006 by transmitting a single sense of circularly polarized, 2.38 GHz (13 cm) radiation from Arecibo Observatory and receiving the reflected lunar echo in both senses at the Green Bank Telescope (GBT) in Green Bank, West Virginia [*Campbell et al., 2006*]. The data were processed as outlined in *Campbell et al.*, 2010. The CPR maps represent the ratio of same-sense (as transmitted; SC for “same circular”) of received polarization to opposite-sense (OC for “opposite circular”), and can be used to deduce wavelength-scale roughness properties of the reflecting surface. A specular reflecting surface gives a CPR of zero because the sense of circular polarization is reversed upon reflection, while more same-sense radiation is returned due to diffuse scattering. The classification of secondary craters discussed here hinges on this property; the secondary craters have asymmetric ejecta blankets which show up in the CPR because they are rough and blocky on spatial scales comparable to the radar wavelength. The distribution of this CPR enhancement is different at secondary craters, where it is concentrated downrange, compared to fresh primary craters, which may exhibit CPR enhancements, but they are more symmetrically distributed around the crater. There is greater contrast between ejecta blankets with enhanced CPR and the background on smooth surfaces (i.e., when the background CPR is low). As a result, this technique is best suited for investigation of secondary craters in the maria or other smooth regions. Elongated ejecta blankets are prevalent on the floors of Newton, Newton-G, and Newton-A craters near the lunar South Pole (Figure 2.2). At a distance of greater than 1000 km, the secondary craters visible in the CPR image at

Newton and Newton-A are some of the furthest secondary craters from the Tycho impact examined to date. Similar distal Tycho secondary craters were identified in Ranger 7 spacecraft images of Mare Cognitum, also at a radial distance of about 1000 km [*Wilhelms et al.*, 1978]. Dundas and McEwen (2007) also investigated the density of distal Tycho craters in rays in Mare Cognitum and near Ptolemaeus crater (~1100 km from Tycho, similar to the distance between Tycho and Newton-A) and estimated based on their counts that Tycho produced at least 10^6 secondary craters with diameters greater than 63 m. However, they stress that this is a lower-bound on secondary crater production that does not include secondary craters between or beyond rays evident in albedo or compositional maps. Work on Mars [*McEwen et al., 2005; Preblich, 2005*] and Europa [*Bierhaus et al., 2001*] suggests that these populations external to obvious rays may dominate the secondary crater production of a given event. The secondary craters identified in this work are not encompassed by the 560,000 km^2 of Tycho rays identified by Dundas and McEwen (2007), and therefore probe this important parameter space for secondary cratering for the first time on the Moon.

2.3 Method

2.3.1 Primary vs. Secondary Crater Classification

In order to assess the relative importance of the small secondary craters at Newton and Newton-A compared to the local primary crater population, both primary and secondary craters were counted in these regions. Due to the sensitivity of cratering statistics to the counting method employed, much care was taken to ensure that both crater counting and primary/secondary classification were as systematic as possible. Crater diameters were measured by fitting ellipses to crater rims. According

to convention, the minor axes of the fitted ellipses were used for the crater diameters, but the major axis size and thus crater eccentricity were also recorded. The regions in which craters with 400 m $\leq$ D $\leq$ 2 km were counted were: an area of 3644 km^2 on the floors of Newton and Newton-G craters (henceforth: Newton region) and another of 996 km^2 on the floor of Newton-A crater (henceforth: Newton-A region).

A major contribution to the uncertainty of secondary classification was the difficulty in establishing one-to-one correspondence between small craters and unresolved tertiary ejecta blankets. A particular challenge was in distinguishing which of the craters in the ejecta blankets were responsible for the ejecta and which had merely been superposed by it. To help break the degeneracy, the simultaneous age of the Tycho secondary craters was employed. Because of the shared age of Tycho and its secondary craters and the assumed homogeneity of the lunar terrain in the relatively small regions of interest, the rim morphology of all Tycho secondary craters in the study should be equally degraded. A potential pitfall of this assumption would be if downrange secondary craters were preferentially degraded due to the downrange motion of the material comprising the areas of CPR enhancement. Considering this caveat, the secondaries identified using this assumption represent a minimum estimate of the number of secondary craters in the region. Tycho Crater is an extremely young (96 +/-5 Myr [*Arvidson et al.,* 1976]) lunar crater and its secondary craters should be among the freshest-looking small impact features in the Newton and Newton-A regions. According to *Neukum et al.* (2001)'s lunar isochrons, on the order of only a few craters younger than 100 Myr with 400 m $\leq$ D $\leq$ 2 km are expected in areas the size of Newton and Newton-A

Therefore, we can distinguish between Tycho secondaries and underlying primaries in the unresolved tertiary ejecta blankets based on the crater rim morphology. A three-fold classification system for rim freshness (in the single channel image) was devised for this purpose: (S) for the craters with the sharpest rims, (SD) for craters with moderate rim degradation, and (D) for craters with diffuse, heavily degraded rims. All craters with classifications "S" and "SD" in unresolved tertiary ejecta blankets as well as all craters with resolved tertiary ejecta blankets were classified as secondary craters. Primary craters were those classified as "D" craters in regions of unresolved tertiary ejecta blankets, all craters with no obviously correlated tertiary ejecta blanket, and "S" and "SD" craters with symmetric or no ejecta blankets. We note that use of this type of morphological classification to correlate individual craters to asymmetric ejecta blankets is somewhat subjective, but the reader is reminded that secondary craters are typically identified on the basis of differences in morphology. In total, 445 craters were counted in the two regions, 94 of which were classified as secondary craters (Figure 2.3).

2.3.2 Size-frequency Distributions

The size-frequency distributions of craters were compiled according to the recommendations set forth by the *Crater Analysis Techniques Working Group* (1979). In addition to the craters already counted with 400m < D < 2 km , all craters with diameters greater than 2 km were counted in larger regions including but also extending beyond the floors of Newton and Newton-A (12442 km^2 at Newton and 12877 km^2 at Newton-A). This was done in order to reduce small number statistics for

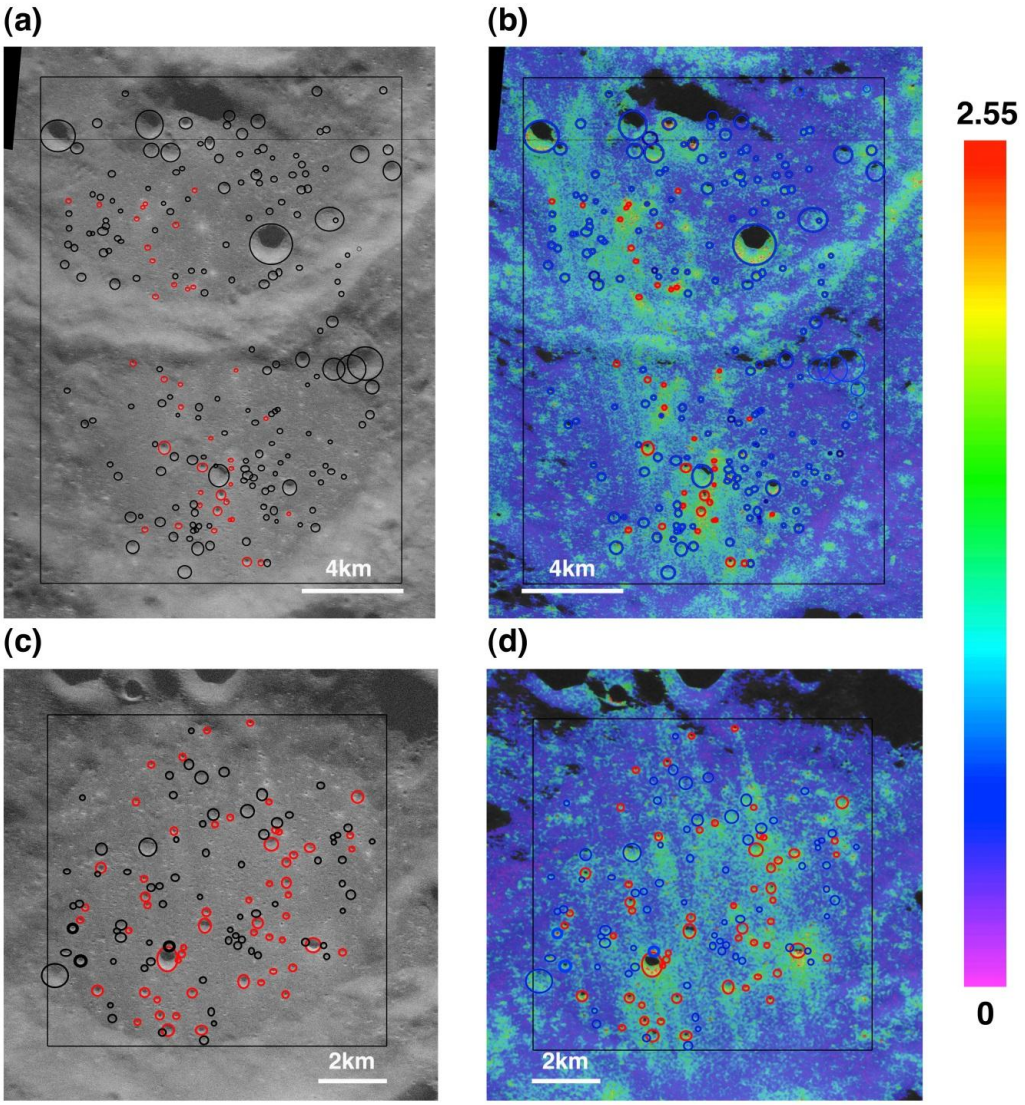

Figure 2.3. All craters counted in the Newton (a-b) and Newton-A (c-d) regions. Primary craters are marked in black/blue, with secondary craters in red. (a) 20 m/pixel single channel image of Newton and Newton-G craters. (b) The Newton region in 100 m/pixel CPR. (c) The single channel, 20 m/pixel image of the Newton-A region used for counting craters. (d) The Newton-A region in the CPR.

the larger craters. The resulting cumulative and relative size-frequency plots take the varying areas into account and are binned with √2 or √2/2 widths centered on 1 km. The first type of SFD compiled was the cumulative density plot, in which the number density of craters greater than a given diameter is plotted against the crater diameter (Figures 2.4 - 2.8). Crater SFD's are power-law functions of the form:

$$N(\geq D) = c\, D^{b}, \qquad \textbf{(2.1)}$$

where c and b are constants and D is the crater diameter. In log-log space, b is the slope of the distribution. In addition to the cumulative plots, differential or "R-plots" were also generated for the data (Figure 2.7).

The error bars for our crater counts represent the Poisson statistical counting noise associated with the total number of counts in each diameter bin. In order to assess the completeness of our counts in more than just the statistical sense, we compare the total number of secondary craters identified by *Hirata and Nakamura* (2006) in two regions to the east of Tycho, designated "E1" and "E2", to counts obtained with our method in those same areas. The results of this comparison are displayed in Table 2.1. In these regions, it appears that the radar method is less sensitive to counts of small craters than the optical method. The reason for this is probably two-fold. Firstly, the radar return is sensitive to the surface roughness, and region E1 in particular has a very high background roughness because of its proximity to Tycho crater's continuous ejecta blanket. Therefore, it is more difficult to make out small crater rims against the background. Secondly, the radar incidence angle is

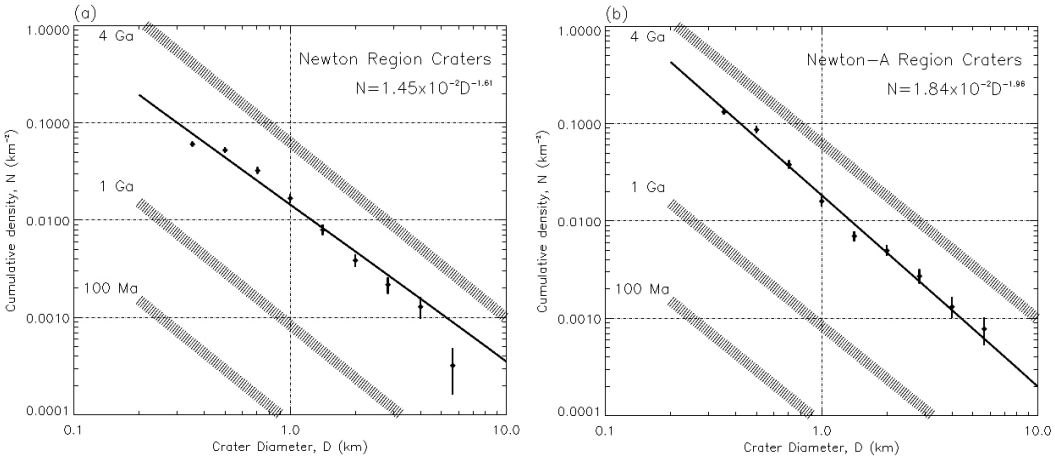

Figure 2.4. The cumulative size-frequency distribution of all craters counted in (a) the Newton region and (b) the Newton-A region. The isochrons in this and all other figures follow Neukum et al. (2001).

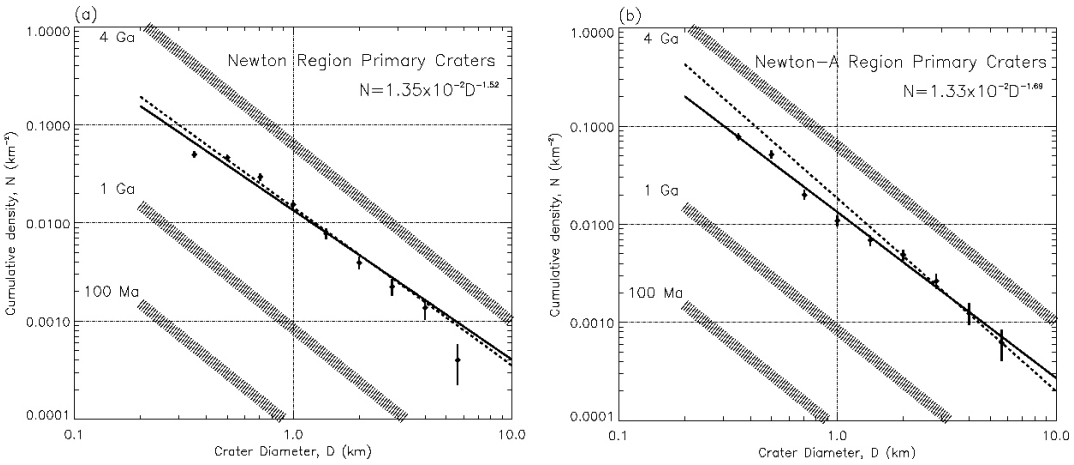

Figure 2.5. The cumulative size-frequency distribution of the corrected primary craters (after removal of secondary craters) in (a) the Newton region and (b) the Newton-A region. The dotted line represents the fit to the crater distribution calculated before the removal of the secondary craters.

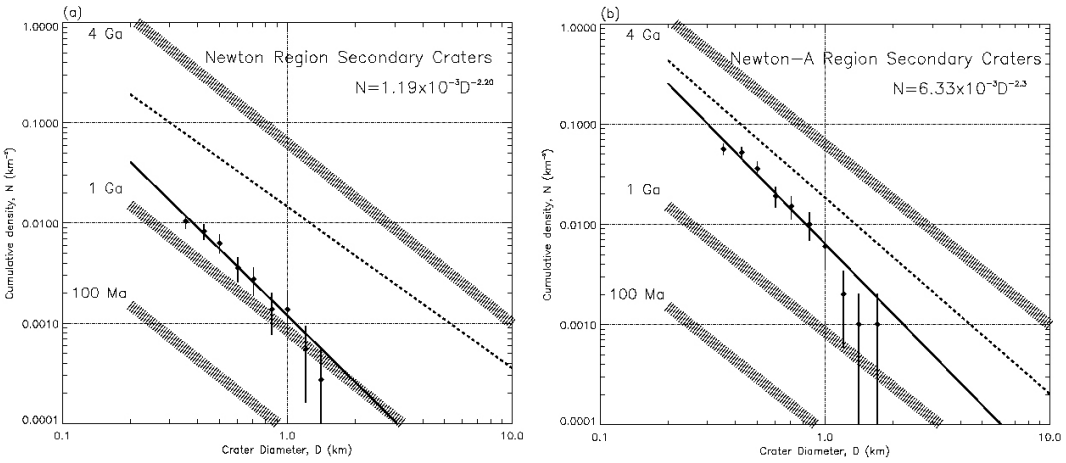

Figure 2.6. Cumulative size-frequency distributions of the secondary craters identified at the (a) Newton region and (b) Newton-A region. The dotted line represents the combined distribution of primary and secondary craters first counted in the areas.

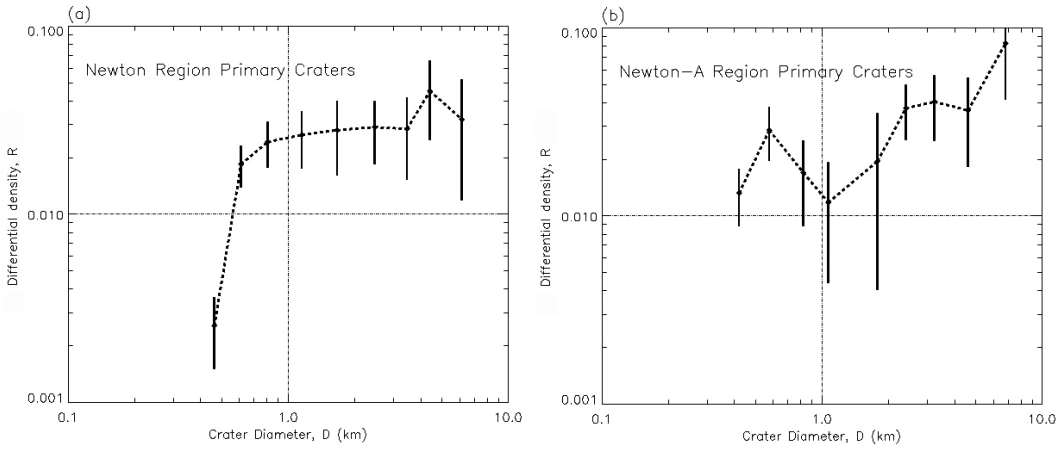

Figure 2.7. A differential plot (R-plot) of the corrected primary crater populations at the (a) Newton region and (b) Newton-A region. Note the dearth of craters counted in the 1 km and 1.717 km bins at Newton-A.

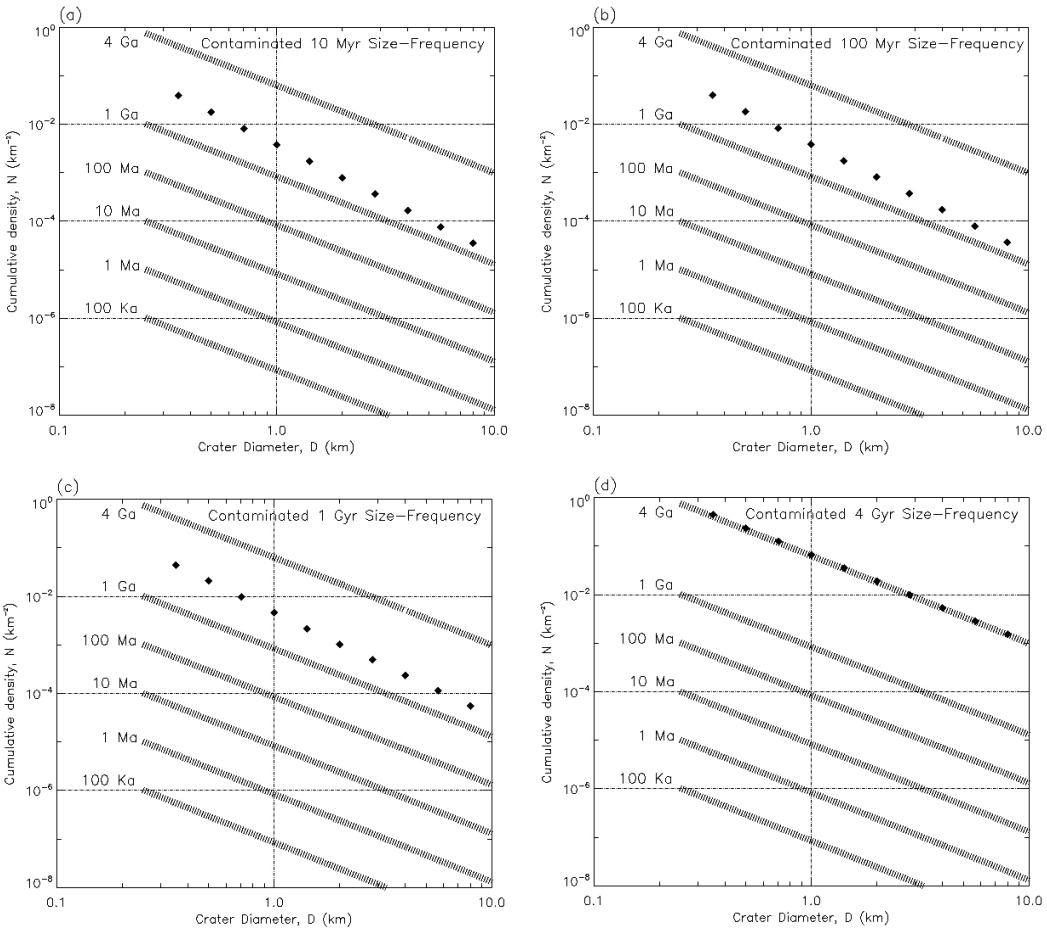

Figure 2.8. A secondary crater population similar to those measured here, with $N(\geq D)=3.8x10^{-3}xD^{-2.25}$, emplaced on hypothetical lunar terrains with cumulative size frequency distributions as given in Neukum et al. (2001). Specifically, secondary contamination of (a) 10 Myr-old lunar terrain, (b) 100 Myr-old lunar terrain, (c) 1 Gyr old lunar terrain, and (d) 4 Gyr-old terrain. The shaded lines correspond to the ideal cases; diamonds represent populations contaminated by secondary craters.

Table 2.1. A comparison between the number of secondary craters identified near Tycho crater by Hirata and Nakamura (2006) and the radar CPR method employed here. The cut-off diameter is relevant only to the power-law fits of Hirata and Nakamura (2006) (i.e., not to the total counts). The necessity of a cut-off for fitting illustrates that secondary crater populations tend to "turn down" from their characteristic steep power-law slopes in this size range.

†Hirata & Nakamura (2006)
‡CPR and Tertiary Ejecta Blanket Method
*Number of craters used for best-fit calculation

	Number of Secondary Craters †	Number of Secondary Craters‡	Cut-off Diameter for Power-law Fit †	Power-law Fit †
E1	92 (35)*	98	1.7 km	$N(\geq D)=(1.32\pm0.11)x10^{-1}D^{-3.44\pm0.11}$
E2	145 (52)*	55	1.0 km	$N(\geq D)=(1.26\pm0.07)x10^{-2}D^{-3.82\pm0.15}$

relatively low at the latitude of Tycho crater, reducing radar shadow that also aids in the recognition of small craters. These two factors are less important on the relatively smooth floors Newton and Newton-A craters, where the radar incidence angle is also very high (near grazing) due to the near-polar latitude. In any case, there is no obvious reason why secondary craters should be more affected than primary craters.

2.4 Results

2.4.1 Secondary Crater Populations and Comparisons to Other Work

Lunar primary craters exhibit a $b=-1.8$ slope in a cumulative size-frequency distribution, as compared to the steeper, $b=-3$ or -4 slope seen at crater diameters less than a few km. The interpretation that this steep branch is composed of secondary impacts was suggested by *Shoemaker* (1965), and has been more recently discussed in the work of *Hirata and Nakamura* (2006) and *Dundas and McEwen* (2007).

In their analysis, *Hirata and Nakamura* (2006) found 92, 145, 134, and 98 secondary craters in regions at distances of 130, 190, 250, and 370 km from the Tycho primary, respectively. The cumulative SFDs of these four regions displayed characteristic power law slopes ranging between $b=-3.32$ and $b=-3.82$. The secondary craters surveyed by *Hirata and Nakamura* (2006) range in size from 0.55 km < D < 4.0 km, as compared to the Newton and Newton-A regions, where the largest secondary craters observed had diameters just under 2 km. The secondary crater densities measured by *Hirata and Nakamura* (2006) suggest that crater density does not decrease at a constant rate with distance from the primary, but rather levels off

after a few crater radii. The secondary craters at Newton and Newton-A fit this trend. The secondary density at Newton-A (1108 km from Tycho), $c=6.33x10^{-3}$ craters/km^2, and at Newton (1015 km from Tycho), $c=1.19x10^{-3}$ craters/km^2, are only slightly lower than the $6.81x10^{-3}$ craters/km^2 measured by Hirata and Nakamura (2006) at 370 km from Tycho.

The shallow power-law slopes of *b=-2.20* at Newton and *b=-2.30* at Newton-A are seemingly unusual for secondary crater populations, which are often characterized by their steep power-law forms. However, there is a well-documented, prominent down-turn (i.e. a shallow power-law slope) in the cumulative SFD of secondary craters that commonly occurs near diameters of about a kilometer, seemingly independent of distance from the primary crater [*Hirata and Nakamura* (2006); *Arvidson et al.,* 1976; *Wilhelms et al.,* 1978]. The shallow power-law slopes at Newton and Newton-A support this claim [*Arvidson et al.,* 1976; *Wilhelms et al.,* 1978]. When larger secondary craters are available, small craters in the regime of the downturn are not typically included for power-law fitting. *Hirata and Nakamura* (2006) derived steep power-law slopes for secondary craters above this downturn; for smaller craters, the slopes are similar to those seen in the small diameter population sampled at Newton and Newton-A. *Hirata and Nakamura* (2006) attribute the down-turn to the destruction of small craters by the surges of ejecta generated by the many simultaneous impacts involved in the formation of a field of secondary craters. *Dundas and McEwen* (2007) also see shallow slopes within Tycho rays near Ptolemaeus crater but do not explicitly state the power-law slopes for these distributions. They suggest that, generically, such down-turns in the secondary crater

SFD in rayed areas could be attributed to a number of factors, ranging from surges during emplacement that obliterate underlying or smaller craters, differential erasure of craters after emplacement due to surrounding slopes, observational incompleteness near the edge of resolution, and possibly the "true rollover" diameter at which ejecta production from primary craters deviates from the typical steep power-law. However, this diameter is not well constrained, and higher-resolution images are needed to distinguish between these factors at Newton and Newton-A. We will address this issue in the next chapter with LROC NAC photographs.

2.4.2 Primary Crater Populations

The cumulative SFDs for the corrected (i.e., after the removal of the secondary craters) crater populations with 400 m ≤ D ≤ 8 km are shown in Figure 2.5. Much like the downturn at small diameters in the secondary crater population, we expect that the primary cumulative SFD will level off due to saturation equilibrium. While the Newton region primary craters exhibit a plateau in the cumulative distribution at D ≤ 500 m, the Newton-A primary craters do not. Instead, there is a slight apparent excess of primary craters at these diameters. To clarify the issue, consider the differential R-plot size-frequency distribution (Figure 2.7).

Because each bin stands alone, the differential SFD not only illuminates intrinsic differences in the crater population over various diameters, but also reveals the unequal distribution of counting error throughout the sample. The R-plot shows that the kink present in the cumulative plot may be attributed to the effects of small number statistics on the mid-range bins with 1.717 km ≤ D < 2 km. This bin shows an

anomalously low density with respect to the other size ranges, a property that translates to a temporary leveling off of the cumulative SFD in this region. The expected number of small primaries (for a $b=-1.8$ SFD) produces an artificially steepened branch in comparison to this momentary "plateau" in the cumulative distribution. The relative dearth of primary craters recorded in this bin is thus simply an artifact of the limited area available for study in the Newton and Newton-A crater floors. This case-study illustrates an important point about the difficulties in interpreting cratering statistics for units of small spatial extent.

2.5 Discussion

2.5.1 Crater Count Contamination

An important part of the controversy surrounding secondary impact craters is the effect of secondary cratering on the inferred ages of young surfaces. Terrains in obvious ray systems are not age-dated using crater counts because of the obvious contamination by secondary craters. However, our measurements suggest that the floors of Newton and Newton-A may belong to a “hidden” extension of a known Tycho ray. This ray is “hidden” because there is no associated albedo enhancement in optical photographs. It is possible that there was once an albedo enhancement associated with this hidden ray, but that space weathering has darkened this region more rapidly than at regions closer to Tycho crater, possibly due to a difference in ray thickness with distance from the parent crater. For a full discussion of space weathering with respect to lunar rays, see *Hawke et al.* (2004). Because this portion of the ray is only apparent in the radar CPR, it could be mistaken as “ray-free” terrain

and included in crater counts by workers relying only on optical images. Therefore, we compare the incorrect age that would be determined from such a count with the more accurate age determined after the removal of the secondary craters associated with the "hidden" ray.

Including the secondary craters, the best-fit power law inferred for Newton-A was $N(\geq D)=(1.84\pm0.07)x10^{-2}D^{(-1.96\pm0.05)}$ and $N(\geq D)=(1.45\pm0.06)x10^{-2}D^{(-1.61\pm0.05)}$ for Newton. Using *Neukum et al.* (2001)'s lunar isochrons, these distributions correspond to ages of 3.80 and 3.76 ±0.01 Ga, respectively. After removal of the identified Tycho secondary craters, the density constant measured for Newton-A region was $c=(1.33\pm0.06)x10^{-2}$ and $c=(1.35\pm0.05)x10^{-2}$ for Newton. These coefficients correspond to ages similar to those of the uncorrected population, at about 3.75 Ga for Newton and Newton-A (Figure 2.5). The age inferred from the corrected primary counts suggests that resurfacing by impact melt from nearby Orientale basin (~3.8 Ga) may be responsible for the relatively smooth Newton and Newton-A craters floors [*Wilhelms et al.,* 1979; *Campbell and Campbell,* 2006].

It is possible that other such "hidden rays" exist on the lunar surface. Assuming that Newton and Newton-A are representative samples, "hidden" secondary crater populations have the potential to significantly skew the interpretation of crater counts on very young surfaces, such as the ejecta blankets of recent craters. Figure 2.8 shows the extent to which similar, undetected secondary populations could contaminate hypothetical lunar terrains of various ages. These plots were created by adding a density representative of the secondary crater populations at Newton and Newton-A ($c=3.76x10^{-3}$) to the densities predicted by *Neukum et al.* (2001) for 10

Myr, 100 Myr, 1 Gyr and 4 Gyr lunar terrains. For purposes of discussion, we assume that the secondary densities measured at Newton and Newton-A are typical of hidden ray populations, and that current lunar isochrons are based on primary-dominated counts at small diameters (in other words, that the secondary populations measured here occur in isolated regions). We also ignore the probable erasure of some underlying primary craters that would occur during emplacement of the hypothetical secondary layer. With these assumptions, the result of failing to remove hidden ray secondary craters from counts in regions where they exist can be summarized as follows:

(1) Surfaces with true ages older than about 3.4 Ga will be largely unaffected by the addition of the hidden ray population. The erroneous increase in age will be on the order of a few percent, as at Newton and Newton-A. For small terrain units where the D< 1km population is important for age dating, this is on the order of, or less than, the uncertainty in age introduced by counting statistics.

(2) Surfaces with true ages around 3.4 Ga superposed by hidden ray secondary craters will contain roughly equal numbers of 1 km diameter primary and secondary craters. For small terrain units where the D< 1km population is important for age dating, the increase in age by improperly including the secondary craters is slightly less than 20%, from 3.4 to around 4 Ga.

(3) Surfaces with ages less than 3.4 Ga will be dominated by secondary craters at diameters below 1 km if "hidden ray" craters are present. The result of improper inclusion of hidden ray secondary craters in counts for age-dating on a surface with a true age of 1 Ga, for example, would be to make the surface appear 3.48 Ga old, about

2.5 times older. Again, this is primarily relevant for small terrain units where the D<1km population is important for age-dating. Young crater ejecta blankets and some volcanic features on the Moon fall within these age and size bounds. Because of the potential to significantly alter the inferred ages of such features, it will be vital to quantify how common such hidden rays are on the lunar surface.

2.5.2 Post-Tycho Primary Crater Impacts

Identification of secondary craters by the presence of asymmetric ejecta blankets also provides a convenient benchmark around which the local superposition relationships can be investigated. The Tycho secondaries in question have a well constrained age of ~96 Ma derived from Tycho ray material gathered by Apollo astronauts [*Arvidson et al.,* 1976]. Using the known age of the secondary layer, three "snapshots" in time of the Newton and Newton-A floors were produced: one prior to the Tycho event, one of the regions just after Tycho was emplaced around 96 Ma, and one of the present crater floor with the layers labeled in time (Figure 2.9). Primary craters were determined to be older than the Tycho secondaries based on three criteria: lack of a high-CPR ejecta blanket; obvious rim erosion and floor flattening relative to the fresher secondary layer; or superposition of a high-CPR ejecta tail. Conversely, primaries younger than the inferred Tycho secondary features were identified based on sharp rim morphology coincident with symmetric high-CPR ejecta blankets. The rim erosion of the primary craters (and subsequent infill leading to shallow floors) older than the secondary crater layer may be the result of "sand blasting" of the region by secondary and tertiary ejecta, which is why it is indicative of craters that were already

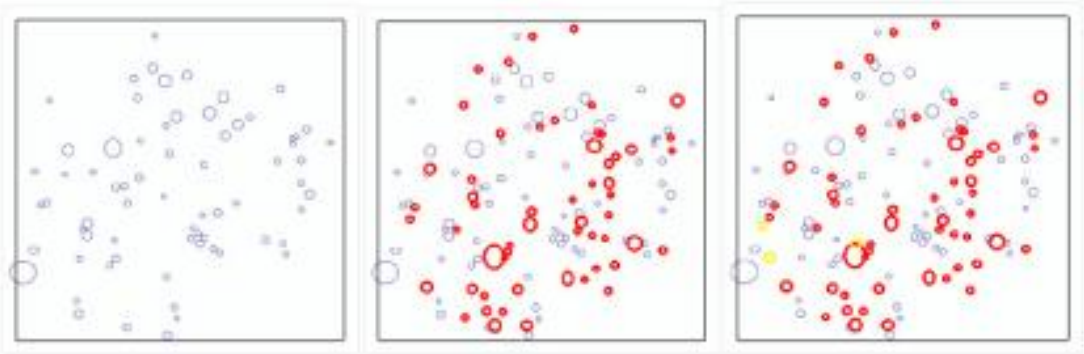

Figure 2.9. The superposition relationships determined for the Newton-A region using the common age of the Tycho secondary craters. (a) The region before the Tycho event, about 100 Ma. (b) The region just following the emplacement of the Tycho secondaries, shown in red atop the pre-existing craters in blue. (b) The region today, with the primaries formed since the Tycho event in yellow.

on the surface when the secondary layer was emplaced. Given a larger survey, this method could provide a strong constraint on the production function of small lunar primaries during the last 100 Myr.

2.6 Summary

CPR maps of Newton and Newton-A craters reveal a cluster of small (D < 2 km) craters with highly asymmetric ejecta blankets, aligned roughly parallel to one another and along the same direction as an optical Tycho ray several hundred kilometers to the northwest. I interpret these CPR-bright ejecta blankets as tertiary ejecta belonging to small Tycho secondary craters. Best-fit power-laws slopes (b=*-2.20±0.27* and b=*-2.30±0.22)* for the secondary populations at Newton and Newton-A are shallower than the canonical b=*-3or-4* for secondary craters. However, secondary crater size-frequency distributions display a down-turn at small diameters that is not typically included in the calculation of the power-law slope. The secondary SFDs at Newton and Newton-A represent this smaller diameter population, and are in agreement with the behavior measured at small diameters by other workers [*Hirata and Nakamura, 2006; Dundas and McEwen, 2007*]. The high number density secondary craters measured ($c \sim 10^{-3}$ craters/km^2) and the orientation of their ejecta along the Tycho radial direction suggest that this population is a "hidden" extension of the visible Tycho ray that superposes Clavius crater. As other lunar rays may continue as secondary crater over-densities beyond where they are visible as high albedo features, the degree of possible contamination by similar populations on lunar terrains over a range of ages was explored. The extent of contamination was quantified by

adding the average secondary crater density at Newton and Newton-A (as a function of crater diameter) to the densities predicted by *Neukum et al*. (2001) for 10 Myr, 100 Myr, 1 Gyr, and 4 Gyr lunar terrains. The resulting ages of the combined populations were compared to the "uncontaminated" ages represented by the *Neukum et al*. (2001) isochrons. In the presence of a "hidden ray", primary and secondary craters can be expected to occur in roughly equal numbers on lunar terrains with primary crater densities corresponding to 3.4 Ga. For hidden rays superposing surfaces with primary crater densities corresponding to ages younger than 3.4 Gyr, secondary craters would dominate all counts below 1 km. Because of the potential to significantly alter the inferred ages of young features, future work should investigate where and how commonly such hidden rays occur on the lunar surface.

CHAPTER 3

THE ORIGIN OF RADAR CPR ENHANCEMENTS AT LUNAR SECONDARY CRATERS

3.1 Introduction

As we have discussed at length, crater counting is used to age-date surfaces of terrestrial bodies throughout the Solar System. Calibrated by lunar sample return, the cratering record on the Moon anchors crater size-frequency distributions to absolute ages [*Neukum et al.,* 2001]. Therefore, it is important that the crater populations of the lunar isochrons reflect a true production function and are not significantly contaminated by secondary craters. A central component of this controversy is the inherent difficulty in distinguishing small primary and secondary craters. Traditionally, secondary craters are classified based on their unusual morphologies, including elliptical planforms, shallow floors, clustering, and braided terrains (*Morrison and Oberbeck*, 1975; *Lucchitta*, 1976). However, it is uncertain whether or not all secondary craters possess these characteristics, or if a significant component of the secondary population is morphologically more similar to primary craters (*Dundas and McEwen*, 2007; *Bierhaus et al.*, 2001; *Wells et al.*, 2010). In the last chapter, we saw how radar polarization data can help alleviate this problem by providing an alternative view of secondary crater clusters.

On the Moon, radar CPR enhancement is observed at both secondary craters and fresh primary craters. However, the geometry of the elevated CPR regions is very different for primary craters than for secondary craters (Figure 3.1). In the case of

Figure 3.1. Differences in the distribution of elevated radar CPR values at primary and secondary craters, as seen in 13-cm radar CPR maps overlaid on LROC WAC mosaics. (a) A fresh primary crater in the Magnius Basin southeast of Tycho crater. The elevated CPR values are distributed symmetrically around the crater and only extend a distance of one or two crater radii (LROC WAC M119882141ME). (b) Tycho secondary crater clusters and a lone secondary with elevated CPR values (LROC WAC M119956789ME). Unlike at the primary crater in (a), the CPR enhancements associated with these secondary craters are distributed asymmetrically around the craters, concentrated mostly in the downrange direction. Note that the CPR enhancements extend several crater radii from the secondary craters. (c) Craters Messier-A and Messier-B in Mare Tranquilitatis. *Herrick and Forsberg-Taylor* (2003) interpret this as a primary double-impact. Note the "butterfly" morphology of the CPR enhancement at Messier-A, with the elevated CPR concentrated perpendicular to the impact direction. The CPR enhancement associated with Messier-B is concentrated downrange from the crater. However, it is different from the downrange signature seen at secondary craters, in that it displays ray-like filaments of enhanced CPR downrange instead of a general downrange wedge-shape. The CPR enhancement at Messier-B is also confined to within about a crater diameter from the crater itself, whereas the regions of elevated CPR at secondary craters are more extensive.

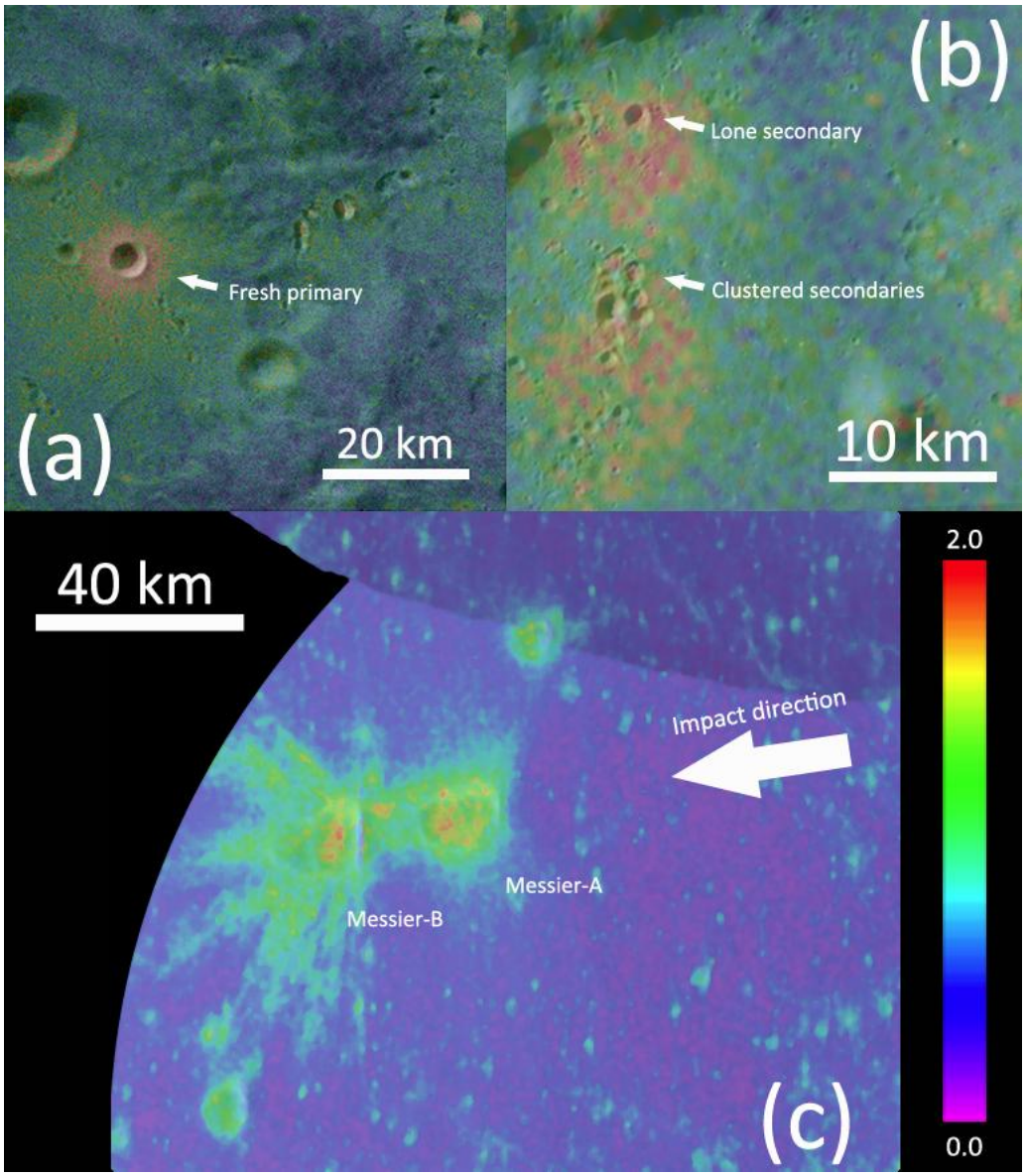
(a)
Fresh primary
20 km
(b)
Lone secondary
Clustered secondaries
10 km
40 km
Impact direction
Messier-A
Messier-B
(c)
2.0
0.0

fresh primary craters, the regions of elevated CPR are symmetric about the crater, except in cases of oblique impacts ($\theta < 30°$) [*Herrick and Forsberg-Taylor*, 2003]. At impacts below 30°, asymmetries in the regions of CPR enhancement begin to appear. These asymmetries are reminiscent of the changes that occur in the ejecta blanket at these impact angles, such as zones of avoidance and butterfly patterns [*Herrick and Forsberg-Taylor*, 2003]. As we saw in the last chapter, however, radar CPR enhancements associated with secondary craters, on the other hand, are not symmetric [*Wells et al.*, 2010]. They are concentrated downrange, forming "streaks" pointing away from the parent crater. They do not exhibit the uprange notches or "butterfly" morphologies observed for oblique primary impacts [*Herrick and Forsberg-Taylor*, 2003]. Additionally, radar CPR enhancements at secondary craters typically extend many crater radii downrange from the crater [*Wells et al.*, 2010]. This is another distinction from the elevated radar CPR regions observed at primary craters. Even for oblique impact angles, CPR enhancements associated with the continuous ejecta blankets of fresh primary craters extend at most a few crater radii from the crater (Figure 3.2). CPR enhancements due to fresh primary crater rays extend large distances from the crater, but are morphologically distinct from the secondary crater signatures as well. Even at low impact angles, rays of enhanced CPR extending from primary craters are filamentary in nature, unlike the wedge-shaped CPR enhancements observed at secondary craters [*Wells et al.*, 2010]. In this chapter, we address the origin of these features and the conditions in which we can expect secondary craters to be accompanied by radar CPR enhancements.

Figure 3.2. (a) Areas of elevated radar CPR extend radially from Tycho crater, mapping out secondary craters and clusters. Outside of the continuous ejecta blanket, these instances of CPR enhancement occur in discrete, wedge-shaped regions, forming "streaks" downrange from secondary craters. (b) In the LROC WAC photograph (M119916068ME) on the left, black arrows point to two clusters of Tycho secondary craters with traditional morphologies. White arrows point to circular craters without traditional secondary morphologies. Elevated CPR values in the 13-cm radar overlay on the right reveal that the white arrow craters are also Tycho secondaries. Using only photographs, these craters might be misidentified as primary craters.

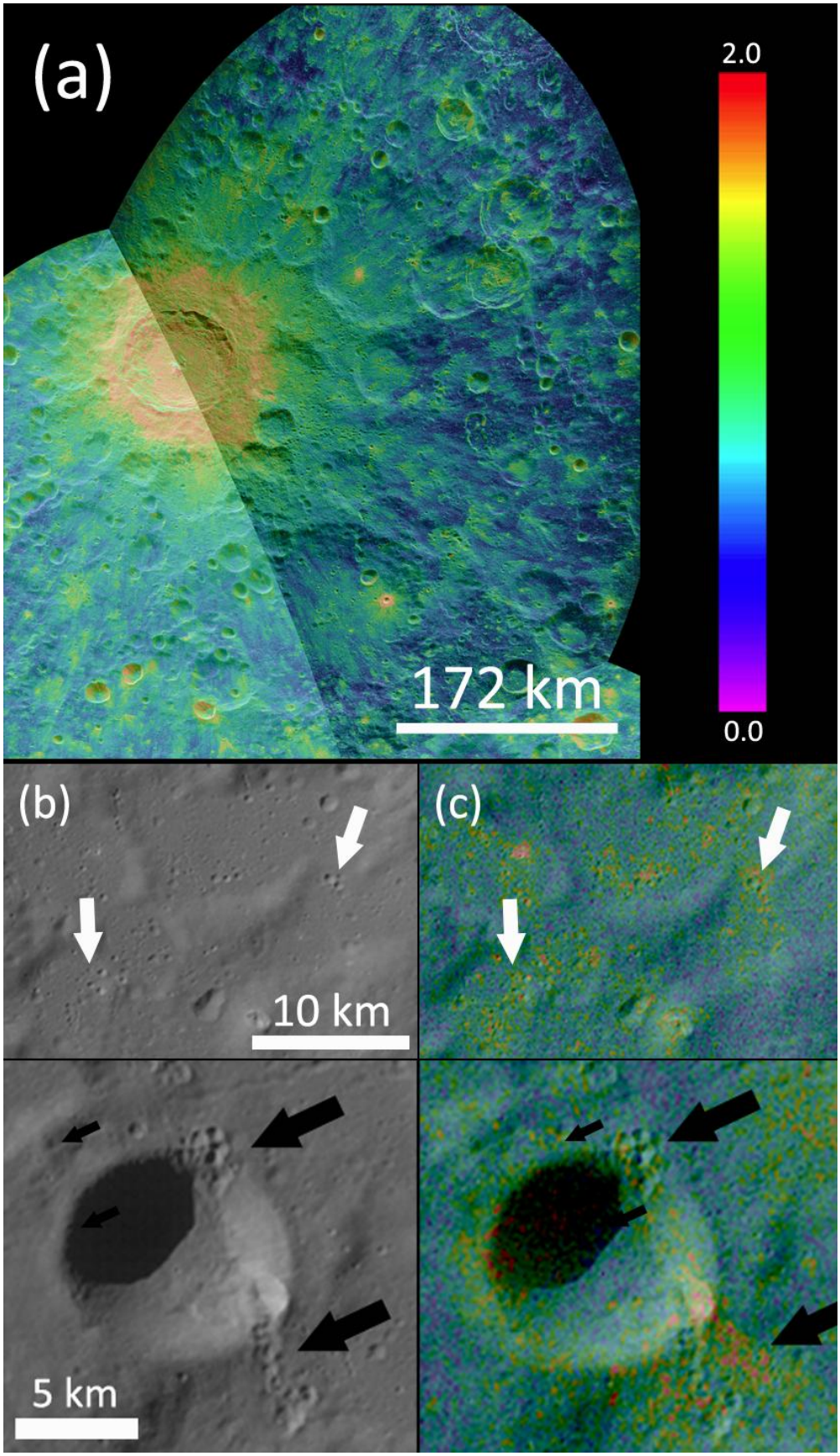
(a)
2.0
0.0
172 km
(b)
10 km
(c)
5 km

3.2 Data and Methods

This study of CPR enhancements at lunar secondary craters utilized a combination of ground-based radar and Lunar Reconnaissance Orbiter Camera (LROC) photographs. In the last chapter, we looked at radar CPR enhancements at 13-cm. In this chapter, we extend our study to include 70-cm radar CPR as well. Radar CPR is sensitive to scattering on the radar wavelength, so by investigating both the 13- and 70-cm polarization behavior, we probe two different populations of scatterers. The penetration depth of the radar signal into the regolith is also wavelength dependent, with longer wavelengths penetrating further, on the order of a few radar wavelengths [*Campbell*, 2002]. Therefore, our multi-wavelength study also samples different regolith depths [*Campbell*, 2002].

The radar data used in this work were collected bi-statically with the 305 m Arecibo Telescope transmitting at either 13- or 70-cm and the 100 m Green Bank telescope receiving the echo. The 13-cm data were collected between 2005 and 2010 and the 70-cm data were obtained through the NASA PDS. The effective resolution of the radar maps is 160m/pixel for the 13-cm data and 400m/pixel for the 70-cm data. LROC Wide Angle Camera (WAC) and Narrow Angle Camera (NAC) products were also obtained through the NASA PDS. The locations of the LROC NAC products used in this work are shown in Figure 3.3. The locations and resolutions of the LROC WAC products used can be found in Table 3.1.

The 13-cm CPR maps have been overlain on LROC WAC products in order to put the high-resolution (~0.5m/pixel) NAC images into context [*Robinson et al.*,

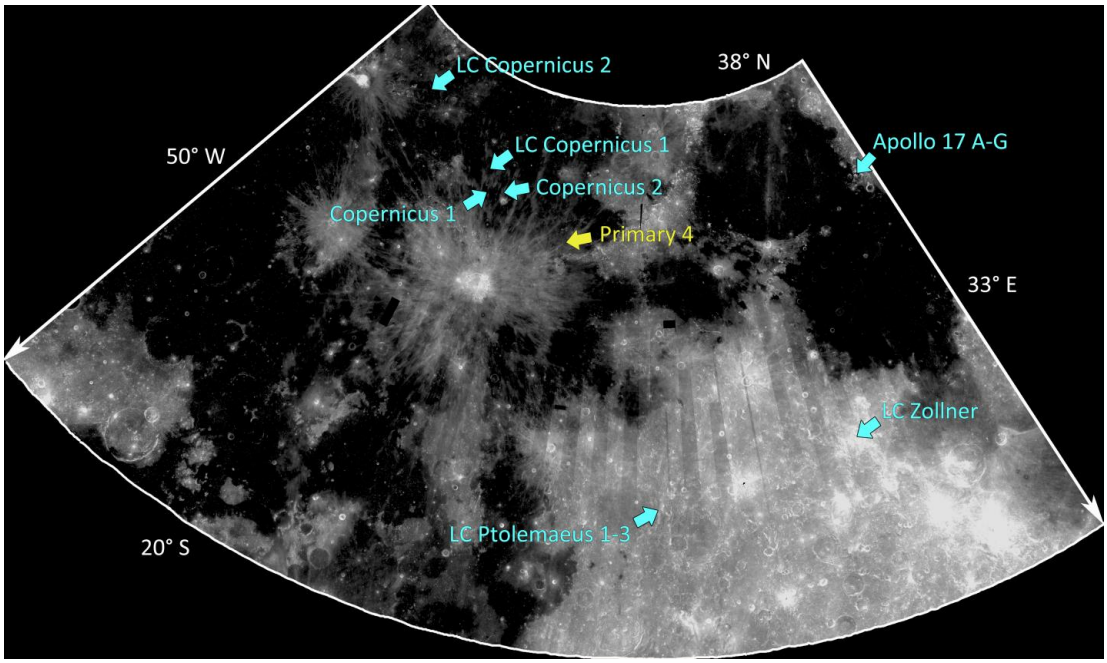

Figure 3.3. (a) The locations of NAC groups listed in Table 3.1. Clementine UVVIS 750-nm basemap.

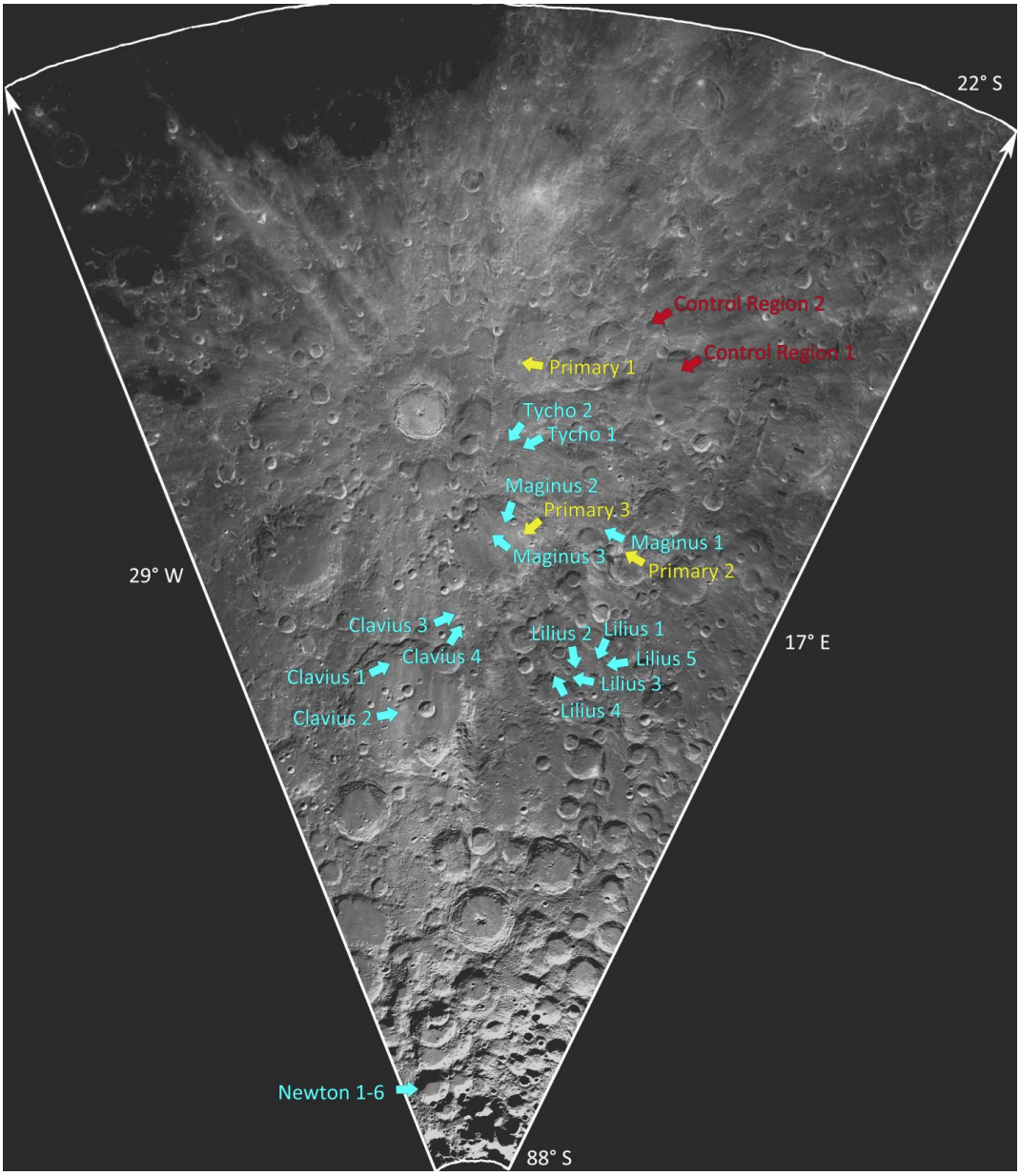

Figure 3.3. (b) The locations of NAC groups listed in Table 3.1. Clementine UVVIS 750-nm basemap.

Table 3.1. WAC product data

Product ID	Region	Resolution (m/pixel)	Center Latitude	Center Longitude
M109039047	Apollo 17	69.41	23.42	30.8
M119888744	Clavius	69.39	-63.49	355.13
M119895706	Clavius	66.21	-54.2	353.92
M119895899	Clavius	63.91	-43.96	353.75
M119915875	Clavius	69.98	-64.45	351.23
M119916068	Clavius	66.59	-54.19	350.95
M119922863	Clavius	69.50	-53.77	349.35
M119936429	Clavius	69.19	-54.21	348.36
M119983943	Clavius	73.96	-53.79	340.88
M116377890	Copernicus	66.86	13.33	350.25
M116445567	Copernicus	65.68	22.91	339.9
M116459128	Copernicus	65.36	23.43	337.84
M116472720	Copernicus	65.02	22.26	335.76
M119800691	Lilius	67.84	-53.75	8.23
M119807487	Lilius	67.65	-53.25	7.17
M119814256	Lilius	67.64	-54.23	6.15
M119834425	Lilius	69.73	-64.5	3.31
M119841222	Lilius	69.76	-64	2.25
M119854788	Lilius	69.99	-64.49	0.2
M119861585	Lilius	69.87	-63.98	359.16
M119868381	Lilius	69.70	-63.51	358.13
M119848211	Maginus	67.52	-53.27	0.94
M119868574	Maginus	67.33	-53.26	357.89
M119875536	Maginus	64.13	-43.98	356.74
M119909298	Maginus	66.26	-53.28	351.92
M119990739	Maginus	75.23	-53.24	339.84
M119936622	Tycho	70.57	-43.94	348.56
M116345123	Tycho	69.35	-48.59	354.88

2005]. This allows us to compare morphologies on the NAC and WAC scales and local variations in the radar CPR values. These overlays were created by registering the CPR maps to the WAC products, which are typically on the order of 70 m/pixel resolution. Because of the difference in resolution and projection between the two data sets, the true CPR resolution is not preserved in these overlays.

3.3 Observations

As mentioned previously, workers during the Apollo-era established photogeologic criteria for morphologies associated with secondary cratering. *Morrison and Oberbeck* (1975) studied morphologies within the continuous ejecta blankets of lunar craters and discussed their pertinence to secondary cratering. They were particularly interested in the movement of local material due to secondary crater formation. They coined the terms "concentric dunes" and "radial ridges" to explain regions of elevated topography associated with chains or clusters of secondary craters. Concentric dunes were defined as ridges at high angles to the radial line and were observed uprange from clusters of secondary crater chains (Figure 3.4). The orientation of these dunes was consistent with ridges observed in laboratory simulations of simultaneous impacts occurring along the same impact direction [*Morrison and Oberbeck*, 1975]. In the lab, these dunes formed due to the interference of the craters' ejecta blankets. In their lunar observations, *Morrison and Oberbeck* (1975) noted that such dunes could be well-developed even in places where the secondary craters themselves were subdued. They hypothesized that in these

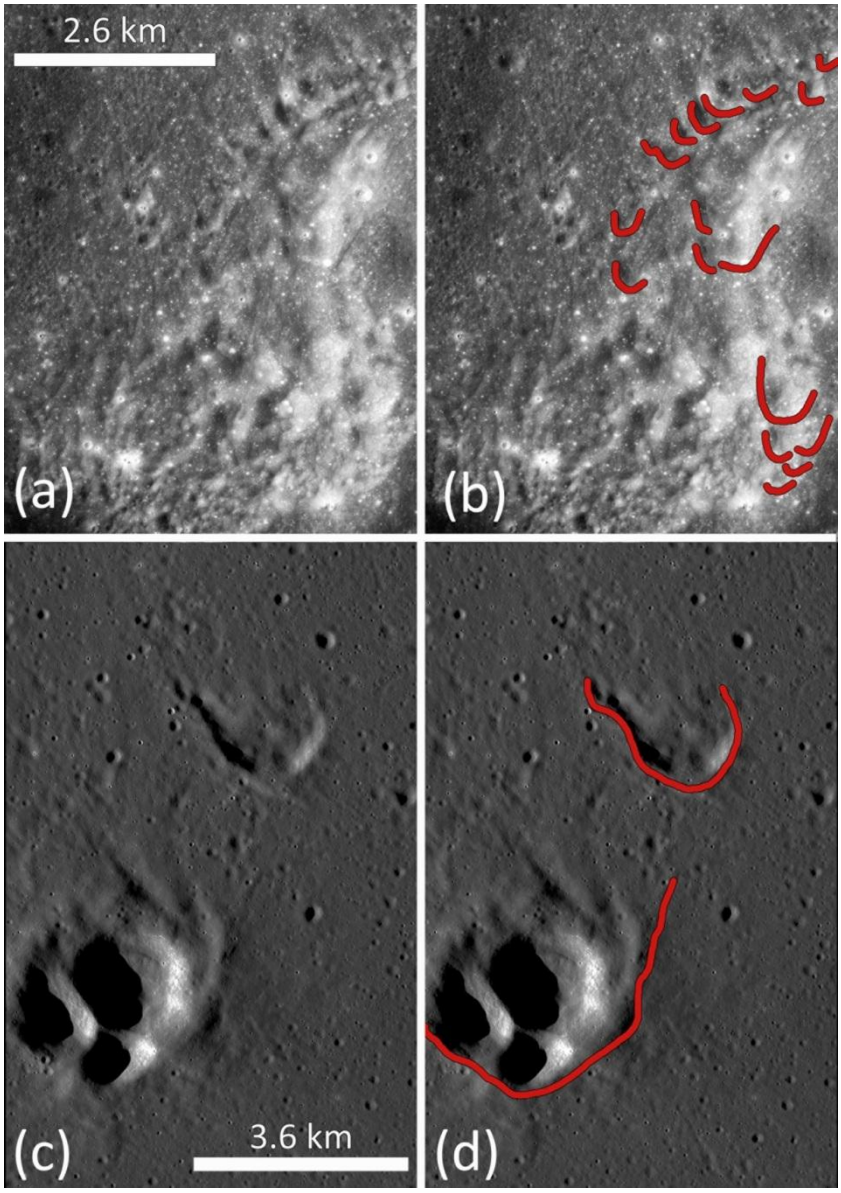

Figure 3.4. Examples of concentric dunes. (a & b) Concentric dunes observed at region LC Ptolemaeus 1 (LROC NAC M106870568LC). (c & d) Concentric dunes observed at region Copernicus 1 (LROC NAC M102307509LC). The red markings in parts (b) and (d) highlight the position of the dunes. *Morrison and Oberbeck* (1975) interpreted concentric dunes as deposits due to interfering ejecta from secondary craters forming simultaneously at different distances along the same impact direction.

cases, the secondary craters responsible for the dunes had been obliterated by debris surge. Debris surge, they argued, was similar to base surges observed at terrestrial explosion craters. In a base surge, a volatile-injected debris cloud moves radially away from the explosive event at high velocity. Unlike base surge, debris surge does not require an atmosphere. Instead, *Morrison and Oberbeck* (1975) proposed that primary ejecta fragments at the base of the expanding ejecta curtain interacted with the local surface to generate a high-velocity, ground-hugging flow of primarily local debris following close behind the true ejecta curtain. *Morrison and Oberbeck* (1975) argued that this process would preferentially remove depressed surface expressions, like secondary craters, while raised "deceleration dunes" would form uprange of pre-existing elevated features, like crater rims. We stress that in the context of this work, “uprange” is synonymous with the direction radially back toward the parent crater, while “downrange” refers to the direction radially away from the parent crater.

Radial ridges were defined as raised ridges at small angles to the radial direction. Like concentric dunes, *Morrison and Oberbeck* (1975) argued that radial ridges were the result of secondary ejecta interference. Concentric dunes were formed by secondary craters at different distances along the same impact direction and radial ridges by craters at the same radial distance. *Lucchitta* (1976) also reported v-shaped dunes and braided terrains in her investigations of lunar secondary crater clusters. These terms appear to correspond to *Oberbeck and Morrison* (1975)*’s* concentric dunes and radial ridges, respectively. Lucchitta also reported “sharp, sinuous depressions” at the intersection of densely clustered craters, as well as collections of v-shaped ridges and grooves and braided lineations in the disturbed areas (*Lucchitta*,

1976). For the sake of continuity, I have tried to employ these existing descriptors when appropriate.

3.3.1 Control Regions

The goal of this investigation of the LROC WAC and NAC products was to correlate morphologies unique to secondary craters with radar CPR enhancements. To serve as a comparison, I began by characterizing control regions with background CPR levels (Table 3.2). Two regions northwest of Tycho crater were selected that exhibited background levels of radar CPR at 13-and 70-cm. These products are located on the western interior walls of Stölfer (D=126 km) and Fernelius-A (D=30 km) craters, respectively (Figure 3.5). Both of these regions appear to have been largely—though not completely—"shadowed" from Tycho secondary cratering by the Tycho-facing rims of these large craters. The selected control regions cover areas which exhibit background levels of CPR. However, due to the exact locations of the NAC cover, isolated secondary chains with associated CPR enhancements are also present in these regions. I characterize both terrain types in the following sections.

3.3.1.1 Control Region 1

This region is located in Stölfer crater, near the central part of its northern rim. It is situated a few kilometers to the west of a group of Tycho secondary crater clusters with prominent CPR enhancements (Figure 3.5). The secondary craters in these chains are oriented radially to Tycho crater. Like many clustered secondary craters,

Table 3.2. NAC product data for Background CPR Regions

Product ID	Group	Resolution (m/pixel)	Center Latitude	Center Longitude
M109196546L	Background 1	0.52	-39.76	5.73
M109196546R	Background 1	0.52	-39.76	5.63
M142246134L	Background 2	0.51	-38.26	3.25
M142246134R	Background 2	0.51	-38.27	3.15

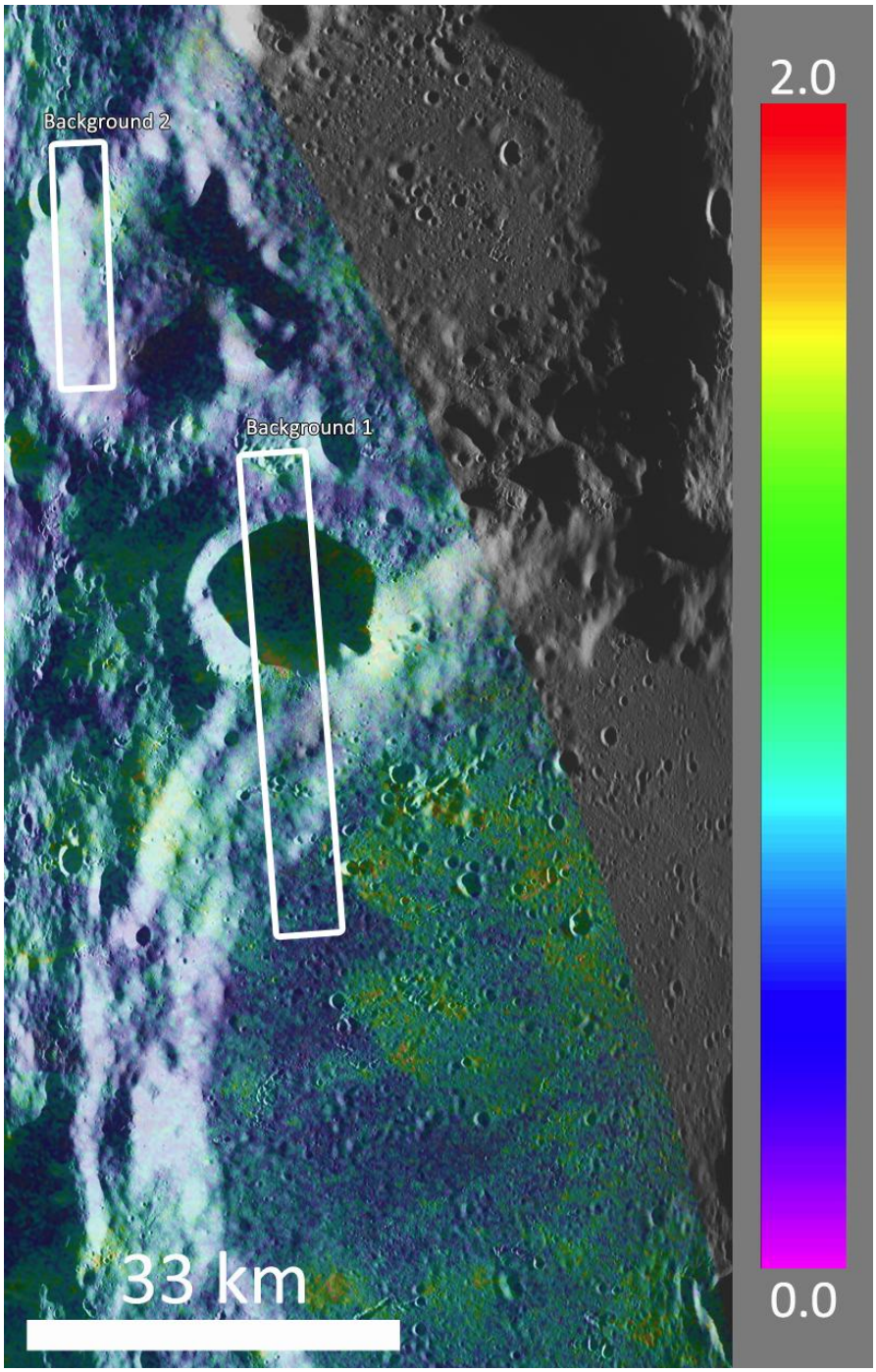

Figure 3.5. Radar CPR context of Control Regions 1 and 2; 13-cm radar CPR overlaid on a LROC WAC photograph (LROC M116283858MC).

they exhibit elliptical planforms with uprange dunes pointing back toward Tycho. The CPR-WAC overlay reveals that the regions of CPR enhancement associated with these isolated secondary crater chains have very sharp spatial boundaries. At these boundaries, the CPR values transition rapidly from background levels to values exceeding one. The locations of the boundaries appear to correspond with the presence of v-shaped dunes extending from the uprange-most craters in the secondary clusters (Figure 3.5).

One of the small, isolated Tycho secondary crater chains is located near the center of this region, on a terraced portion of the wall of Stölfer crater (Figure 3.5). These craters are 0.5 to 1 km in diameter and are accompanied by a slight CPR enhancement at 13-cm. These morphologies do not reflect the surface properties of regions with background levels of CPR, but for the sake of completeness, we will briefly describe the morphologies in these small areas of CPR enhancement.

The rims of the secondary craters in the regions of enhanced CPR are sharp at the WAC scale, but at NAC resolution, the rim morphology appears very subdued. The secondary craters themselves are characterized by rounded uprange rims and open or very heavily degraded downrange rims. Some of the secondary craters also exhibit concentric dunes like those described by *Morrison and Oberbeck* (1975). Lineations are also observed surrounding these secondary craters. These lineations begin uprange from the crater clusters and extend downrange at a lower angle to the radial line than the angle of the concentric dunes (Figure 3.6). The lineations appear to be low,

mounded ridges a few meters wide and ranging in length from a few tens of meters to upwards of a hundred meters. They trend generally from southwest to northeast, creating an overall subtly textured appearance or elongation of features in that direction. As we will see later, linear features are common in regions of CPR enhancement associated with secondary craters, but this is one of the few examples in our observations of a surface with a regional-scale texture without a strong 13-cm CPR enhancement. One possible explanation for the lack of a CPR enhancement in this instance is that the smooth material on which the lineations form is deeper here than observed elsewhere.

Apart from the lineations, the terrain surrounding this isolated secondary cluster appears very smooth on the tens-of-meters scale, as if material on the surface has been swept along the direction of the lineations. This is in sharp contrast to the terrain south of the secondary cluster, which exhibits a "hummocky" appearance on the tens-of-meters scale. The areas of these linear features correspond to background levels of CPR, while the hummocky regions correspond to CPR enhancements. The downrange areas inside the angle of the concentric dunes are also areas of CPR enhancement.

Away from these isolated secondary crater chains, Control Region 1 exhibits background levels of CPR at 13-and 70-cm. These background levels occur on the interior wall and westernmost part of the floor of Stölfer crater. At the NAC scale, these areas of background levels of CPR are characterized by small primary craters with shallow depth-to-diameter ratios and very subdued rims. This morphology dominates craters in these regions with diameters between ~0.1-0.5 km. Below this

size, the craters are deeper for their size and exhibit sharper rims.

3.3.1.2 Control Region 2

Like Control Region 1, these products were chosen because they represent an area with background levels of radar CPR. This region lies in an area of low radar CPR at 13-and 70-cm on the inside western rim of Fernelius-A crater, just north of Stölfer (Figure 3.5). As with Control Region 1, the area covered by these products also includes several isolated secondary crater chains belonging to Tycho crater. Here, as before, the uprange rims of these secondary craters, which appear sharp at WAC resolution, appear quite rounded at NAC resolution.

As we saw in the areas of background CPR in Control Region 1, the regions of background CPR covered in Control Region 2 lack lineations and other regional patterns on the surface. Instead, these surfaces are dominated by small primary craters. Unlike the small secondary craters, with their subdued rims and filled floors, these small primary craters would have sharp rim morphologies and bowl-shaped profiles. Several of these small primary craters also have albedo-bright ejecta blankets, indicative of young ages.

3.3.2 Fresh Primary Craters

In addition to investigating surface morphologies in regions of background level CPR values, we also observed the surface morphologies of a few kilometer-sized

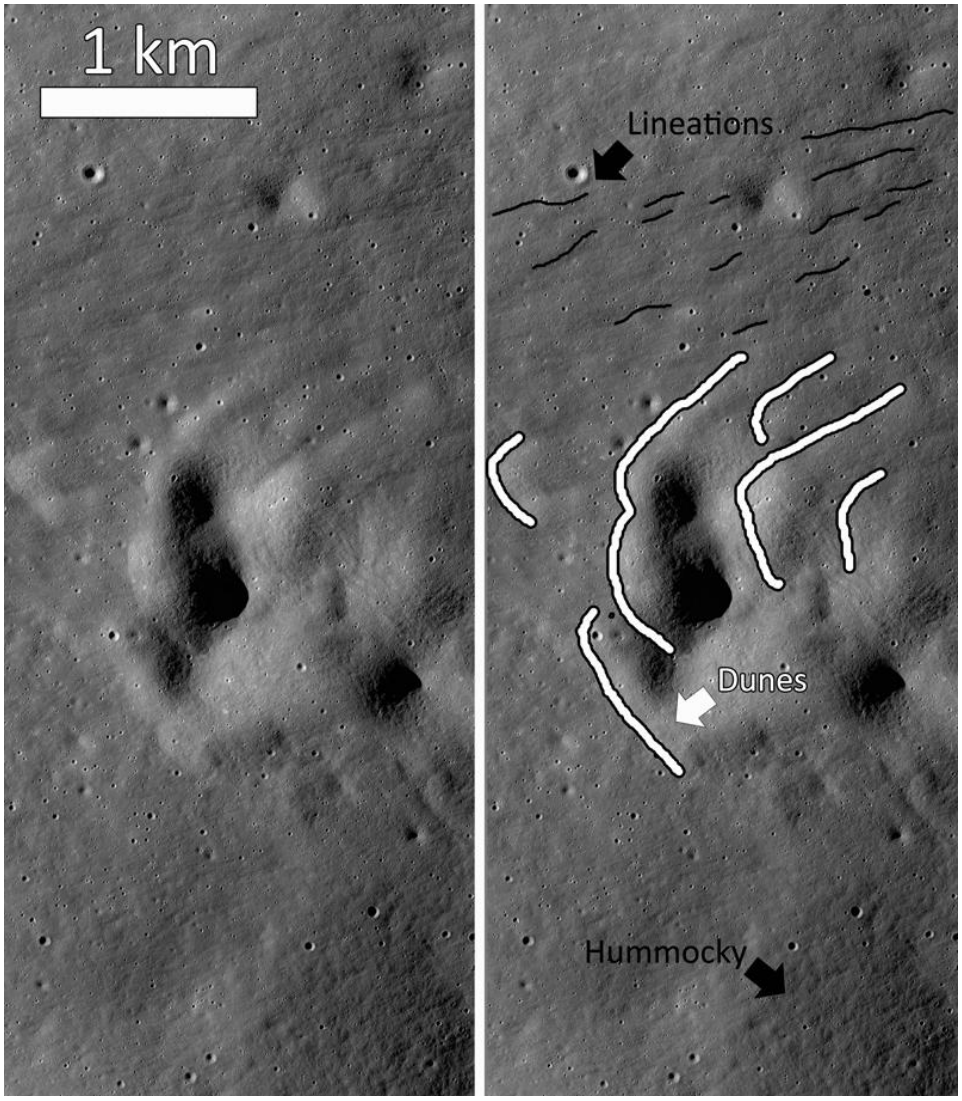

Figure 3.6. Concentric dunes and lineations at a cluster of small Tycho secondary craters in Background Region 1 (LROC NAC M165823235LC). The lineations have a lower angle to the radial direction than the dunes. The areas downrange from the dunes the hummocky region have higher CPR values at 13-cm than the lineated terrain.

primary craters to compare to the morphologies observed at secondary craters. Fresh primary impact craters were cataloged in four separate regions: one on the continuous ejecta blanket of Tycho crater at Pictet-E, two near Maginus crater, and two northeast of Copernicus crater in the Imbrium basin (Figure 3.2, Table 3.3). We determined that these were primary impacts because they were not members of crater clusters, they did not exhibit any traditional secondary morphologies on the WAC scale, nor were they accompanied by asymmetric, wedge-shaped CPR enhancements [e.g., *Lucchitta*, 1976; *McEwen et al.*, 2005; *Wells et al.*, 2010; *Robbins and Hynek*, 2011].

I chose a combination of highlands and mare craters in order to address potential effects of target properties on the resulting crater morphologies. The freshness of these impact features was determined based on their stratigraphic relationship with Tycho and Copernicus crater rays. Each of these small primary craters also exhibits an azimuthally symmetric radar CPR enhancement at 13-and 70-cm, indicative of a young age.

3.3.2.1 Primary Region 1

Primary Region 1 covers a fresh, bright 1.4 km diameter primary crater on the floor of Orontius crater, just northeast of Tycho (Figure 3.7). This small crater superposes the continuous ejecta blanket of Tycho crater and therefore post-dates the Tycho impact. The small primary crater has a radar CPR enhancement at 13-and 70-cm, but the enhancement extends further from the crater at 13-cm. As stated earlier, the areas of enhanced radar CPR are not in the characteristic wedge shape reported for secondary craters, but rather symmetric around the crater planform, as we would

Table 3.3. NAC product data for Primary Crater Regions

Product ID	Group	Resolution (m/pixel)	Center Latitude	Center Longitude
M129322429L	Primary 1	0.50	-40.82	355.27
M129322429R	Primary 1	0.50	-40.82	355.18
M142239567L	Primary 2	0.51	-49.82	4.27
M142239567R	Primary 2	0.51	-49.82	4.15
M129315484L	Primary 3	0.51	-49.35	356.36
M129315484R	Primary 3	0.51	-49.35	356.24
M144694133L	Primary 4	0.51	17.6	349.18
M144694133R	Primary 4	0.51	17.6	349.1

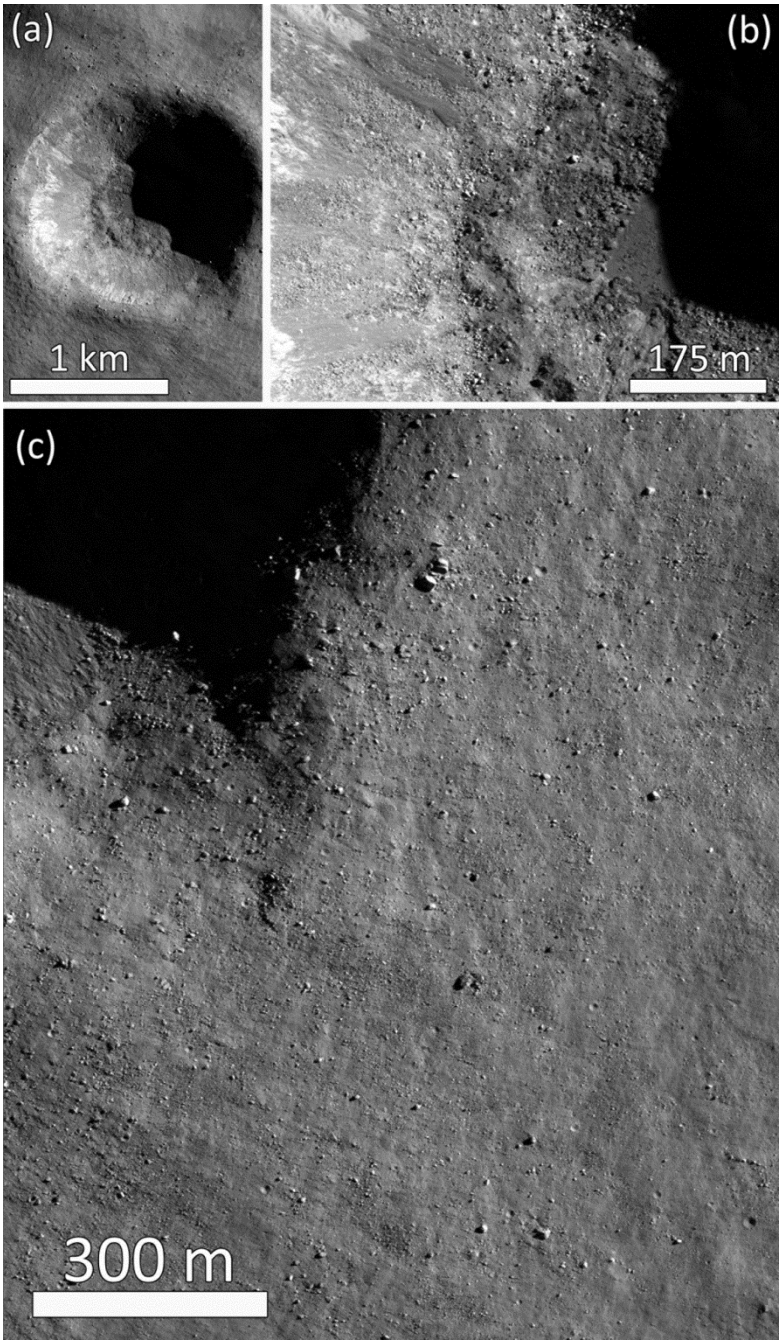

Figure 3.7. Rim and floor morphologies at the 1.5 km diameter primary crater in Primary Region 1 (LROC NAC M129322429LC). (a) This small primary crater has a sharp planform and mound of dark, blocky material on its floor. Dark and light striations on the interior walls indicate mass wasting. (b) A pond of smooth, dark material on the crater floor. It is possible that these deposits consist of impact melt. (c) The spatial distribution of blocky material outside of the crater rim. These blocks range in size from <0.5 m to upwards of 10 m in diameter.

expect for the continuous ejecta blanket of a fresh primary crater with moderate impact angle [*Herrick and Forsberg-Taylor*, 2003; *Wells et al.*, 2010].

At NAC resolution, this crater has a sharp rim with evidence of mass wasting events moving material down the interior walls to the crater floor (Figure 3.7). Dark and light striations on the interior crater walls indicate movement of material down the slope. Clast size sorting appears to have taken place in these striations, with larger blocks concentrated toward the crater floor and smaller clasts suspended partway up the wall. The crater floor itself is covered in a mound of blocky material with a small deposit of smooth, dark material at the center. This smooth material is potentially impact melt. The dark, particulate deposits on the interior wall may represent a splash of this impact melt which has eroded from the crater rim back down toward the floor. Outside of the crater rim, blocky material is distributed evenly around the crater. The sizes of these blocky clasts vary from the edge of resolution (~0.5 m/pixel) to diameters of approximately ten meters.

3.3.2.2 Primary Region 2

This region is located in the heavily cratered terrain to the east of the Maginus basin (Figure 3.8). It covers a fresh, 3.7 km diameter primary crater with radar CPR enhancements at 13-and 70-cm. The 13-cm enhancement extends further from the crater than the 70-cm enhancement. This crater sits on the intersection of the rims of several large, ancient craters.

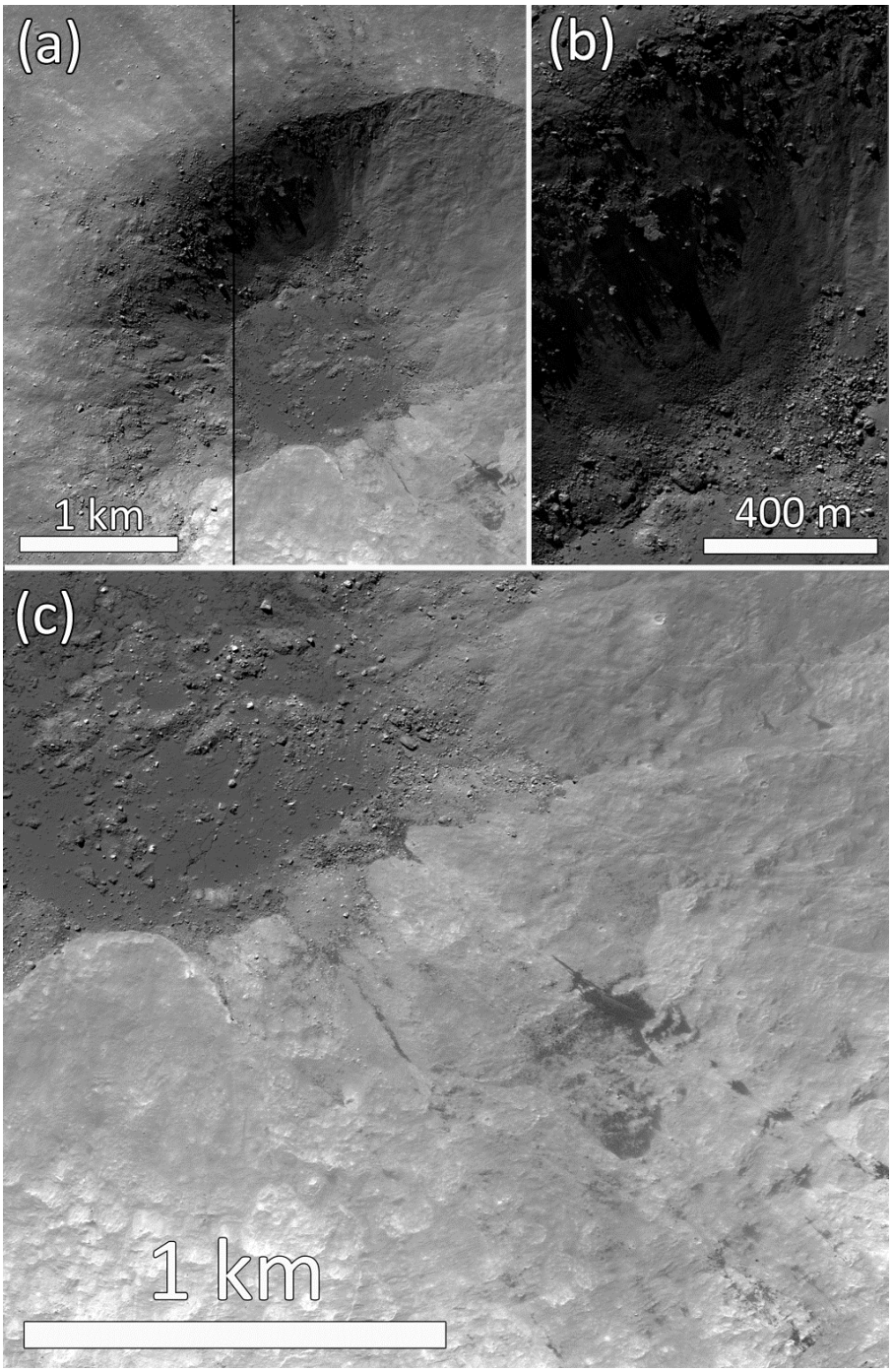

Figure 3.8. A 3.6 km diameter primary crater located east of the Maginus basin (Primary Region 2; LROC NAC M142239567LC and M142239567RC). (a) Impact melt forms a pond of dark material in the northwest corner of the crater floor. This melt appears to have splashed over the northwestern rim quadrant. (b) The dark melt flowed back down over the rim, creating blocky flows with lobate margins. (c) Localized splashes of melt are also observed on the southeastern interior wall. This splashed melt appears to have lithified into a blocky material

At the NAC scale, blocky material extends in radial "rays" away from the crater, starting very near the crater rim. These rays of blocky material are concentrated to the northeast of the crater. The western, northern, and southern rims have very sharp boundaries, with evidence of movement of material downslope on the interior southwestern rim.

Dark impact melt forms a pool slightly offset to the northeast of the center of the crater floor (Figure 3.8). Melt also appears to have splashed up the northeastern interior wall, where it drapes over the rim. There are cracks in the dark melt material on the crater floor, presumably due to contraction during cooling (Figure 3.8). In addition to the smooth material on the crater floor, the dark splashed material on the northeastern interior wall appears to be composed of blocky clasts.

The interior of the northeastern wall of this crater is relatively steep compared to the western and southern interior walls. The impact melt pond and splash are also offset to this side of the crater (Figure 3.8). This asymmetry could be the result of a moderately oblique impact, or it may simply reflect unique target asymmetries due to the confluence of the ancient crater rims in this region.

The impact melt that splashed over the rim to the northeast also shows evidence of flow back into the crater. The result of this flow is a series of arcuate lobes of dark material concentrated toward the base of the slope (Figure 3.8). On the surface, this dark material is strongly sorted by clast size, with smaller clasts remaining further up the slope than larger clasts. The presence of this blocky material is concentrated on the lobate margins of these dark flows. As we will see later, this type of morphology—dark, raised lobes of material with block-rich margins—are also

observed at many secondary craters, albeit in a different context.

3.3.2.3 Primary Region 3

These products cover a fresh, 4.5 km diameter primary crater located in the northeastern part of the Maginus basin (Figure 3.9). This crater displays a radar CPR enhancement at both 13-and 70-cm. At both wavelengths, the CPR enhancement is symmetric about the crater. The CPR enhancement is greater at 13-cm than 70-cm, and the 13-cm enhancement extends further from the crater than the 70-cm enhancement. This crater is surrounded by blocky material, both inside and outside of the crater rim. Many of the blocks occur in "rays" extending radially outward from near the crater rim.

An interesting difference in rim morphology between this crater and the secondary craters we observed of a similar size, such as those in the isolated crater chains at Control Regions 1 and 2. Whereas the rims of many of the secondary craters are either heavily degraded, breached, or covered by smooth material that originates outside of the crater, all movement of material toward the floor of this crater appears to have originated within the crater rim. The result is a very sharp rim boundary and patches of light and dark material on the interior wall, indicative of small, repetitive mass wasting events. Finally, this crater superposes Tycho secondary features in the region and therefore is younger than the Tycho secondary craters. The fact that mass wasting is occurring on the interior of this crater wall but apparently not at the secondary craters since their formation indicates that either the slopes on the secondary walls are too shallow to encourage mass wasting or the smooth units which

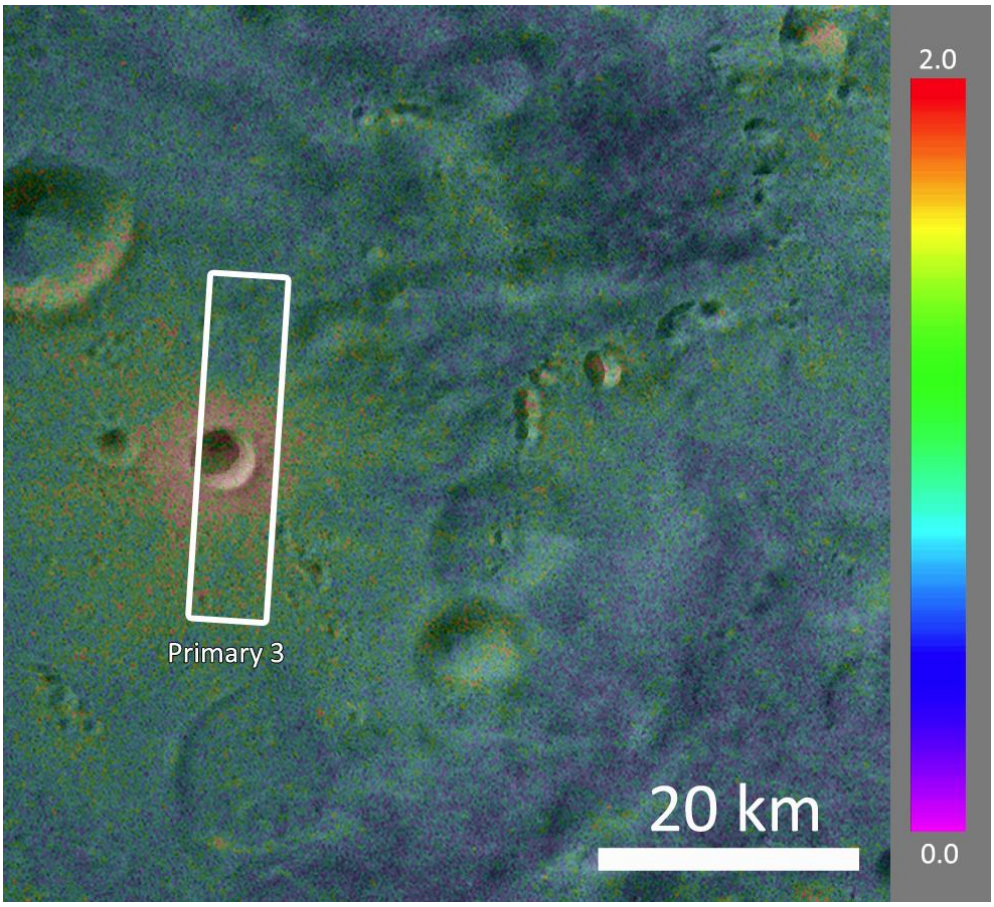

Figure 3.9. Context of the 5-km diameter primary crater in region Primary 3; 13-cm radar CPR overlaid on LROC WAC (M119868574MC). This primary crater has a CPR enhancement at 13-and 70-cm. These enhancements are azimuthally symmetric around the crater.

breach the secondary craters are more resistant to erosion than the wall materials at this primary crater.

3.3.2.4 Primary Region 4

These products cover what appear to be two well-preserved primary craters ("South Crater" and "North Crater") in the southern part of the Imbrium basin (Figure 3.10). The size of South Crater is 3.4 km and the size of North Crater is 3.5 km. These craters have CPR enhancements at 13-cm, distributed azimuthally symmetrically around their rims. By comparing the morphologies we see at these mare craters with the highlands craters in Primary Regions 1-3, we can determine if any of these features are target-dependent.

These primary craters in Primary Region 4 have sharp rims at the NAC scale. Block-rich material is common on the interior slopes of these craters and there is evidence of repeated small mass wasting events. The block rich material is distributed evenly around the interior walls of the craters and appears to correspond with the greatest CPR enhancement associated with these craters. Both of these craters have flat floors that appear to be filled with impact melt. The impact melt drapes over block-rich material, and clasts extrude from the dark, smooth melt (Figure 3.10).

Compared to the albedo of the other crater materials, the impact melt at the south crater is not as dark as the impact melt observed at the highlands primary craters. Rather, the melt pond is primarily recognizable by its very smooth appearance. This smooth material is overlain by bright, block-rich material that has moved down the interior slopes of the crater walls (Figure 3.10). This impact melt

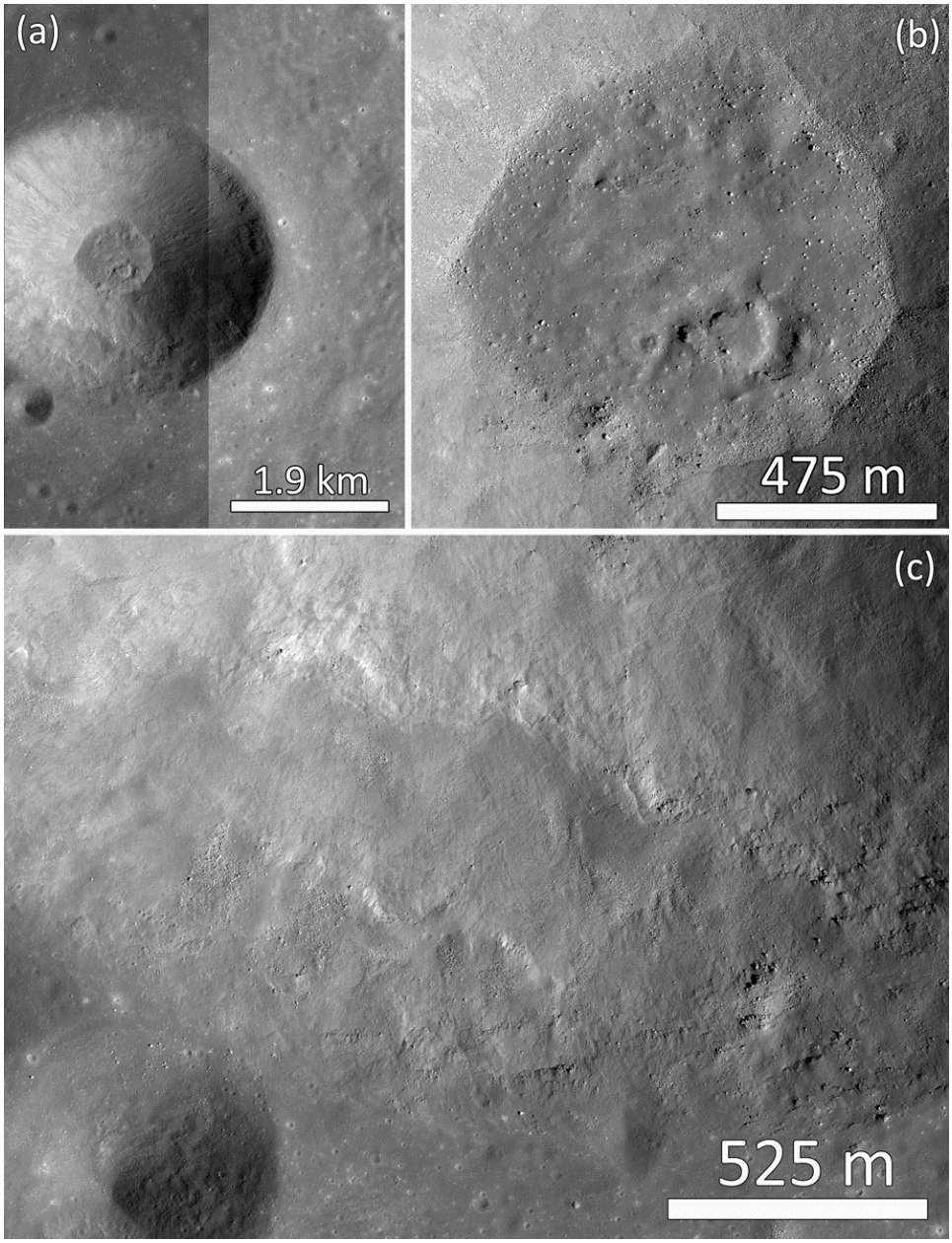

Figure 3.10. (a) A 3.8 km primary crater in the southern part of Mare Imbrium (Primary Region 4; LROC NAC M144694133RC). (b) The floor of this crater is filled with smooth material with a slightly lower albedo than the surrounding crater materials. (c) Dark, smooth material slumps into the crater from the southwest. The lobate margins of this dark unit are characterized by an increase in blocky clasts.

may have splashed over the southern and western rims of this crater. Patches of smooth, dark material are present on these interior walls. However, as the contrast between the dark and light regions is subtle, the change in albedo in these regions may be due entirely to lighting conditions. As observed at the other primary craters, the lobate margins of this smooth material exhibit concentrations of blocky clasts.

The smooth material on the floor of the north crater is even less pronounced than at the south crater. It is worth noting that the small impact craters here and on the south crater melt pond display very subdued morphologies with shallow depth-to-diameter ratios. Unlike the narrow striations of dark and light material on the interior rims of the highland craters, the deposits on the interior of the north crater form laterally continuous sheets with lobate margins (Figure 3.10). As we saw at the other primary craters, the blocky material is concentrated on these margins.

3.3.2.5 Summary of Primary Crater Morphologies

In summary, the five primary craters examined in this study shared several common morphologies:

(1) **Melt ponds.** The highland craters exhibited darker melt relative to the other crater materials than observed for the mare craters. This difference may be the result of the overall lower albedo of the mare, which would reduce the contrast between the dark melt and the surrounding material. Dark material was also observed on the rims and interior walls of these craters, both as upward splashes and as downward flows. In some instances, the ponded melt

at the floor of these craters exhibited cracks, which we attribute to contraction during cooling.

(2) Standard depth/diameter ratios. In particular, the rims of these craters displayed sharp boundaries and sometimes even local scarps (of heights of tens of meters) where rim material has collapsed into the crater.

(3) Blocky rim material. Blocks near the rims of these craters tended to be azimuthally evenly distributed around the crater planform. This blocky material ranged in size from the edge of resolution in the NAC images to large blocks with diameters greater than ten meters. In some cases, blocky material was observed in ray-like concentrations extending radially away from the crater. Blocky material was also observed on the interior walls of these craters. The wall blocks appear to have been subjected to a number of sorting mechanisms. Typically, larger blocks were concentrated nearer to the crater floor than small blocks. As we will see later, the distribution of blocky material at these primary craters is in contrast to the distribution of blocky material at the Tycho secondary craters.

(4) Azimuthally symmetric radar CPR enhancements. Each of these five craters displayed azimuthally symmetric CPR enhancements at 13-and 70-cm. These enhancements extended no more than a few crater radii from the impacts. The 13-cm signatures always extended further from the crater than the 70-cm signatures. This difference likely represents the original distribution of scatterers. 70-cm scatterers are larger and thus will not be launched as far from the crater as 13-cm scatterers, given the same ejection energy. Therefore,

they are likely to be concentrated closer to the crater, resulting in a more compact CPR enhancement at 70- than 13-cm.

These observations reveal that small, fresh primary craters with symmetric CPR enhancements possess a common group of morphologies. They are sharp-rimmed and bowl shaped, with the exception of some flattening of the floors of primary craters were impact melt has pooled and solidified in dark ponds. This melt is observed in splashes up the sides of these kilometer-sized primary craters. It also flowed back down the interior crater walls toward the crater floor, leaving lobes of dark material with raised margins. Block-rich material is common on these margins. Blocky material was also observed in ray-like clusters extending radially away from these kilometer-sized craters. As we will see in the following sections, the location of blocky material around and inside of these primary craters is very different from the location of blocky material observed at secondary craters of similar size with radar CPR enhancements. Similarly, the lack of regional-scale patterns in the areas of background CPR is a distinct contrast to the frequent lineations and networks of parallel dunes which we will see are common in regions of secondary craters with CPR enhancements. Having identified the morphologies in these "control" regions, we will now characterize the morphologies of several groups of Tycho secondary craters over a range of distances from the parent crater.

3.3.3. Secondary Cratering

Two criteria were used to select suitable regions of study containing secondary craters. Candidate regions exhibited elevated radar CPR values at 13-cm, similar to those described at Newton and Newton-A by *Wells et al.* (2010). Regions were also

chosen that exhibited classic secondary crater morphologies. These included elliptical planforms, shallow floors, herringbone/concentric dunes, braided terrains/radial ridges, and spatially clustered craters. Many regions within the rays of Tycho and Copernicus craters satisfied these conditions. Of these, I looked in detail at five regions varying in distance from just outside of Tycho crater's continuous ejecta blanket to 27 Tycho radii downrange. Regions were chosen at a variety of distances from the parent crater in order to observe any potential changes in morphology due to impact energy or angle. In increasing order of radial distance from Tycho crater, the regions selected were Tycho, Maginus, Clavius, Lilius, and Newton (Figure 3.3).

3.3.3.1 Tycho Region

The Tycho region is located very near to Tycho crater, just outside of the continuous ejecta blanket, a distance of about two crater radii (Figure 3.3, Table 3.4). At a distance of 150 km from Tycho crater, these secondary craters formed at low velocities and have corresponding "classic" secondary crater morphologies. At WAC scales, the secondary craters in these chains have sharp uprange rims and heavily degraded or completely eroded downrange rims (Figure 3.11). They also have prominent uprange v-shaped dunes which point back toward Tycho crater. The orientation of these dunes is consistent with the concentric dunes described by *Morrison and Oberbeck* (1975).

At NAC scales, the terrain around these secondary craters is very smooth (Figure 3.12). For the purpose of this work, we define smooth as "lacking in blocky clasts on the 1-10 m-scale." The smooth material fills these crater floors in the form of hummocky deposits. The rounded and filled morphologies of these craters are

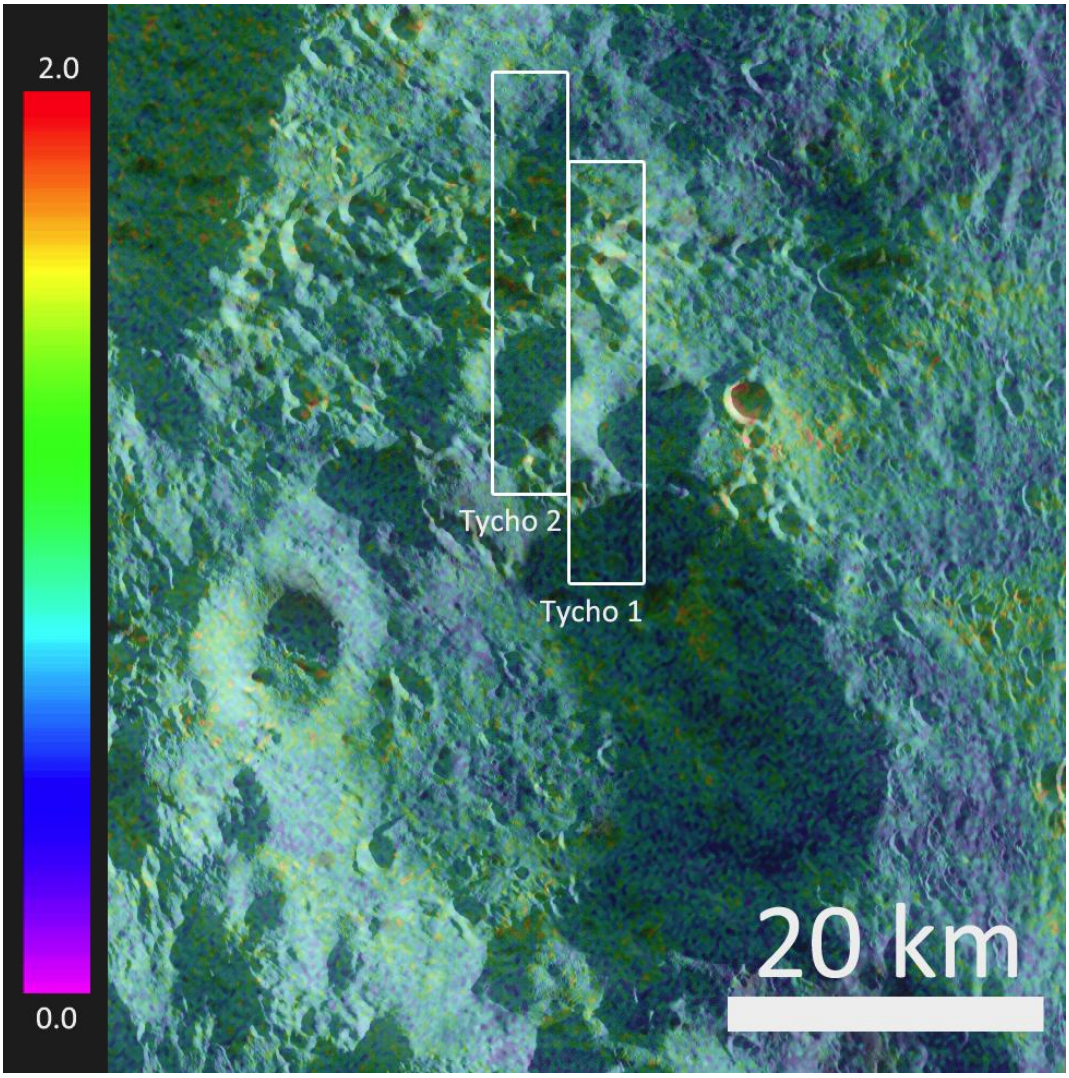

Figure 3.11. Tycho region context; 13-cm radar CPR map overlaid on LROC WAC product M116345123MC. This area is located east of Tycho crater, just outside of the continuous ejecta blanket. Elevated values of CPR accompany the Tycho secondary crater chains in these regions.

Table 3.4. NAC product data for Tycho Region

Product ID	Group	Resolution (m/pixel)	Center Latitude	Center Longitude
M109264593L	Tycho 1	0.52	-45.37	355.14
M109264593R	Tycho 1	0.52	-45.37	355.03
M155266941L	Tycho 2	0.50	-45.27	354.8
M155266941R	Tycho 2	0.50	-45.26	354.9

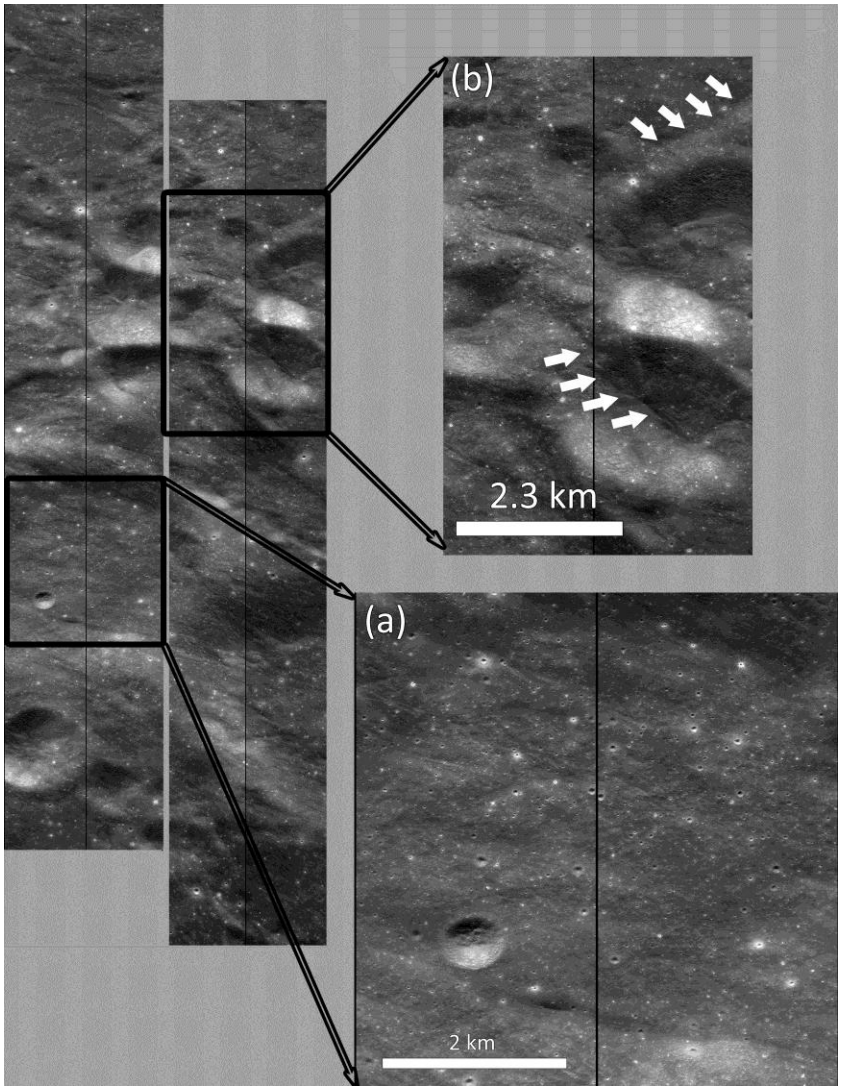

Figure 3.12. Tycho region (LROC NAC M109264593LC and RC; LROC NAC M155266941LC and RC. (a) Smooth terrain lacking 1-10m sized blocks. (b) An example of uprange v-shaped dunes.

consistent with the debris surge hypothesis of *Morrison and Oberbeck* (1975), as a debris surge could have scoured and smooth the terrain in this region after the initial passage of the ejecta curtain formed the secondary craters themselves. Many sub-parallel downrange lineations are present in these smooth units, similar to those described earlier at Control Region 1 (Figure 3.12). Unlike in Control Region 1, the lineated terrains in this region are areas of CPR enhancement.

This region has a strong CPR enhancement at 13-cm and a weak enhancement at 70-cm (Figure 3.11). In this context, the lack of blocky material in and around this secondary cluster is somewhat surprising. In regions of enhanced CPR, we would expect to find scatterers on the radar wavelength scale, which would be 13- and 70-cm sized clasts in this case. However, as we just described, there is a noticeable lack of meter-sized blocks in the NAC images of these craters. Any decimeter-scale blocks would be below the size resolution of the NAC products, so it is possible that the scatterers responsible for the 13-cm enhancement are present on the surface but not visible in these images. One explanation for the 70-cm enhancement but a lack of meter-sized scatterers in the NAC products is that the scatterers responsible for the 70-cm CPR enhancement are buried below the surface.

In summary, the small-scale morphologies of these proximal Tycho secondary craters are consistent with the emplacement of a dense cluster of secondary craters followed by a ground-hugging flow of material that rounded the rims of these craters and deposited smooth material around their rims and on their floors. Despite radar CPR enhancements at 13- and 70-cm in this region, the NAC images provide no visual evidence of an abundance of radar wavelength-scale sized scatterers. In fact, a dearth

of clasts on this size scale is observed compared to the distribution of blocky material at similarly-sized primary craters.

3.3.3.2 Maginus Region

The next region downrange from Tycho crater is the Maginus region (Figure 3.13, Table 3.5). This region is southeast of Tycho crater at a distance of about 200 km from Tycho. The Maginus region was chosen to investigate because a number of Tycho secondary crater chains with radar CPR enhancements lie along the floor of the Maginus basin. These chains are readily apparent at the WAC scale, as we can see in the WAC and CPR overlay figure (Figure 3.13). The CPR enhancements associated with these chains are wedge-shaped, beginning uprange of the first craters in the cluster and circumscribing the cluster rims. This is very similar to the relationship between the regions of enhanced CPR and isolated secondary crater chains seen at Stölfer crater in Control Region 1. The CPR enhancements at these clusters also match up with the position where we would expect to find concentric dunes like those hypothesized by *Oberbeck and Morrison* (1975).

In the following regions, we have investigated a number of different terrain types associated with these clusters. Using NAC products, we investigated the small scale features associated with the braided terrains, uprange dunes, and rounded rims.

3.3.3.2.1 Maginus Region 1

Maginus Region 1 is located in the heavily cratered terrain to the east of Maginus basin. At WAC scales, this region is primarily smooth with a few degraded

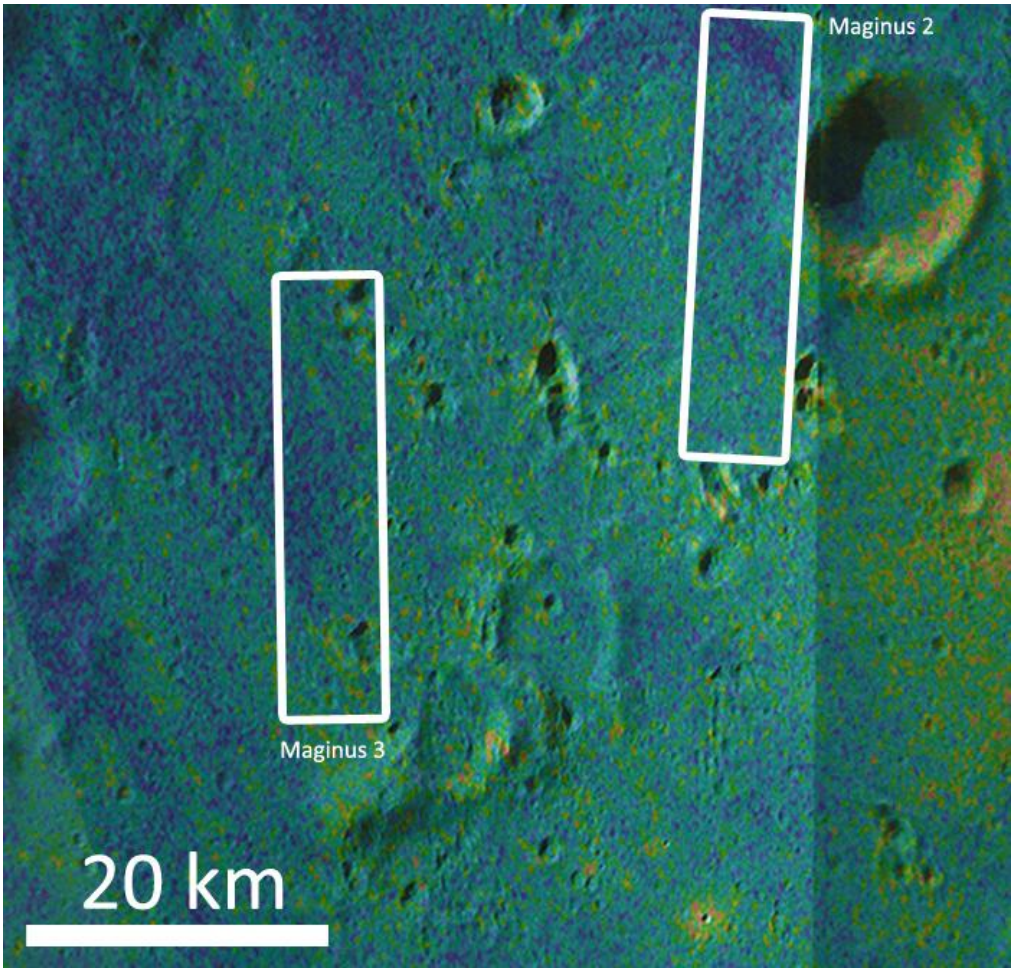

Figure 3.13. WAC/CPR overlay of the Maginus region (LROC WAC M119882141ME AND M119888937ME).

craters on the several-kilometer size scale. The exceptions are two long, linear but otherwise isolated clusters of Tycho secondary craters in the central and southern-most part of the images. The linear clusters have associated radar CPR enhancements at 13-cm but the rest of the image area displays background CPR levels. There is no 70-cm CPR enhancement in this region.

At NAC scales, the central secondary cluster is composed of v-shaped gouges where the v's point back to Tycho. The southern secondary cluster is also composed of gouges with well-developed herringbone ridges. As observed in the Tycho regions, there is a dearth of blocky material at both secondary clusters in Maginus Region 1, despite the CPR enhancements at 13-cm (Figure 3.14).

3.3.3.2.2 Maginus Region 2

Maginus Region 2 is located in the northeastern part of the Maginus basin floor (Figure 3.13). This area lies just north of a chain of prominent Tycho secondary craters, with a moderate CPR enhancement at 13-cm but weak enhancement at 70-cm. The Tycho secondary crater chain in this region is composed of kilometer-sized craters with steep uprange rims and poorly defined downrange rims, as well as shallow floors and herringbone dunes (Figure 3.15). Just to the west of the part of this region covered by the NAC products is another Tycho secondary cluster with well-developed braided terrain downrange. The downrange-most part of the disturbed terrain associated with this cluster is visible here in Maginus Region 2 (Figure 3.15).

Another cluster of shallow Tycho secondary craters is located in the northwestern corner of this region. These craters appear extremely subdued in the

Table 3.5. NAC product data for Maginus Region

Product ID	Group	Resolution (m/pixel)	Center Latitude	Center Longitude
M124551230L	Maginus 1	0.51	-48.61	3.14
M124551230R	Maginus 1	0.51	-48.6	3.26
M139939268L	Maginus 2	0.52	-48.91	355
M139939268R	Maginus 2	0.52	-48.91	355.12
M142307393L	Maginus 3	0.51	-49.37	353.7
M142307393R	Maginus 3	0.51	-49.38	353.59

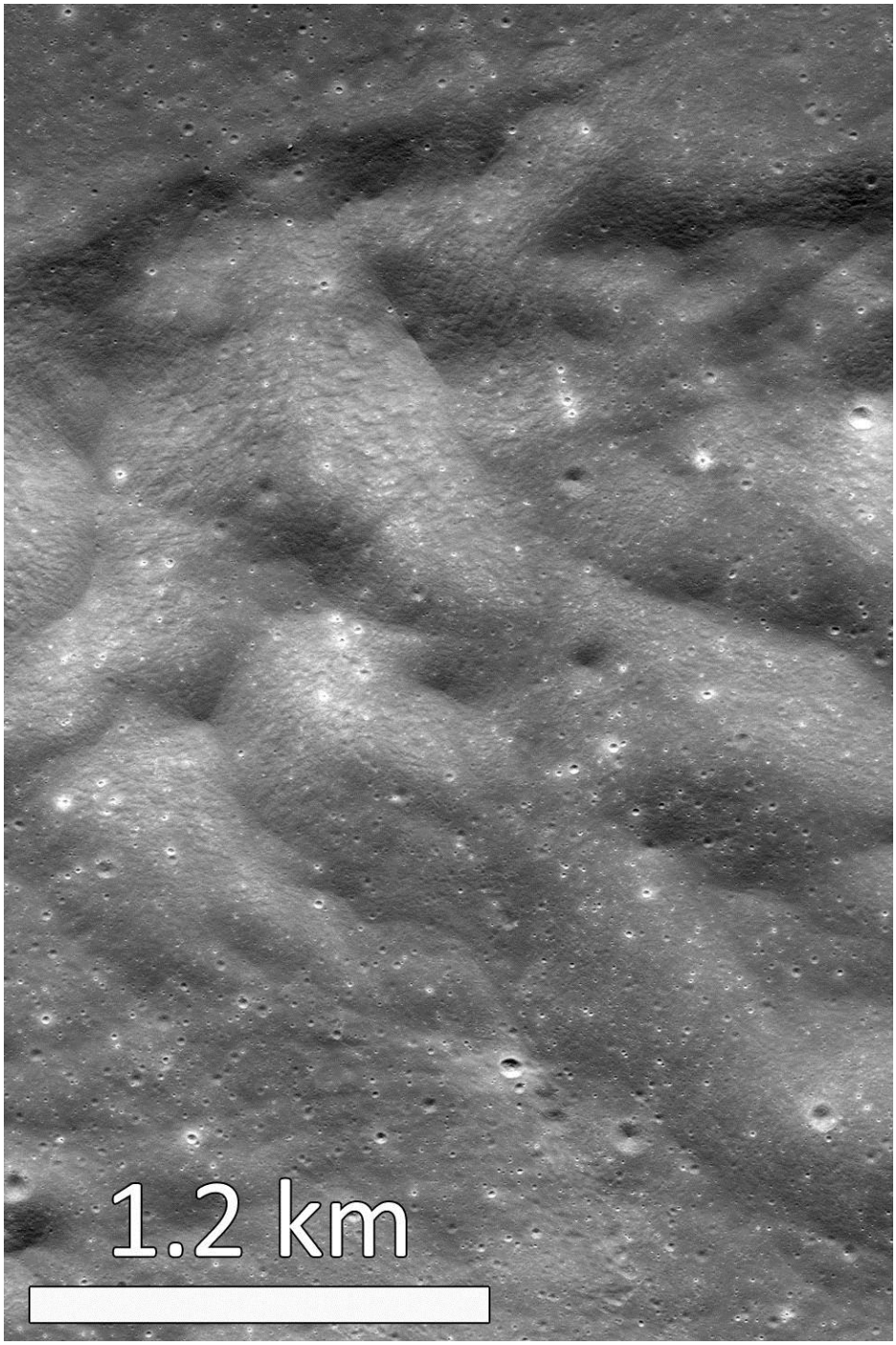

Figure 3.14. An example of smooth terrain downrange from the Tycho secondary craters in Maginus Region 1 (LROC NAC M124551230LC).

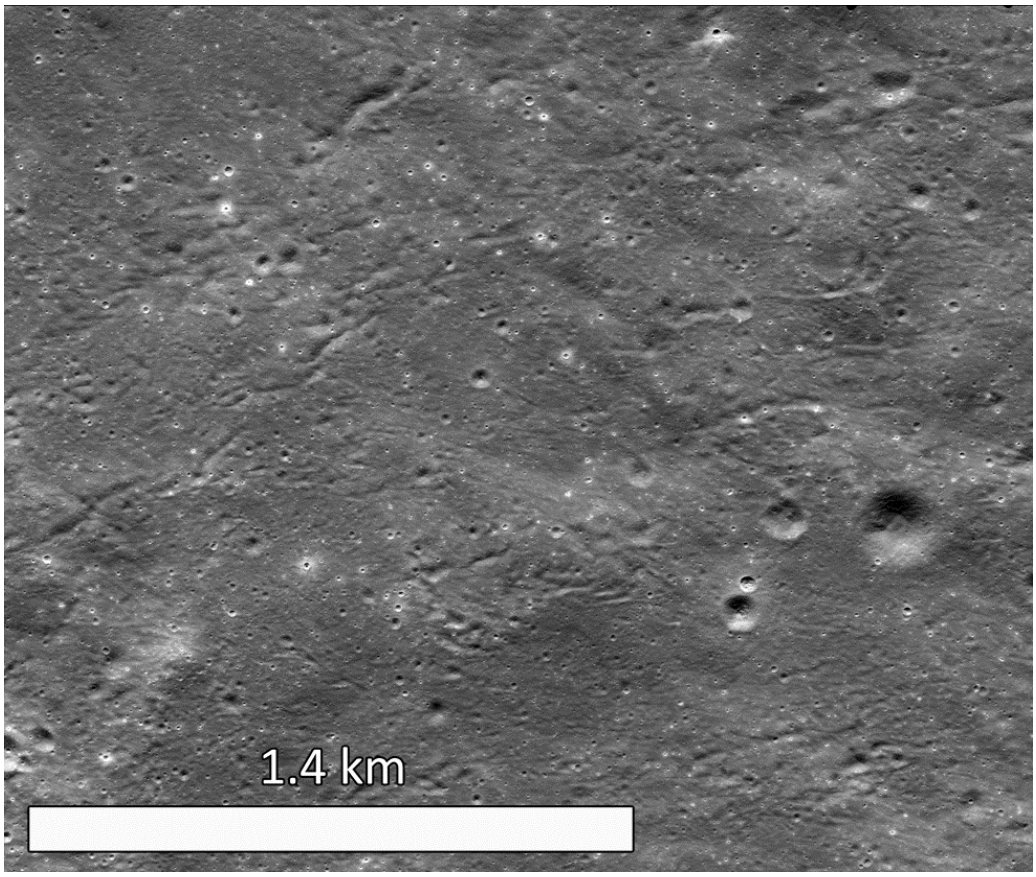

Figure 3.15. Maginus Region 2 (LROC NAC M139939268LC). Examples of unusual arcuate troughs just uprange from the herringbone dunes of a cluster of kilometer-sized Tycho secondary craters.

NAC products, due to their shallow floors and degraded rims. They appear more like downrange-elongated gouges with scalloped planforms than true craters when viewed at the NAC scale. Many of the very shallow "crater" features in this region appear to have been filled by a smooth, dark material. Despite the CPR enhancements at 13-cm, there are very few instances of block-rich terrains in these products.

As we have seen at other secondary crater clusters, numerous linear features sub-parallel to the orientation of the crater chain are observed in the heavily braided regions directly downrange from the cluster of potential shallow Tycho craters, as if material has moved downrange along the surface in these regions. Arcuate troughs tens of meters wide and tens-to-one hundred meters long are also observed in this region (Figure 3.15). These troughs appear to mimic the direction of the herringbone dunes of the downrange craters and may reflect an extension of those structures uprange.

3.3.3.2.3 Maginus Region 3

This region is located in the center of the Maginus basin, north of the central peak complex (Figure 3.13). Maginus Region 3 covers three separate secondary crater clusters. In the northeast part of the region is a group of three kilometer-sized craters with degraded rims. In the southeast is another group of kilometer-sized craters with heavily degraded rims. In the central portion of the images are a handful of smaller craters with what appear to be sharp, herringbone uprange rims at WAC resolution and shallow, heavily degraded downrange rims (Figure 3.16). This is a region of radar CPR enhancement at 13-cm and very weak 70-cm enhancement (Figure 3.13).

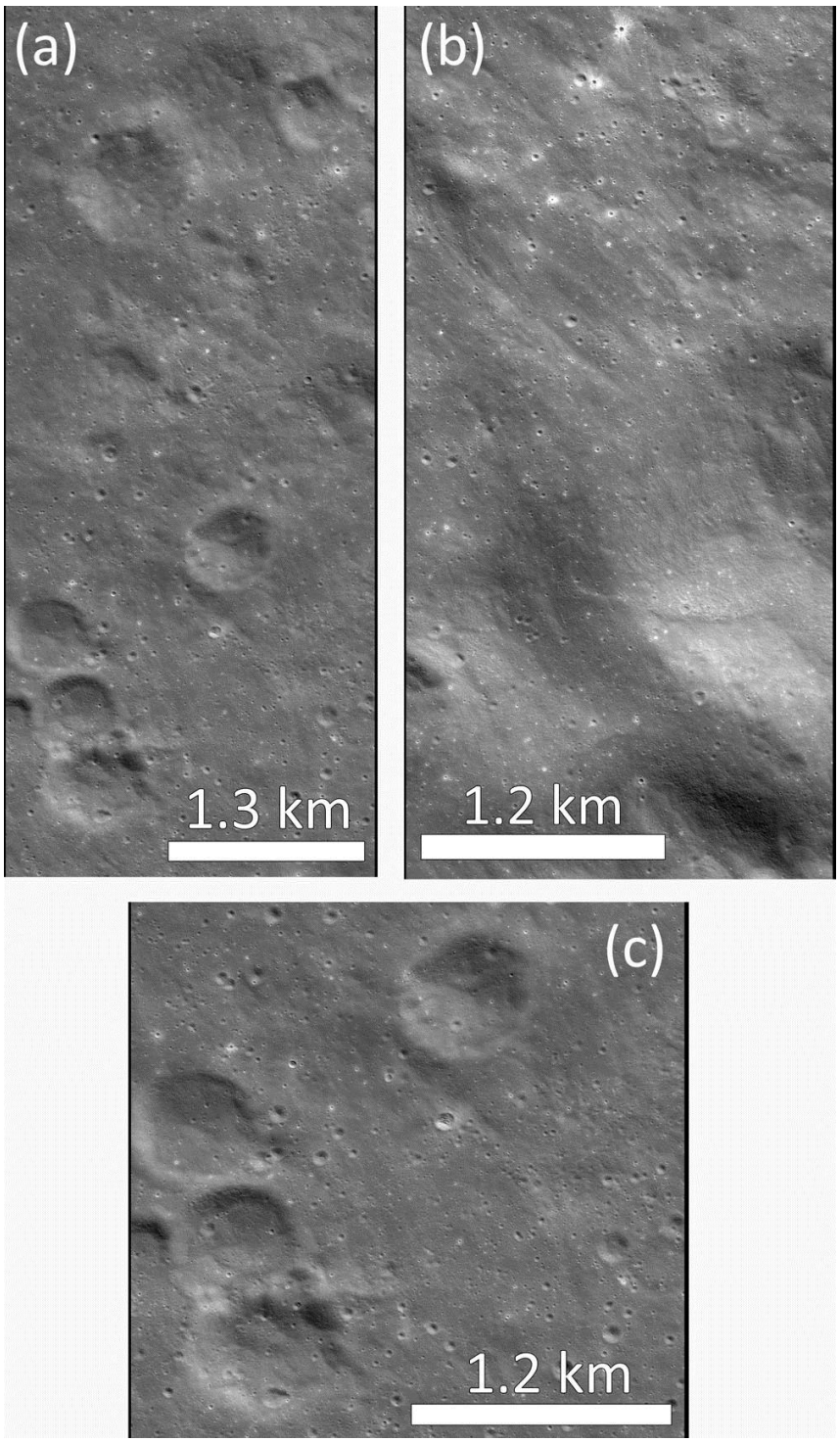

Figure 3.16. Maginus Region 3 (LROC NAC M142307393LC). (a) Examples of shallow floors. (b) Linear troughs oriented downrange. (c) Examples of degraded downrange rims.

At NAC scales, the northernmost secondary cluster appears to have been breached by a smooth material lacking 1-10 m-sized clasts. These smooth materials display linear troughs which run roughly parallel to the Tycho direction (Figure 3.16). The smooth units originate outside of these heavily degraded craters and fill their floors, leaving hummocky, smooth deposits. The uprange rims of the smaller of these two craters have been almost completely obliterated by these smooth units.

At high-resolution, the central cluster of craters also appears to have been breached by the smooth material (Figure 3.17). As a result, these craters are very shallow, with scalloped planforms. In some instances, blocky debris sits on the rim of one of these craters (Figure 3.17). It is partially buried by the smooth material and occurs on the margin of one such smooth unit.

The south cluster is also breached from the uprange direction by the smooth material (Figure 3.17). The Tycho-facing rim is heavily degraded by the flow of the smooth material over the rim crest and into the crater, resulting in a hummocky floor deposit. Throughout this region, these smooth flow morphologies and heavily degraded rims are consistent with debris flow modification of the secondary craters.

While smooth terrains dominate the secondary clusters in Maginus Region 3, blocky material is also observed in isolated pockets (Figure 3.17). These concentrations of blocks are most common on the interior of secondary crater walls in this region, where they extrude from the smooth material as if they have been partially buried.

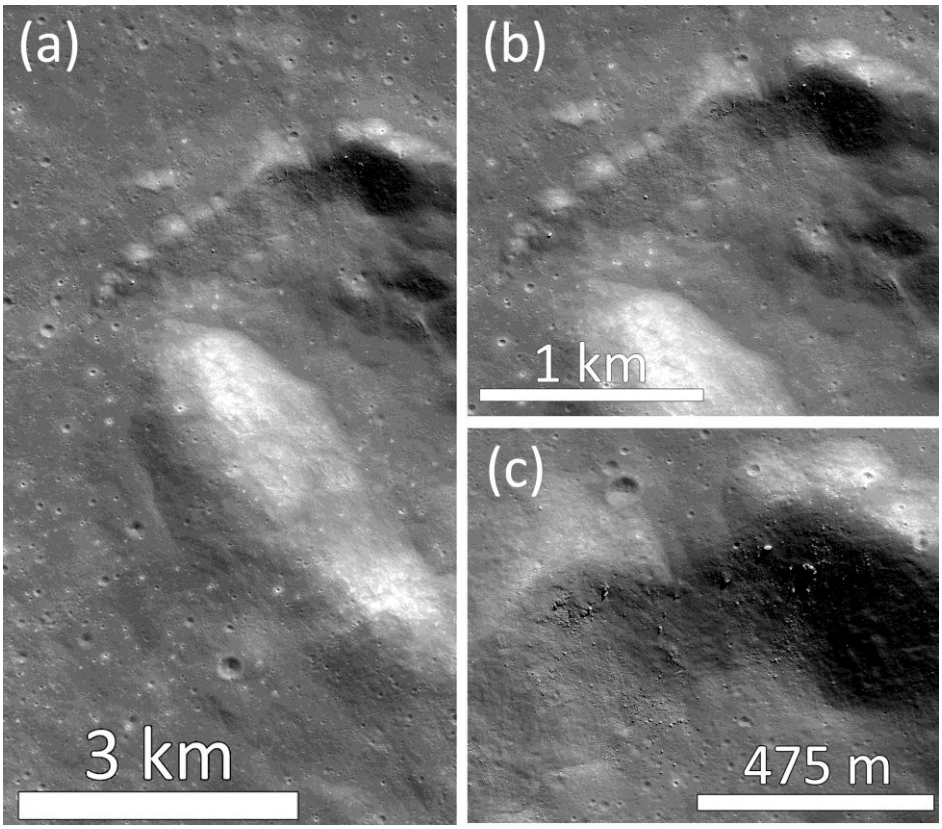

Figure 3.17. Maginus Regions 3 (LROC NAC M142307393LC). (a) The breached uprange rim of a large Tycho secondary crater on the floor of the Maginus basin. (b) Smooth material forms a channel on the north part of the rim and flows toward the crater floor. (c) An example of a typical contact between smooth flows and blocky material.

3.3.3.2.4 Summary of Maginus Regions

Much as we saw at the proximal secondary craters in the Tycho region, the morphologies observed at the secondary craters in the Maginus region are indicative of debris flow. Smooth material appears to have flowed over or around many of the secondary crater rims, resulting in rounded or subdued rim morphologies on the NAC scale, well-developed uprange dunes pointing back in the Tycho direction, open downrange rims, and crater floors with hummocky textures. Braided terrains appear in the intercrater regions of these clusters, with the pattern extending from ridges and troughs down to fine lineations. These regional-scale patterns are consistent with interference patterns in a downrange debris flow, where deflection of the flow around or over topographic obstacles such as secondary crater rims dictates the geometry of the textured pattern. The presence and location of isolated clusters of blocky material are also consistent with this interpretation. These blocky regions are commonly found at the crests and on the interior walls of the uprange rims of the Tycho secondary craters in the Maginus region. If this blocky material were transported downrange by debris flows, we would expect them to be preferentially deposited in regions of low flow velocity or those shielded from the flow. Rim crests and uprange interior crater walls fit this description.

To this point, we have seen that debris flow can explain the morphologies observed at Tycho secondary clusters in regions of 13-cm radar CPR enhancement out to distances of 350 km (8 crater radii) from the parent crater, Tycho. We now

continue our investigation at greater distances by examining a collection of Tycho secondary crater clusters in the Clavius and Lilius regions.

3.3.3.3 Clavius and Lilius Regions

The Clavius basin (D = 225 km) is located in the lunar southern highlands at distance of about 500 km from Tycho crater (Figure 3.18, Table 3.6). Lilius crater (D = 61 km) lies approximately 350 km to the east (Figure 3.19, Table 3.7). Based on counts of craters with D>20 km identified in LRO LOLA digital elevation models, *Head et al.* (2010) identified this region as one of the oldest on the lunar near side.

The youngest large feature in this region is Rutherfurd crater (D=48 km), which straddles the southeast rim of Clavius. The USGS map places Rutherfurd's ejecta blanket stratigraphically above the high-albedo Tycho ray that crosses Clavius from the north to south, putting bounds on the maximum age of Rutherfurd at ~100 Myr [*Cummings*, 1972; *Arvidson et al.*, 1976]. The Rutherfurd ejecta blanket features prominently in the 13-and 70-cm radar maps as CPR enhancements. To avoid confusion between features related to Tycho and features related to Rutherfurd, regions within the continuous ejecta blanket of Rutherfurd crater were not used in this work.

The USGS geologic map of the Clavius Quadrangle describes this region as ancient highlands terrain and maps numerous units of "crater materials". It also identifies a group of intercrater units that it attributes to flow, possibly of ash or other volcanic material [*Cummings*, 1972]. While the theories of widespread highlands volcanism are no longer viable [*Head*, 1976], these units are spatially correlated with

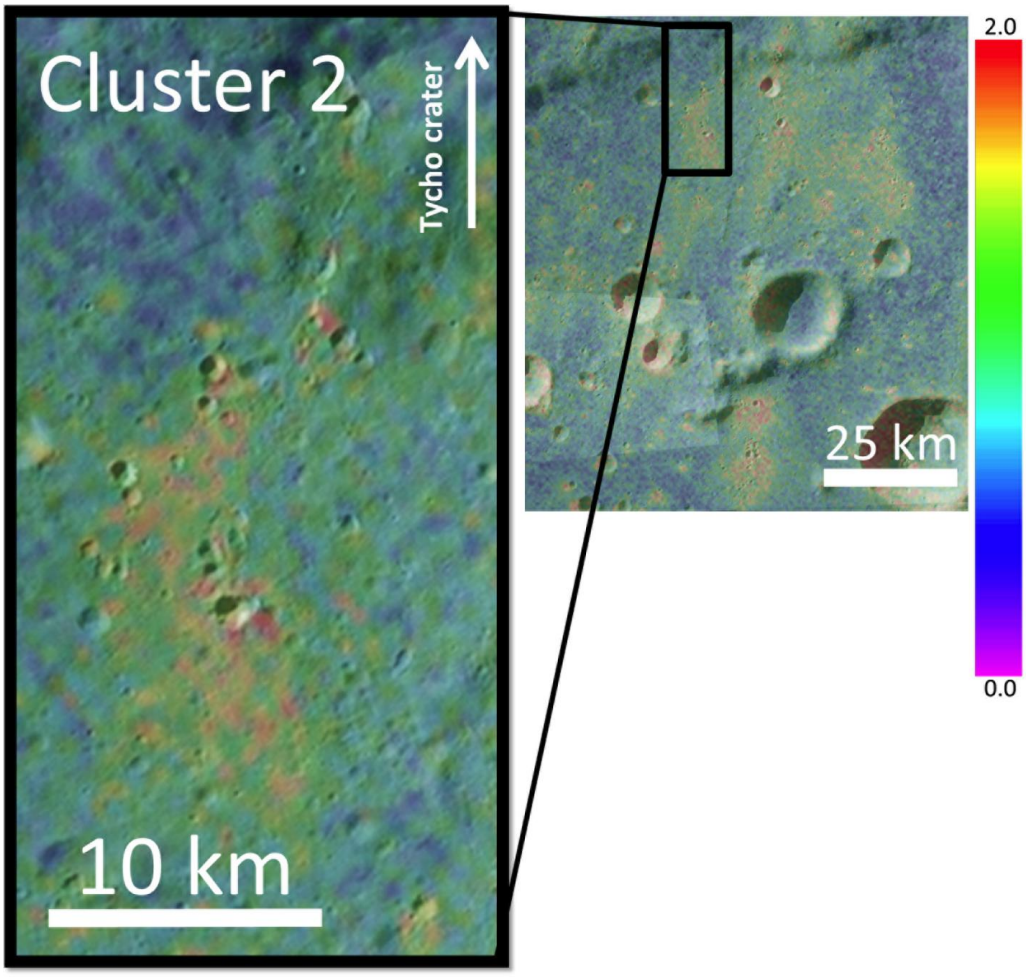

Figure 3.18. Clavius Region WAC/CPR overlay (LROC WAC M119936429ME and M119983943ME). "Cluster 2" and Clavius Region 1 refer to the same cluster (LROC NAC M111688776RC). Note the radar CPR enhancements downrange from the secondary craters in this cluster.

Table 3.6. NAC product data for Clavius Region

Product ID	Group	Resolution (m/pixel)	Center Latitude	Center Longitude
M111688776L	Clavius 1	0.51	-55.87	344.71
M111688776R	Clavius 1	0.51	-55.87	344.58
M119956786L	Clavius 2	0.54	-58.87	344.98
M119956786R	Clavius 2	0.54	-58.87	345.14
M119916160L	Clavius 3	0.51	-53.9	350.86
M119916160R	Clavius 3	0.51	-53.9	350.94
M157647899L	Clavius 4	0.50	-54.44	351.42
M157647899R	Clavius 4	0.50	-54.44	351.3

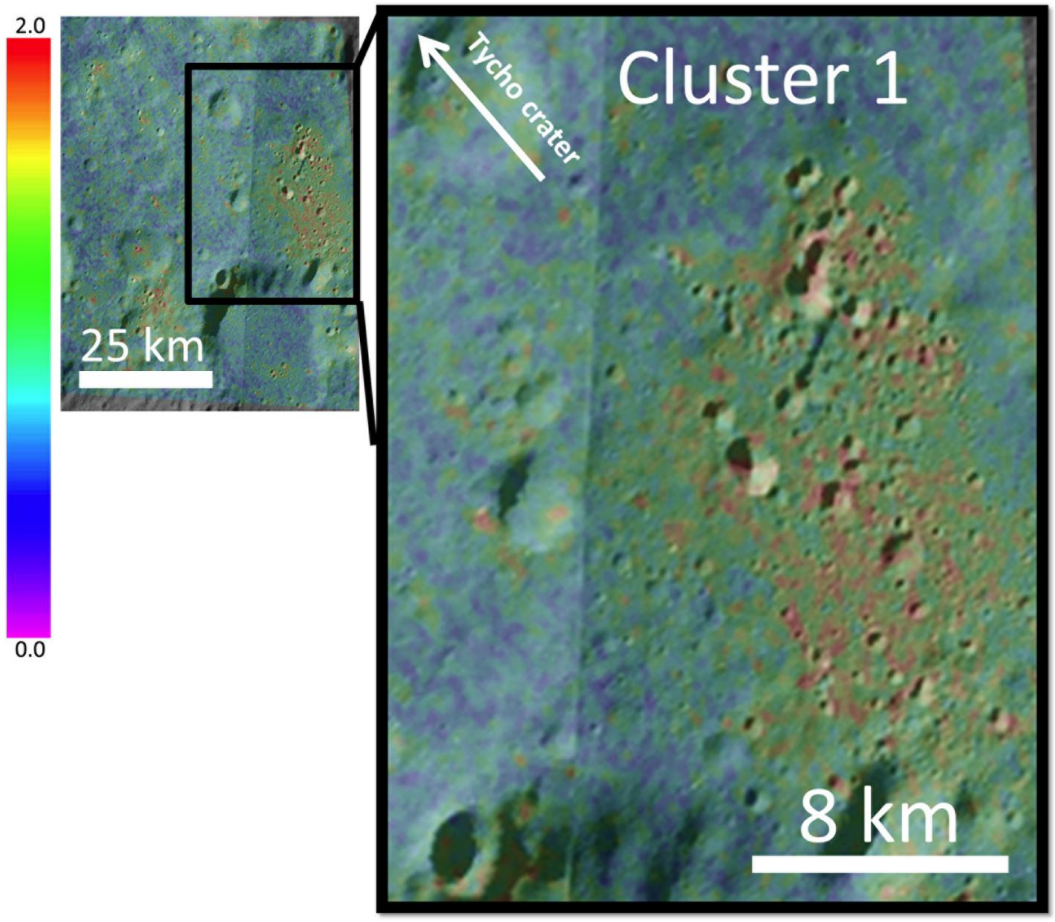

Figure 3.19. Lilius Region WAC/CPR overlay. "Cluster 1" and Lilius Regions 1 and 5 refer to the same cluster (LROC WAC M119827848ME).

the presence of enhanced 13-cm radar CPR at Tycho crater clusters, indicating that the mapped flows may be related to impact cratering rather than volcanic process.

3.3.3.3.1 Clavius Region 1

Clavius Region 1 is located in the north-central portion of the Clavius basin. It is near the northern rim of the basin but lies on the flat basin floor. This region has a strong radar CPR enhancement at 13-cm and a moderate enhancement at 70-cm (Figure 3.18). At WAC resolution, two clusters of kilometer-sized craters are visible in this area. The two clusters are oriented along the Tycho direction. The terrain between them is hummocky with braided terrains reminiscent of those described by other authors [*Morrison and Oberbeck*, 1975; *Lucchitta*, 1976]. At the WAC scale, these clusters are composed of a combination of craters with sharp, fresh-looking rims and some with subdued rims. The craters with subdued rims are smaller in size than the fresh-looking craters. The uprange rims of the subdued craters are steep and sharp, but they lack clearly-defined downrange rims (Figure 3.18). The subdued craters in the southern-most cluster display herringbone dunes that grade into braided terrain. There is also a third prominent cluster of what appear to be Tycho secondary craters just to the northeast of the area covered by these NAC products. These craters are characterized by steep uprange rims and a lack of clearly-defined downrange rims. They likely contribute to the braided terrains in the northeastern part of this region.

At full NAC resolution, we can see that smooth material is deposited over even the "sharp" secondary crater rims, creating subdued rim morphologies (Figure 3.20). The downrange rims of these secondary craters are more frequently eroded by smooth

Table 3.7. NAC product data for Lilius Region

Product ID	Group	Resolution (m/pixel)	Center Latitude	Center Longitude
M109203644L	Lilius 1	0.52	-55.91	4.31
M109203644R	Lilius 1	0.52	-55.91	4.16
M122196145L	Lilius 2	0.52	-56.21	2.64
M122196145R	Lilius 2	0.52	-56.2	2.78
M122202930L	Lilius 3	0.52	-56.35	1.61
M122202930R	Lilius 3	0.52	-56.35	1.76
M135189975L	Lilius 4	0.52	-56	359.79
M135189975R	Lilius 4	0.52	-56	359.93
M137517296L	Lilius 5	0.52	-55.81	4.67
M137517296R	Lilius 5	0.52	-55.81	4.81

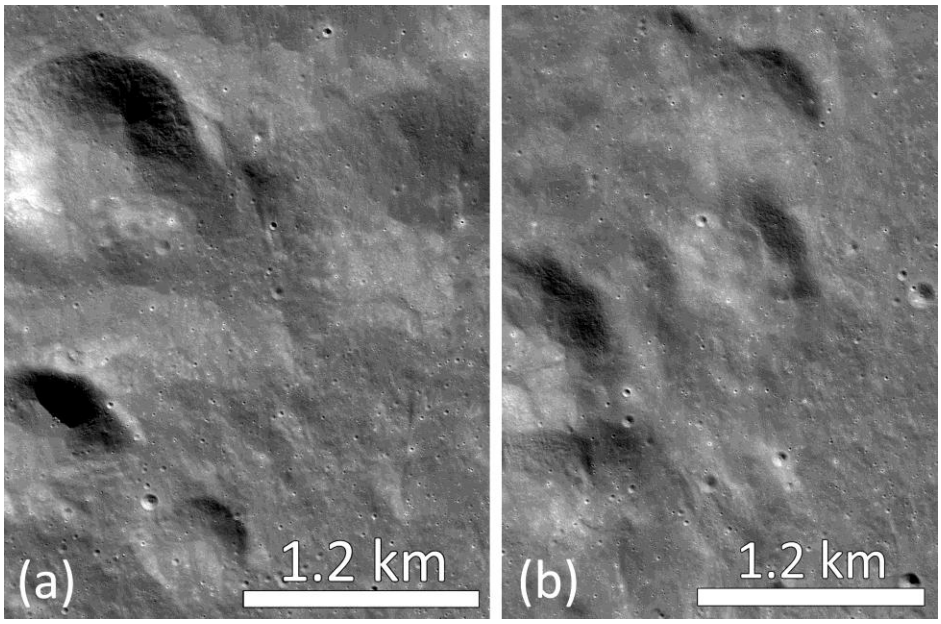

Figure 3.20. Clavius Region 1 (LROC NAC M111688776RC). (a) An example of breached crater rims in the part of the cluster closest to Tycho. (b) Craters further downrange in the same cluster. Note the gradation from crisper to more degraded crater rims proceeding downrange in the cluster.

material than the uprange rims, particularly in the cases of the craters at the uprange edge of the clusters. Further downrange, some uprange rims are also heavily eroded. The change in degradation state with distance downrange in the cluster is a common occurrence in these regions. The slow gradation of preservation from crisp rims to gouges and ridges is consistent with debris flow originating at the front of the clusters and growing in strength downrange as more material is added to the flow (Figure 3.20).

The best example of smooth terrain breaching a secondary crater in this area is the large crater in the southernmost part of the region (Figure 3.21). This crater is breached by smooth material from the east and west and appears to have experienced collapse of the interior southern rim. The eastern rim may also have undergone a significant collapse event, resulting in a double-rim and a well-defined channel of smooth material directed west toward the crater floor (Figure 3.21). This is a particularly good example of the flow nature of these deposits. On the eastern part of the breached rim of this crater, the smooth material forms a clear channel with sharp boundaries that slipstream the surrounding features. A close examination of the NAC images also reveals instances where the smooth material has flowed up the front rim of this crater and come to rest, leaving arcuate, raised margins at the downrange edge of the flow.

As we saw at the Tycho and Maginus regions, the smooth terrains in Clavius Region 1 lack blocky clasts on the 1-10 m scale. Where small blocks are visible, they are typically partially covered by smooth material (Figure 3.21). In other places, blocks appear to extrude from the smooth terrain. It is likely that the same smooth

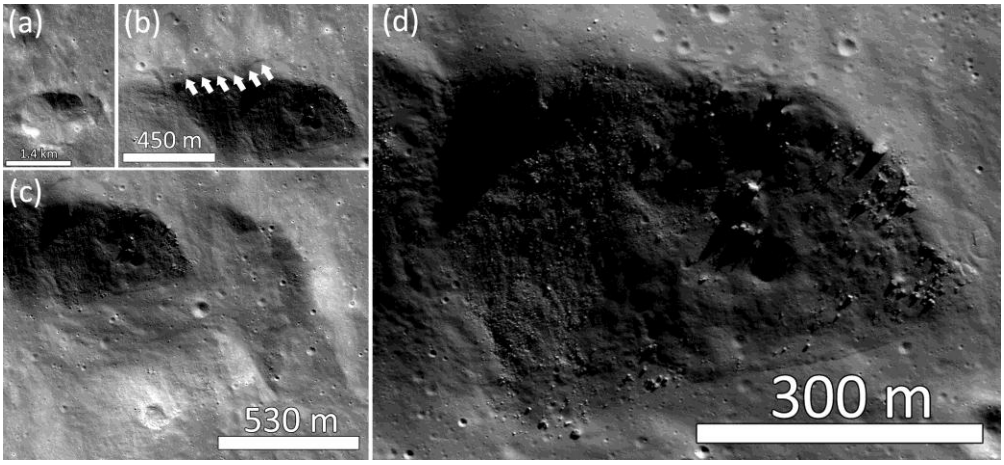

Figure 3.21. Clavius Region 1 (LROC NAC M111688776RC). (a) A 1.4 km diameter Tycho secondary crater with its rim breached by smooth material. (b) The raised margin of a deceleration dune where the smooth material slowed down going up this crater rim. (c) A sharp-edged channel of smooth material flowing down into the crater. (d) A typical contact between smooth and blocky material.

material that eroded the rims of the secondary craters in this region also buried blocky material that was ejected during secondary excavation. A block-rich layer beneath a shallow cover of smooth material would explain the presence of the small (D = 5-80 m) pitted craters in this area (Figure 3.22). Pit craters can form at any diameter given sufficient differences in target properties with depth to change the effective crater excavation efficiency [*Melosh*, 1989, pg. 82]. The small pit craters in this region appear to excavate blocky material, which also supports the hypothesis that the pits are the result of a stratified target with a buried blocky layer. These excavated blocks can be found in mounds on the crater floors and strewn outside of the small crater rims.

3.3.3.3.2 Clavius Region 2

Clavius Region 2 is located further downrange than Clavius Region 1, just south of the Clavius central peak complex (Figure 3.18). It covers a prominent cluster of Tycho secondary craters that are visible at the WAC scale. These craters also display a very clear CPR enhancement at 13-cm, as well as a moderate enhancement at 70-cm. On the WAC scale, the morphologies of the secondary craters in this cluster are similar to those of the other secondary clusters we have discussed to this point. They have sharp, steep uprange rims and subdued, heavily eroded downrange rims. At the uprange end of the cluster, the craters are very tightly clustered. They overlap so that the uprange-most craters are only uprange rims, not full craters. This cluster also features a large uprange dune at a high angle to the impact direction that circumscribes the cluster. Individual craters in the cluster also exhibit smaller v-shaped uprange dunes. The terrain to the east, west, and downrange from this cluster is

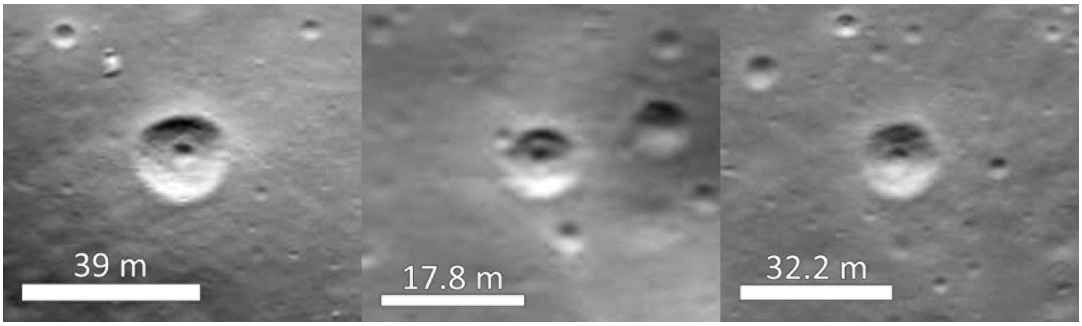

Figure 3.22. Examples of pit craters (LROC NAC M109203644LC and M109203644RC).

highly disturbed, forming a clear braided pattern. The craters downrange from the main cluster are progressively smaller and more degraded, until they give way to v-shaped ridges and braided terrain as opposed to fully-formed craters. Again, I stress that these morphologies are consistent with the passage of a rapid debris flow through this region, gaining volume and erosive power as it progressed downrange.

Another class of features in this region which can be explained with a debris flow origin are the fine lineations. At NAC resolution, a braided pattern of v-shaped ridges and lineations is prevalent throughout the region on a variety of scales (Figure 3.23). The pattern begins at the tens of meter scales and persists to the kilometer scale. The smooth material also forms dunes where it is deflected around crater rims and ridges that may be heavily eroded crater rims (Figure 3.23). As we have seen at other clusters, there is an extreme dearth of block-rich material in this region. Only the largest craters have associated blocky material, found on the interior uprange rims (Figure 3.23). Consistent with the other regions, this blocky material is partially buried in smooth material.

3.3.3.3.3 Clavius Region 3

Clavius Region 3 covers several Tycho secondary craters in the plains between Maginus-H and Clavius-B craters (Figure 3.18). I have chosen to discuss this particular cluster because at the WAC scale, the individual craters in this cluster do not appear clustered at all. Instead, the cluster is revealed based on the presence of the CPR streaks. This region has a radar CPR enhancement at 13-cm but not at 70-cm. Additionally, at the WAC scale, the craters in this cluster appear to have well-

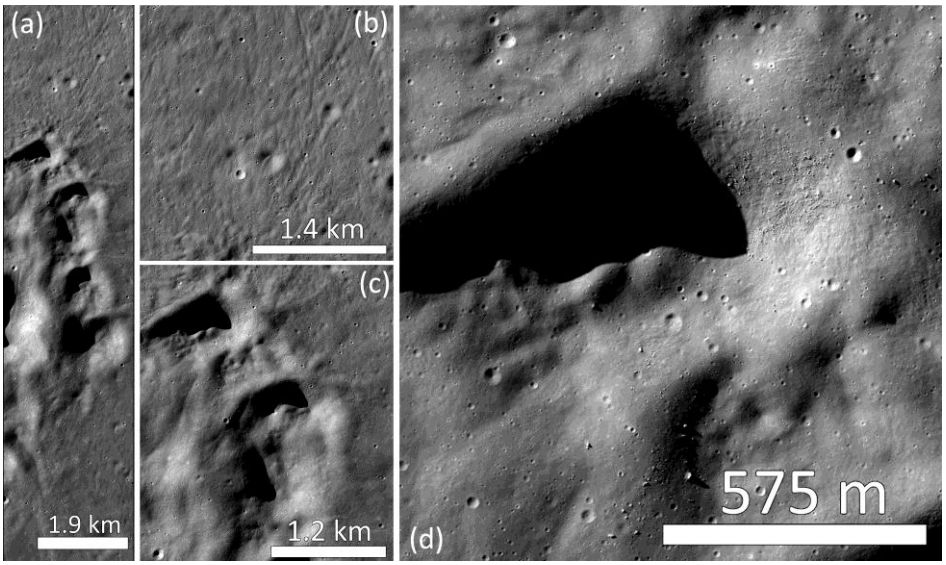

Figure 3.23. Clavius Region 2 (LROC NAC M119956786RC). (a) Cluster context. The v-shaped dunes at the tip of the cluster point back in the direction of Tycho crater. (b) An example of fine braided texture uprange from the cluster in (a). This braiding is due to another Tycho secondary cluster just uprange and out of the image. (c) Detail of the v-shaped dunes. Note the sharper rims uprange and heavily degraded downrange rims of these secondary craters. (d) Instances of blocky material are confined to areas inside the v-shaped dunes.

preserved uprange and downrange rims. There is no obvious braiding or other unusual disturbance of the surrounding terrain visible on the WAC scale (Figure 3.18).

At NAC scales, the surface near these craters is hummocky, with numerous v-shaped lineations downrange of the craters pointing back in the Tycho direction. Like the more obviously clustered secondary chains we have already investigated, this region is characterized by very smooth terrain. These smooth units drape over some of the secondary crater rims (Figure 3.24). The crater floors are filled with this smooth material, resulting in hummocky deposits on their floors. Block rich material is observed on the interior rims of some of the craters, where it is partially buried by smooth material (Figure 3.24).

The two largest craters in this region have well-developed v-shaped uprange dunes, reminiscent of deceleration dunes (Figure 3.25). Smooth material breaches the uprange rim of the two of these craters that is further downrange. The terrain directly downrange from this crater is particularly disturbed-looking. It is very interesting that we should see uprange dunes, braiding, and lineations in a collection of secondary craters that do not appear strongly clustered. If the dunes and textured patterns on the surface are indeed the result of interference in the debris surge following the primary ejecta curtain, then the presence of these features indicates that the primary ejecta was sufficiently clustered for the flow to have multiple, interfering points of origin. In other words, the fact that we see these features in a region where the secondary craters themselves are widely spaced indicates that even isolated ejecta fragments large enough to form secondary craters are accompanied by swarms of small debris. The debris appears to impart sufficient energy to the local surface to initiate debris flow,

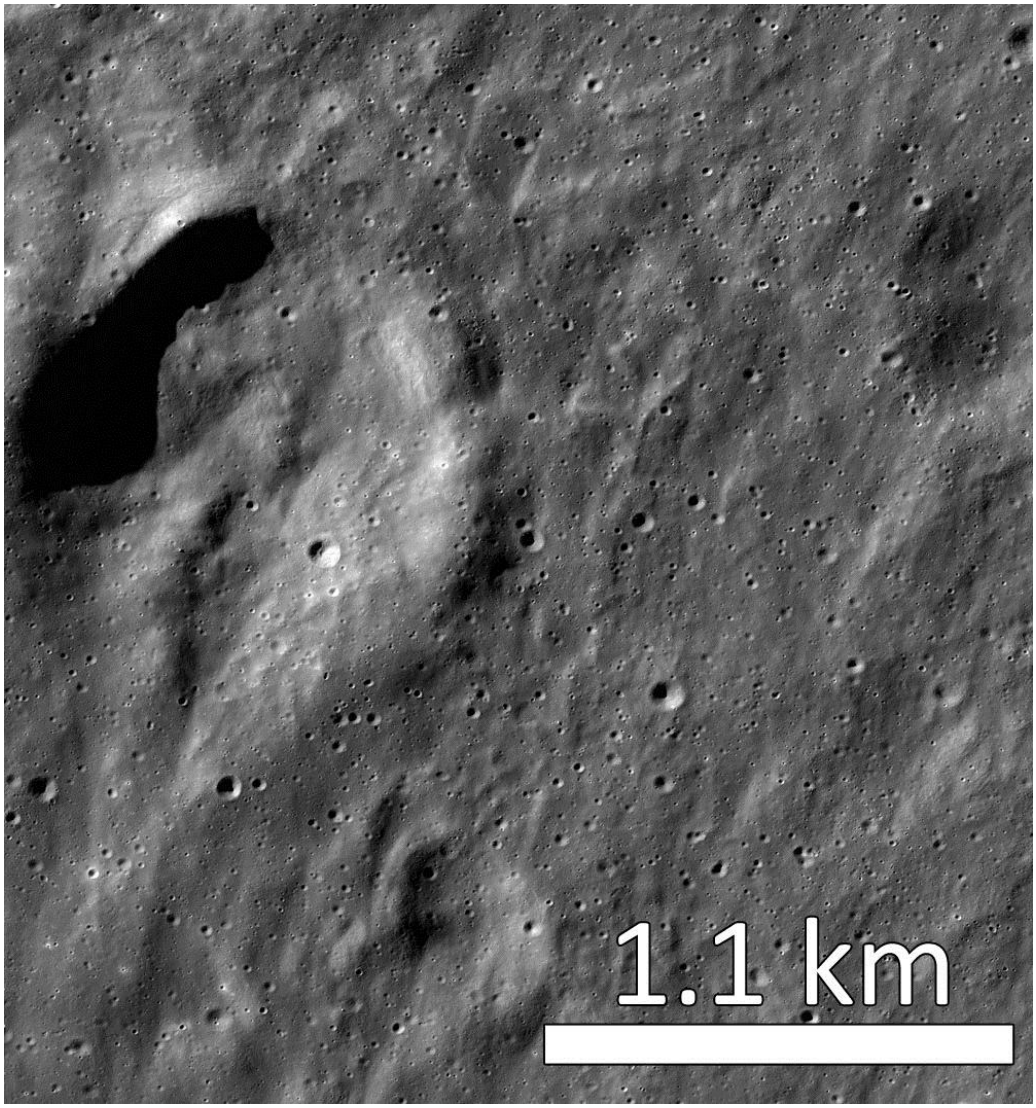

Figure 3.24. Clavius Region 3 (LROC NAC M119916160RC). Smooth material breaches the rim of this Tycho secondary crater from the northeast (uprange). This smooth material fills the crater floor and appears to have eroded the downrange crater rim.

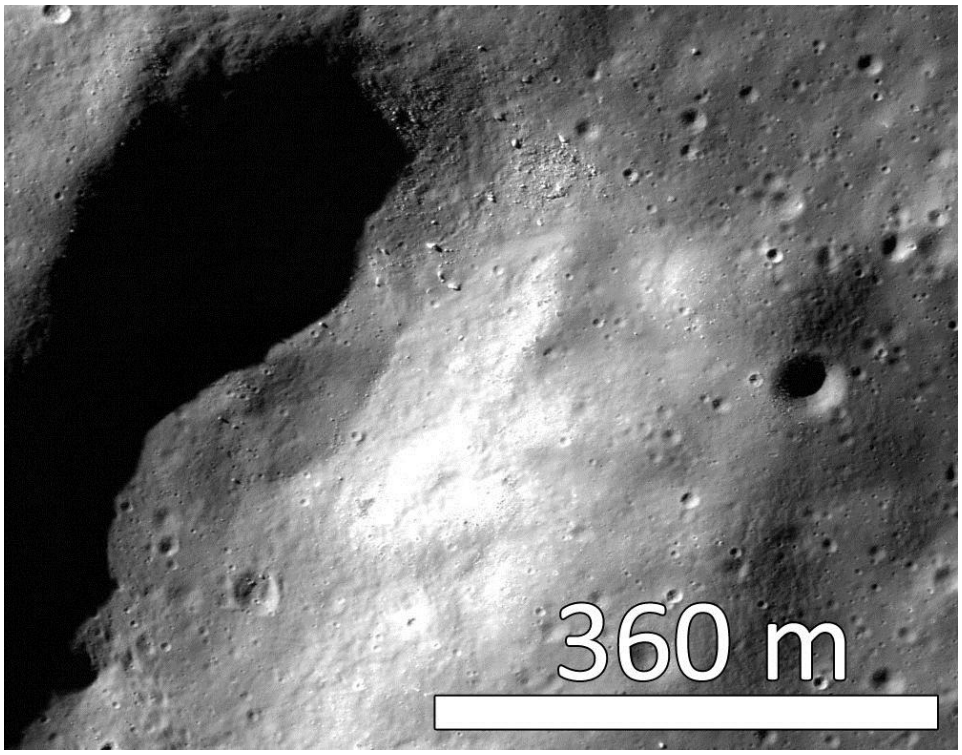

Figure 3.25. Clavius Region 3. A small Tycho secondary crater is breached from the northeast by smooth material. Block-rich material is visible on the northeastern rim and interior wall of this secondary crater.

but not enough to form craters. Downrange from the largest secondaries in a given cluster, some of these fragments may have formed small secondary craters that were subsequently obliterated by the passage of the debris flow. The presence of these flow features at widely spaced secondary craters indicates that downrange transport of local material is an important part of the secondary cratering process, even at relatively isolated secondary craters.

3.3.3.3.4 Clavius Region 4

Clavius Region 4 crosses Clavius-BB crater, a 16-km crater between Clavius-B and Maginus-H. This region has a strong CPR enhancement at 13-cm and a weak enhancement at 70-cm (Figure 3.18). A linear cluster of craters crosses the eastern rim of this crater. Even at the WAC scale, these are easily identified as Tycho secondary craters. They are strongly clustered with well-developed herringbone ridges. The uprange rims of these craters are sharper than their downrange rims.

At NAC scales, the raised v-shaped dunes uprange of these craters are apparent (Figure 3.26). The smooth material that comprises these dunes extends downrange from the v-shaped ridges. The smooth units have numerous lineations parallel to the Tycho direction, creating the impression that the smooth material flowed over the surface in this direction. Even compared to the smooth terrains identified at other clusters, the smooth terrain in this region is exceptionally smooth (Figure 3.26). Almost no 1-10 m-sized blocks are observed on the surface in these regions. Where blocks are observed, they are confined to the inside of the secondary craters, confined by the boundaries of the v-shaped ridges (Figure 3.26). As we have mentioned

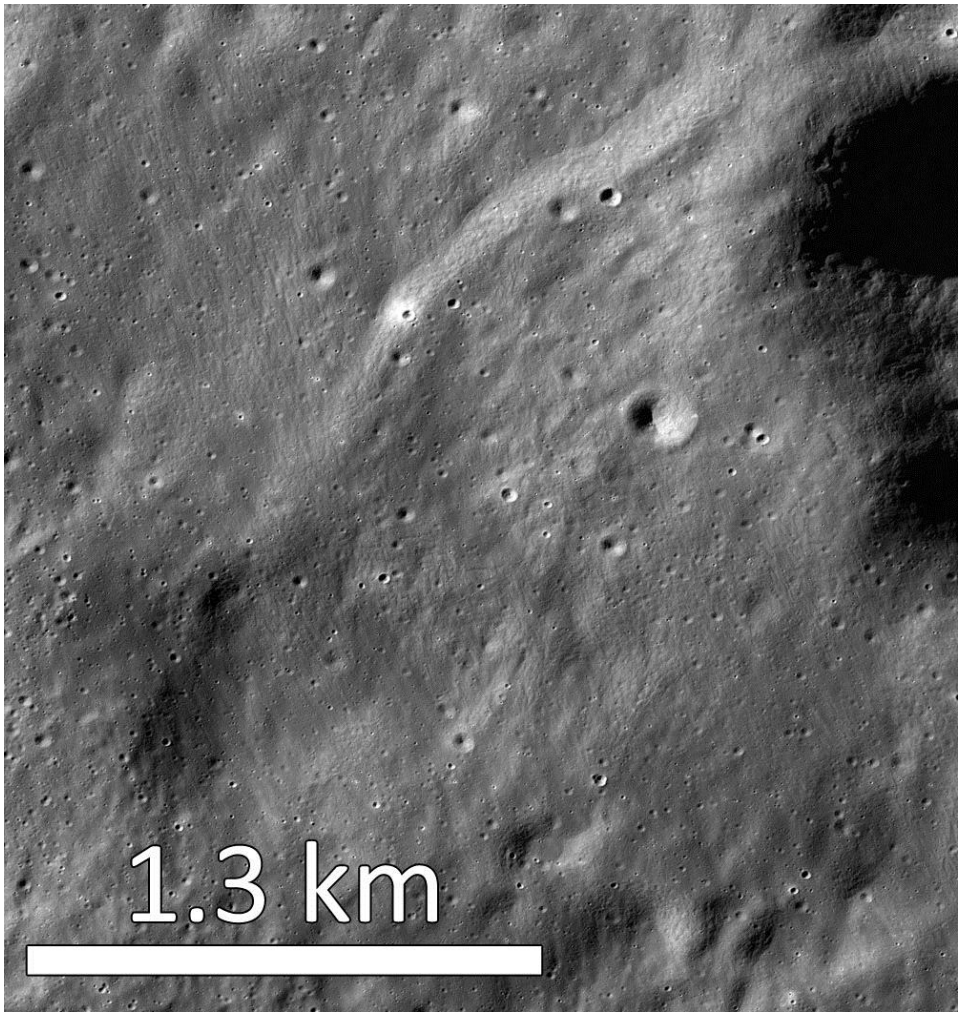

Figure 3.26. Clavius Region 3 (LROC NAC M119916160RC). One half of a raised, v-shaped dune extends southwest from the Tycho secondary crater in the upper right-hand corner of this image. Braided terrains are visible inside and downrange from the area circumscribed by the dune.

previously, the location of this blocky material is consistent with shielding of the blocks from the highest velocity debris flows by these dunes and crater rims. It is possible that we see blocks concentrated in these leeward regions because exposed block-rich material has been swept downrange by flow.

3.3.3.3.5 Lilius Region

The Lilius region is a similar distance from Tycho crater as the Clavius region, only Lilius (D = 61 km) is located approximately three hundred and fifty kilometers east of Clavius. Lilius and Clavius share similar geologic histories as part of the oldest region of highlands terrains on the lunar near side [*Head et al.*, 2010]. At WAC scales, the clusters observed in the Lilius region display excellent examples of secondary morphology. The clusters in Lilius Regions 1 and 5 display particularly prominent wedge-shaped CPR enhancements at 13-cm (Figure 3.19). These clusters also have some of the highest CPR enhancements at 70-cm of any of the craters investigated in this study.

3.3.3.3.5.1 Lilius Region 1

Lilius Region 1 covers a cluster of large Tycho secondary craters on the relatively flat plain to the southwest of Lilius crater (Figure 3.19). The diameter of the largest crater in this cluster is 2.0 km. The larger craters in this cluster are located to the northwest of the group. Further to the southeast, the cluster is composed of smaller craters. At WAC scales, some of these smaller craters have sharp, well-defined rims. Others are more degraded. In the southeastern parts of this cluster, the small craters are so close together with such degraded rims that individual craters are

difficult to define. Instead, the terrain appears textured or hummocky, similar to braided terrains defined by other workers. In addition to its classic secondary morphologies, this cluster has a prominent radar CPR enhancement at 13-cm and a strong enhancement at 70-cm.

At NAC scales, the rims of some of these secondary craters have been breached by smooth material. A flow of smooth material breaches a flat-floored secondary crater just southeast of the northern-most, doubled-lobed secondary crater (Figure 3.27). Boulders of various sizes extrude from the otherwise smooth flow material. As in the other regions, it appears as though these boulders were incorporated into the flow as it moved along the surface (Figure 3.27). The smooth flow empties into the secondary crater, filling and flattening the floor. There also appears to be a smaller breach of the crater wall from the northwest.

Interestingly, the boulders and blocky material in these products are brighter than the surrounding smooth material. The smooth, dark material clearly superposes the bright, blocky material along the western contact, suggesting that the dark material is stratigraphically younger than the bright, block material that it superposes (Figure 3.27). This indicates that the dark albedo of the smooth material that breaches this crater wall may be the result of a compositional difference.

Smooth, dark material also covers the rim of the largest secondary crater in this cluster (Figure 3.28). This smooth material also superposes block-rich terrain from the east and from the north. Again, the smooth material is darker than the bright, blocky material, despite its younger age. The dark color of this deposit may reflect a difference in composition. In addition to its dark albedo, the western edge of the

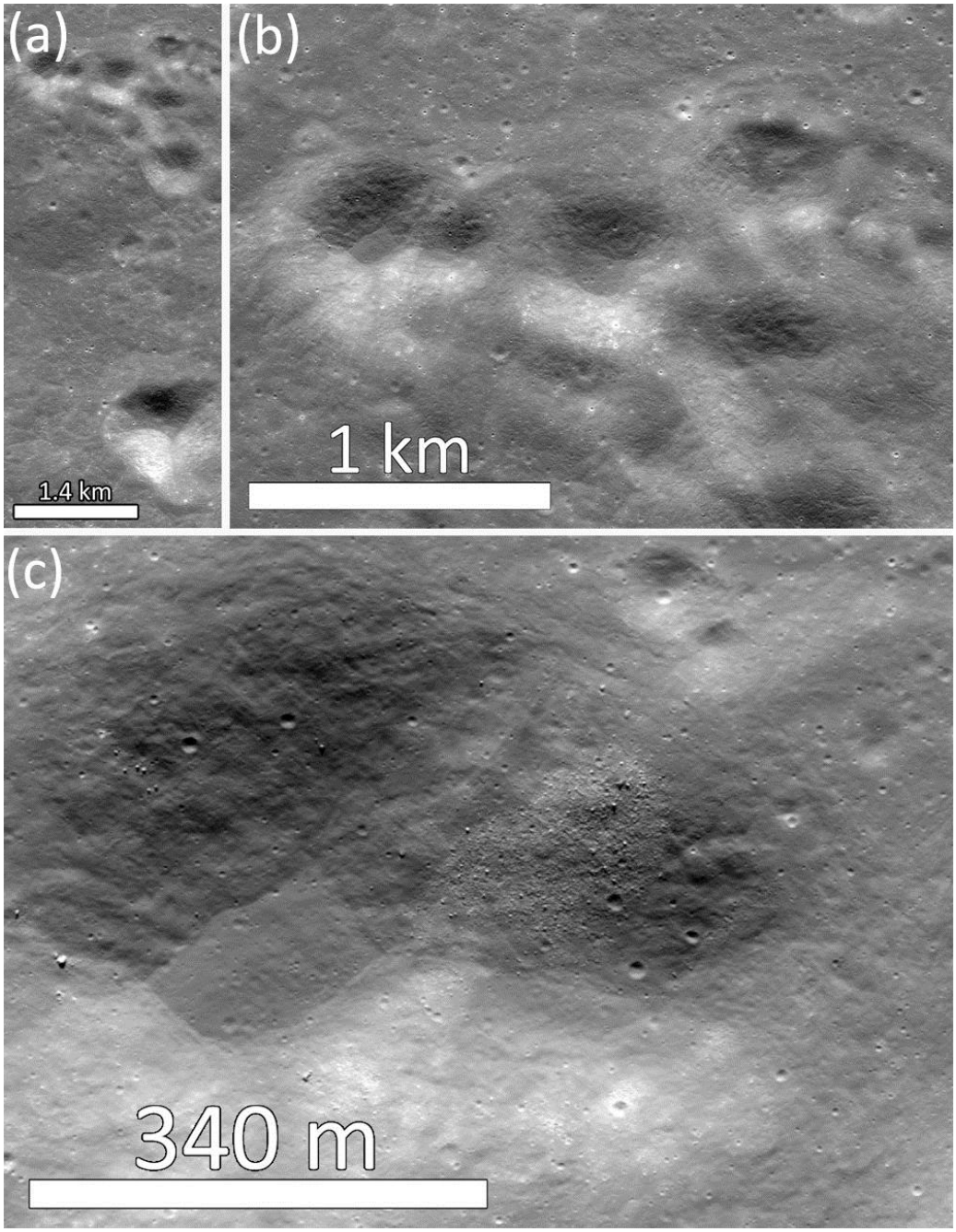

Figure 3.27. Lilius Region 1 (LROC NAC M109203644RC). (a) Context of the uprange part of the cluster. (b) Small secondary craters at the tip of the cluster with rounded rims and floors filled with smooth material. (c) Detail of one of these filled secondary craters. Smooth, dark material pools in the crater floor. This smooth material covers a small region of bright, block material on the eastern rim of this small crater.

contact between the smooth, dark material and the blocky flow has a clearly raised edge, possibly indicating a coherent flow front (Figure 3.28). Large blocks are also suspended on steep parts of the crater wall by the smooth, dark material. There are no indications, such as boulder tracks, to indicate that these boulders have rolled downslope since the smooth material was emplaced (Figure 3.28).

One possibility that could explain the low albedo and coherent morphologies of these particular flows is the incorporation of impact melt into the flow. As we saw at the primary craters in Primary Regions 1-4, when impact melt flowed back into the crater, it formed raised, lobate margins with a concentration of blocky material. The contacts between these smooth, dark flows and the blocky material at this secondary crater are reminiscent of those morphologies. But how reasonable is it in invoke a small melt component in these flows? Recently, workers have hypothesized that appreciable pockets of impact melt may be transported ballistically for large distances from the parent crater. *Robinson et al.* (2010) described young, smooth, ponded flows on the lunar nearside and hypothesized that these dark ponds could be impact melt from a large nearside Copernican-aged crater such as Tycho. These workers reported over 3,000 km^2 of these deposits, a significantly greater surface area than covered by the isolated regions of coherent flow morphologies that we observe at this Tycho secondary cluster [*Robinson et al.*, 2010]. Therefore, it does not seem unreasonable that a small volume of melt could have been ballistically transported to this region and incorporated into the debris flow. This might also account for the mapping of this region as "ash flow" by *Cummings* (1972).

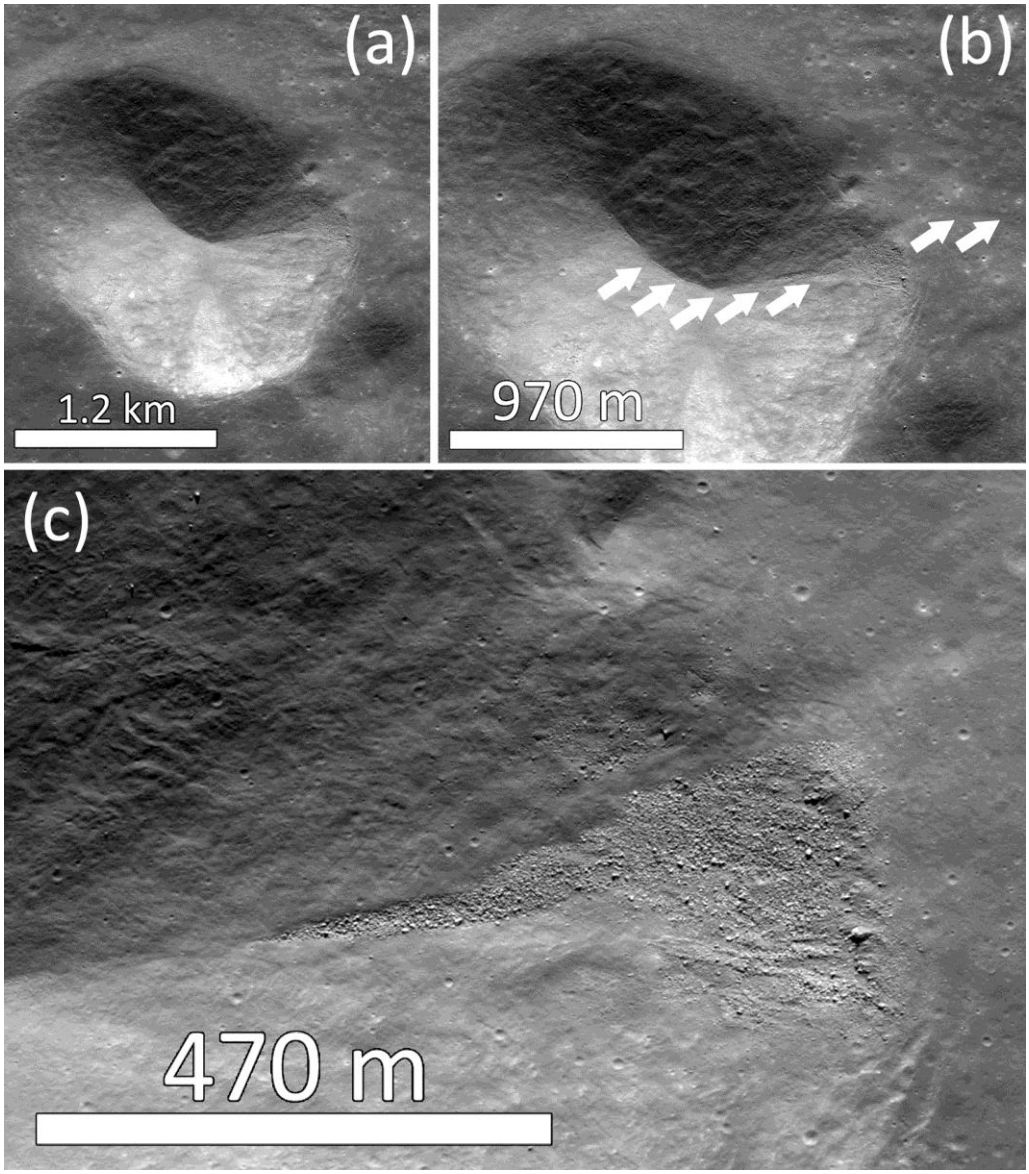

Figure 3.28. Lilius Region 1 (LROC NAC M109203644LC). (a) A large Tycho secondary crater near the tip of the Lilius Region 1 cluster. (b) Smooth, dark material breaches the rim of this secondary crater from uprange. White arrows highlight the sharp downrange margin of this smooth flow. (c) A contact between the smooth, dark material and bright, blocky material on the inside of the eastern rim. The dark material lies on top of the blocky material, as is visible at the raised margin of the smooth material on the western edge of the blocky terrain.

3.3.3.3.5.2 Lilius Region 2

Lilius Region 2 covers the floor of Lilius M crater and the two un-named craters directly to the north and south. The craters on the floor and northern wall of Lilius M are very dense but otherwise there are no morphologies visible on the WAC scale that would indicate that secondary craters are present in this location. Like Clavius Region 2, this region exhibits radar CPR enhancements at 13-and 70-cm despite the lack of obvious secondary crater morphologies on the WAC scale (Figure 3.19).

At the NAC scale however, these images reveal a crater cluster with classical secondary crater morphologies (Figure 3.29). These craters are strongly clustered, with the larger craters to the northwest and a gradation to smaller craters toward the southeast. In addition to being flat-floored, many of these craters exhibit prominent chevron-shaped dunes pointing in the direction of Tycho crater. A good example of this is the largest crater on the floor of Lilius M, which has well-developed chevron ridges (Figure 3.29). As we have seen many times at the other clusters, smooth material breaches the rim of this crater. Block rich material is confined to inside the herringbone ridge. Downrange from this crater, the terrain is disturbed for several kilometers in an excellent example of a braided morphology. Many of the smaller craters on the floor of Lilius M have uprange ridges reminiscent of deceleration dunes [*Morrison and Oberbeck*, 1975]. The small craters on the floor of the unnamed crater north of Lilius M also exhibit these uprange dunes.

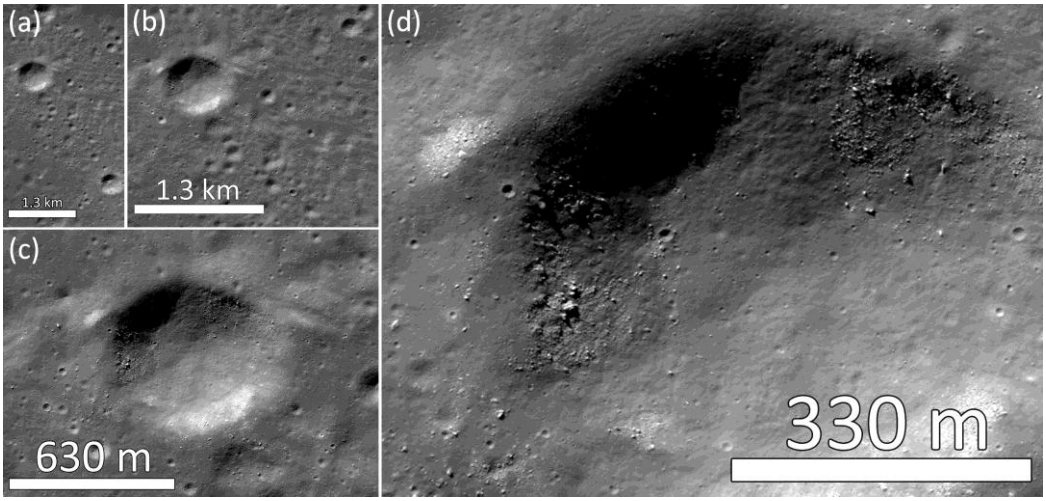

Figure 3.29. Lilius Region 2 (LROC NAC M122196145RC). (a) Context of an isolated secondary crater. (b) An otherwise circular Tycho secondary crater with a v-shaped uprange dune. Note the braided terrain to the east of the crater. (c) Detail of the v-shaped dune. (d) Blocky material inside the v-shaped dunes.

Therefore, much like we saw in Clavius Region 3, what appear to be isolated craters without secondary crater morphologies at the WAC scale, at higher resolution actually exhibit debris flow morphology associated with secondary cratering. These observations indicated that steaks of radar CPR enhancement, particularly at 13-cm, are a good tracer of this phenomenon.

3.3.3.3.5.3 Lilius Region 3

Lilius Region 3 crosses Lilius J crater and the flat plains to the north and south. This region exhibits CPR enhancements at 13-and 70-cm. At the WAC scale, a cluster of secondary craters, identifiable based on their sharp uprange rims with slightly v-shaped planforms, is visible just north of Lilius J crater. These craters are also strongly clustered compared to other craters of this size in the region.

At NAC scales, the rims of the craters in this secondary cluster appear very subdued. Several kilometer-sized craters on the floor of Lilius J display chevron dunes. Smooth material breaches the uprange rims of the craters in the downrange part of the cluster (Figure 3.30). Block rich material appears to have been transported downrange by this smooth material. The block rich material is confined to the area within the dunes, as if it were swept away elsewhere.

3.3.3.3.5.4 Lilius Region 4

Lilius Region 4 is located on the flat plains to the southwest of Deluc R crater. A chain of secondary craters can be seen at the WAC scale in this area (Figure 3.19). The direction of this cluster indicates that these are likely Tycho secondary craters.

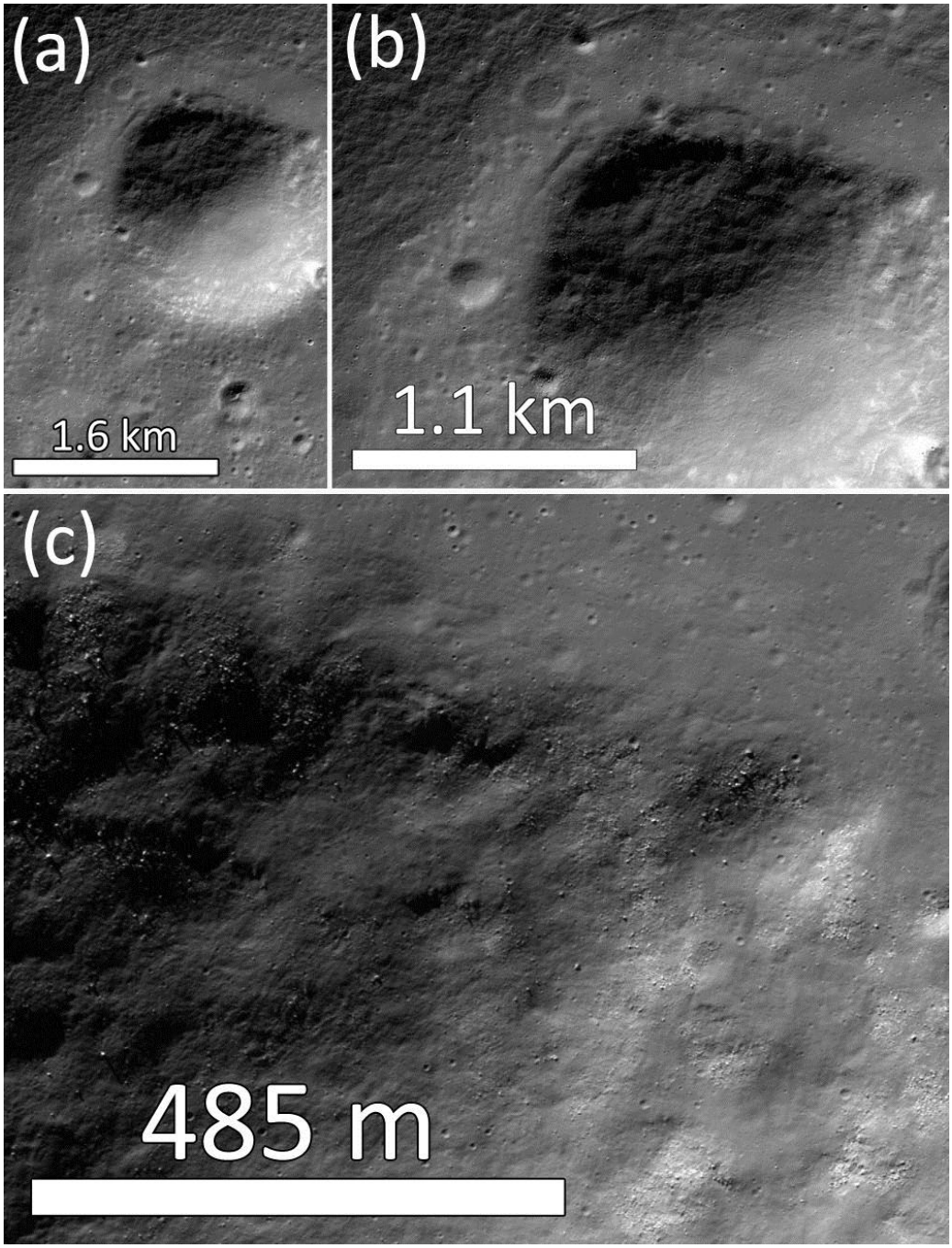

Figure 3.30. Lilius Region 3 (LROC NAC M122202930LC). (a) A large Tycho secondary crater with a circular planform and v-shaped uprange dune. (b) The smooth material of the uprange dune forms deceleration dunes where it slowed down flowing up the outer rim of the crater. (c) Contact between smooth and blocky material on the interior northeastern rim of this secondary crater

Radar CPR enhancement accompanies the clusters at 13-cm but is not discernibly above background levels at 70-cm.

At NAC scales, this area exhibits braided terrains and numerous flat-floored craters on the kilometer scale. The braided terrain is confined to the cluster and the region directly surrounding it, primarily concentrated in the downrange direction from Tycho crater. The flat-floored craters are filled with smooth material. As we have seen numerous times, blocky material on the 1-10 m-size scale is very rare in this cluster, despite the 13-cm radar CPR enhancement.

3.3.3.3.5.5 Lilius Region 5

The coverage of the NAC products in Lilius Region 5 crosses the same prominent cluster of Tycho secondary craters as the Lilius Region 1, albeit further downrange in the cluster (Figure 3.19). Like Lilius Region 1, this area displays strong radar CPR enhancements at both 13-and 70-cm. The secondary craters visible at the WAC scale are tightly clustered, shallow-floored, and elongated in the Tycho direction. Many of the craters in this cluster also have well-developed uprange v-shaped dunes.

This region shows some of the clearest examples of flow of smooth material around topographic obstacles. At NAC scales, the areas uprange of the v-shaped dunes show evidence of smooth material deflected around topographic highs (Figure 3.31). Not all of the smooth material is deflected, however. In some places, it breaches the rims of the secondary craters and creates smooth, hummocky deposits on the crater floors. As we have seen before, block-rich material is rare in this region.

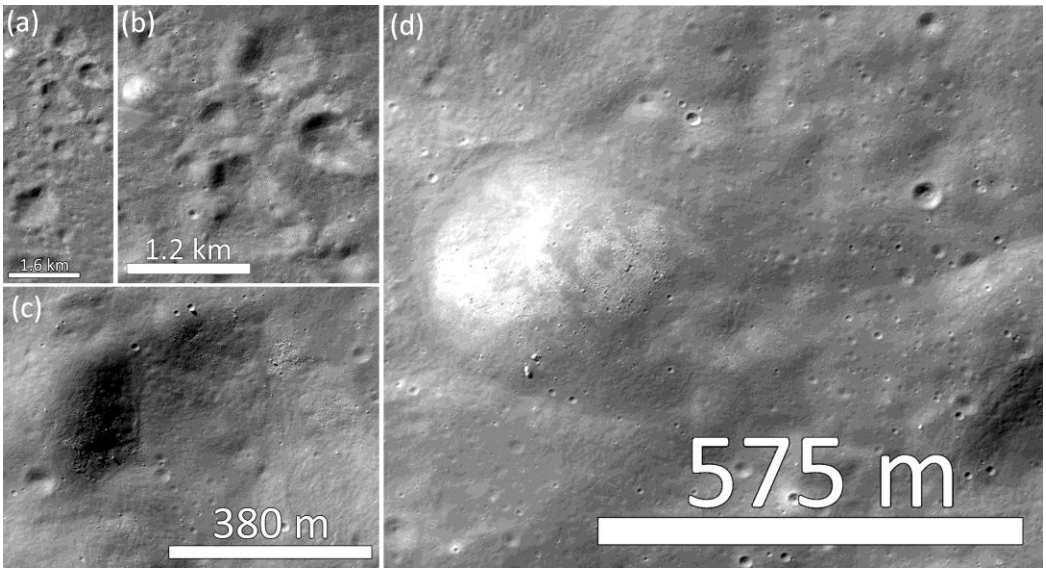

Figure 3.31. Lilius Region 5 (LROC NAC M137517296LC). (a) Cluster context. Note the scalloped planforms of the larger secondary craters. (b) Examples of v-shaped uprange dunes to the northwest of these Tycho secondary craters. (c) Contacts between smooth and blocky material on the interior of one of the secondary crater rims. (d) Smooth material appears to have flowed around this raised mound from the northwest to southeast, slipstreaming the edges of the mound.

Where blocky material is observed, it is typically on the interior of secondary crater rims and buried or partially covered by smooth material. As we have seen in a number of instances at other clusters, the blocky material in this region is brighter than the smooth material that covers it, indicating maturity is not responsible for the low albedo of these smooth flows.

3.3.3.3.6 Clavius and Lilius Region Summary

This investigation of the Clavius and Lilius regions, then, confirms that flow morphologies are common in and around Tycho secondary crater clusters, out to distances of approximately 500 km (11 crater radii) from the parent crater. The Lilius and Clavius regions exhibited examples of flows of smooth, dark material with raised margins draping over the rims of secondary craters toward the crater floors. The raised margins of these flows were often accompanied by an increase of block-rich material compared to the surrounding smooth terrain. The flow units consistently overlaid the bright, block-rich units, suggesting that the blocks are not eroding out of the margins, but may have been pushed along the surface by the flows to their current positions. This hypothesis is supported by the location of the highest concentrations of blocks, which commonly occur in areas which would have been shielded from flows moving downrange from Tycho, such as the leeward sides of crater rims. If the blocky material were being pushed or carried along by debris flows, we would expect them to be preferentially deposited in areas of low flow velocity, just as observed.

Another important point about these flow margins is that they are sharp, raised, and do not appear to have been disturbed by erosion or small impacts since they were

formed. Based on the work of *Robinson et al*. (2010), it is not unreasonable to assume that small amounts of primary impact melt may have been delivered to these regions and incorporated into the flows, resulting in coherent flow margins, resistant to erosion. In addition to the smooth, dark flows observed in secondary clusters at the Clavius and Lilius regions, braided terrains, uprange dunes, and other morphologies which suggest interference within these debris flows were also observed at isolated Tycho secondary craters otherwise lacking "secondary" morphologies on the WAC scale.

3.3.3.4 Newton Region

Wells et al. (2010) investigated Tycho secondary craters in the Newton and Newton-A regions near the lunar south pole. As discussed previously, they found Tycho secondary craters on the floor of these deep craters. These craters exhibited CPR enhancements at 13-cm and appeared otherwise to look like primary craters in WAC scale photographs. NAC global coverage allows us to look at this region in much greater detail. With this data, we can address the surface morphology of these regions to investigate whether or not the debris flow morphologies observed at the more tightly clustered craters in the other regions are also present at Newton and Newton-A. The Newton region lies approximately 25 Tycho radii from the parent crater. *Wells et al.* (2010) estimated an age of 3.8 Ga for this region based on corrected counts of primary craters. The floor of Newton-A, in particular, appears very heavily cratered.

Due to their latitude and depth, these craters are often subject to very low solar

incidence angles in the available NAC imagery. This provides an exaggerated view of the surface morphologies compared to what we observe at lower latitude regions like Tycho or Clavius.

3.3.3.4.1 Newton Regions 1-6

Newton Regions 1-6 cover the floor of Newton-A crater near the lunar south pole (Figure 3.3, Table 3.8). The craters on the floor of Newton-A display strong radar CPR enhancements at 13-cm, as documented by *Wells et al.* (2010). At WAC scales, these craters resemble small primary craters. They are not strongly clustered and have well-defined uprange and downrange rims.

At NAC scales, many of the small craters on the floor of Newton-A are filled with smooth material lacking blocky material on the 1-10 m-scale. Some of the craters also display clear uprange v-shaped dunes (Figure 3.32). In these cases, block rich material is also observed, typically downrange of the deceleration dunes where such debris would have been shielded from the smooth flows. At very low sun angles, braided lineations are also visible on the floor of Newton-A (Figure 3.32). Some secondary craters in the southern part of the floor of Newton itself are also accompanied by a downrange region of braided terrain.

The presence of morphologies at Newton-A that indicate clustering of primary ejecta, namely braided terrains and uprange dunes likely produced by debris flow along the surface, raises the interesting question: is primary ejecta similarly clustered at other sites so far-flung from the parent crater, or are the morphologies observed at Newton-A a special case?

Table 3.8. NAC product data for Newton Region

Product ID	Group	Resolution (m/pixel)	Center Latitude	Center Longitude
M137667011L	Newton 1	0.94	-79.45	340.42
M137667011R	Newton 1	0.94	-79.45	340.81
M137673796L	Newton 2	0.93	-79.61	339.33
M137673796R	Newton 2	0.93	-79.61	339.73
M155354486L	Newton 3	1.2	-80.74	340.64
M155354486R	Newton 3	1.2	-80.74	341.21
M155361271L	Newton 4	1.2	-80.71	339.66
M155361271R	Newton 4	1.2	-80.71	340.23
M155368056L	Newton 5	1.2	-80.73	338.65
M155368056R	Newton 5	1.2	-81.82	339.46
M157721971L	Newton 6	1.2	-80.71	339.72
M157721971R	Newton 6	1.2	-80.71	339.15

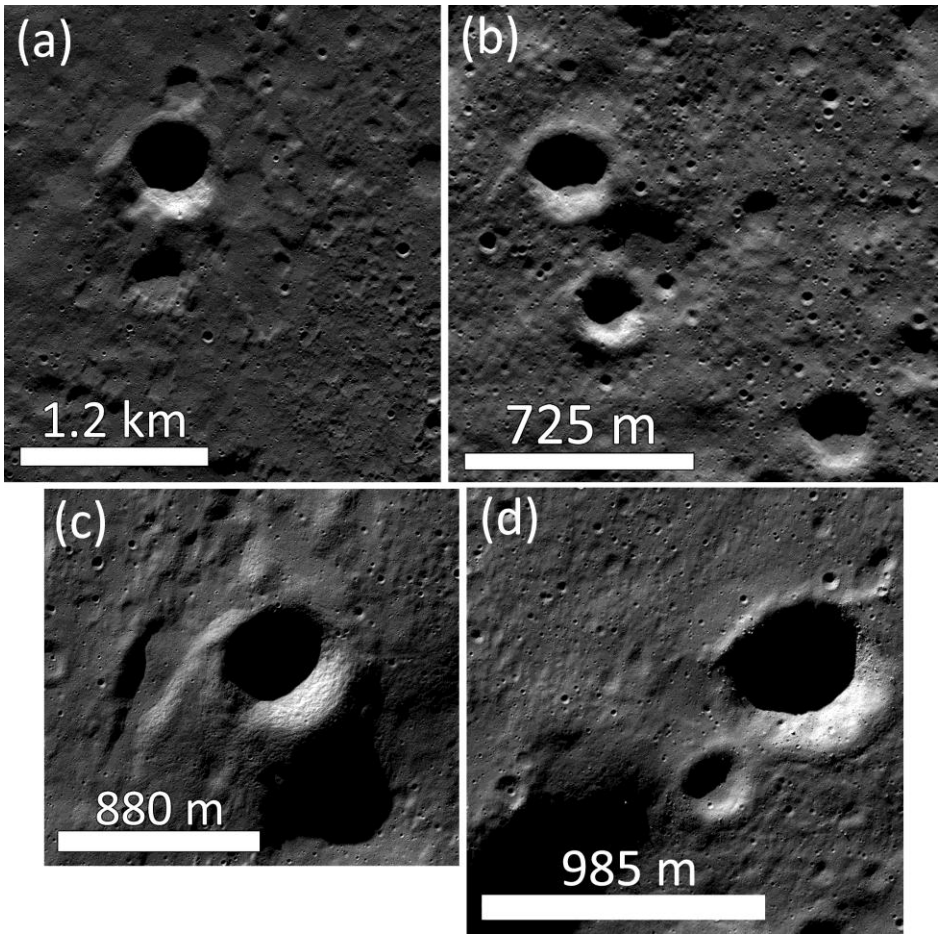

Figure 3.32. Newton Region. Examples of v-shaped dunes and braided terrains. (a) LROC NAC M155368056LC. (b) LROC NAC M155354486LC. (c) LROC NAC M137673796LC. (d) LROC NAC M137667011LC.

In order to address this question, I looked at NAC photographs of the Tycho secondary crater clusters near the Apollo 17/Taurus Littrow Valley site. The Apollo 17 landing site is even further from Tycho crater than the Newton region, at a distance of 2250 km (Figure 3.2). The secondary craters near the landing site were discussed in detail by *Lucchitta* (1976). In the following section, I examine the NAC morphologies at these craters as well as the CPR signature at 13-cm and compare them with the Newton observations.

3.3.3.4.2 Apollo 17 Regions A-G

Apollo 17 Regions A-G cover the light mantle region to the west of the Apollo 17 landing site. This area was covered in the westernmost part of the Apollo 17 ground traverse. Like the smooth, dark regions we have seen at clusters closer to Tycho, the light mantle here is lacking clasts on the 1-10 m scale. Subdued braiding can be seen at the southernmost extent of the smooth mantle. This braiding continues past the albedo feature downrange from the Tycho direction (Figure 3.33, Table 3.9).

The landing site and surrounding crater cluster are also included in this region. The Tycho secondary crater cluster south of the landing site is composed of shallow craters with scalloped planforms, as seen on the NAC scale at the other regions of interest. Scalloped planforms are instances where smooth material interrupts the crater rim in numerous places, creating a scalloped outline when viewed in planform. Smooth material breaches the rims of these craters from the Tycho direction (Figure 3.33). Many of the secondary craters in this cluster have well-developed uprange dunes, as if the smooth material were deflected around their rims to form v-shaped

Table 3.9. NAC product data for Apollo 17 Region

Product ID	Group	Resolution (m/pixel)	Center Latitude	Center Longitude
M106690695L	Apollo 17 A	1.5	20.18	30.5
M106690695R	Apollo 17 A	1.6	20.18	30.78
M104318871L	Apollo 17 B	1.4	19.97	30.55
M104318871R	Apollo 17 B	1.4	19.97	30.78
M113758461L	Apollo 17 C	0.52	19.78	30.84
M113758461R	Apollo 17 C	0.51	19.78	30.76
M116113215L	Apollo 17 D	0.50	20.44	30.85
M116113215R	Apollo 17 D	0.50	20.44	30.78
M129086118L	Apollo 17 E	0.49	20.2	30.8
M129086118R	Apollo 17 E	0.49	20.2	30.73
M159752868L	Apollo 17 F	0.50	20	30.64
M159752868R	Apollo 17 F	0.50	19.99	30.56
M162107606L	Apollo 17 G	0.48	20.21	30.75
M162107606R	Apollo 17 G	0.48	20.2	30.68

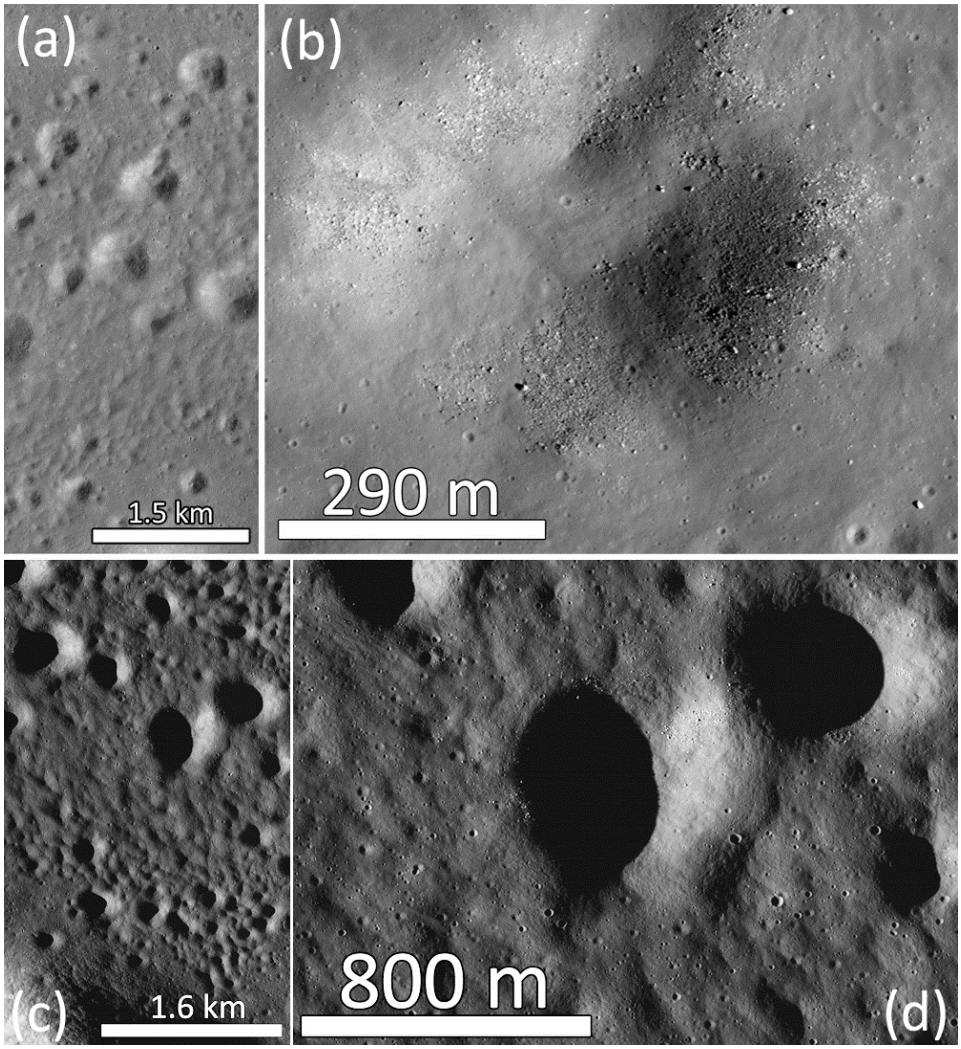

Figure 3.33. Apollo 17 Region. (a) Braided terrains and scalloped crater planforms in the cluster of Tycho secondary craters near the Apollo 17 landing site (LROC NAC M113758461RC). (b) Smooth material breaches the rim of this small secondary crater (LROC NAC M113758461RC). (c) Another example of braided terrain (LROC NAC M116113215RC). (d) Braided terrain and blocky material on the interior rims of small Tycho secondary craters (LROC NAC M116113215RC).

ridges. Bright, blocky material is found primarily on the interior walls of these craters. Although the blocky material is overlain by the smooth material, the blocky material is consistently lighter than the smooth material. The relationship between these smooth flows and isolated areas of blocky material are also consistent with what we have seen at other clusters. Braided terrains are also visible in the southwestern part of this cluster (Figure 3.33). These braided terrains were first identified by *Lucchitta* (1976). The braided terrains in the southern part of the cluster grade into the smooth material that is deflected to form the v-shaped dunes uprange of the crater rims.

Based on these observations of the secondary craters at the Apollo 17 landing site, we conclude that extreme distance from the parent crater does not prohibit the formation of debris flow by clustered primary ejecta. Other workers have noted that spreading of fragments during the long flight times to distal sites reduces the clustering of secondary craters [*Bierhaus et al.*, 2005]. At Newton-A, the secondary craters themselves, which are widely spaced, support this claim. However, the presence of the debris flow morphologies at Newton and Apollo 17 indicate that, while secondary-forming fragments may be more diffusely scattered at these large distances, the density of smaller fragments is sufficient to produce debris flows with interference patterns like uprange dunes and braided lineations. The same holds true for isolated secondary craters observed closer to Tycho in the Clavius and Lilius regions. Although these features are only apparent in photographic images when viewed at high resolution, such as provided by the LROC NAC, radar CPR enhancements can be used to identify candidate secondary craters at lower resolution.

3.4 Analysis

The morphologies observed at the five regions within Tycho crater's rays can be divided into four general classes: (1) Impact craters, (2) Braided/disturbed terrains, (3) Smooth terrains, and (4) Block-rich deposits. In the following section, we will summarize the properties of these groups.

3.4.1 Impact Craters

The impact craters observed in these clusters displayed a variety of morphologies, with the most notable difference occurring across size regimes. Note that these size regimes do not reflect sharp boundaries, but rather qualitative trends in morphology with size.

3.4.1.1 Size: 0.5-1.4 km

At LROC WAC resolutions, craters in this size-range fit the traditional description of secondary craters. They are strongly clustered compared to craters of the same size outside of the regions of elevated radar CPR. We interpret these craters as Tycho secondaries.

The uprange rims of these craters tended to be better preserved than the downrange rims. Fine, smooth material (lacking clasts on the 1-10 m scale) has been deposited in these craters. The extent of filling due to this material varies. The largest craters in this size range tend to have better-preserved rims, breached only locally by lobes of the smooth material. These craters have relatively minimal infilling, but still

display flat floors and reduced crater depth. Craters on the small end of this size range have been almost completely filled by the smooth material. Only traces of their rims remain visible. As with the larger craters, the uprange rims are better preserved than the downrange rims.

3.4.1.2 Size: 80 m to 0.5 km

There is a noticeable lack of craters on the 80-400 m size-scales in these regions. Within this size-range, "subdued" craters are most common. Below about 80 m in diameter, the number of craters increases again dramatically and is combined with a transition to predominantly "sharp" crater morphology.

Subdued craters are circular depressions lacking raised rims. These craters display very shallow depth compared to diameter. However, they show little evidence of mass wasting, i.e. blocks or slumped material, to indicate that they have degraded to this state slowly over time. Morphological evidence suggests that the subdued craters formed very rapidly after the formation of the secondary craters and the deposition of the smooth units. It is difficult to explain these features as independent primary craters due to the large number that appear to have formed almost simultaneously. The subdued craters could be remnants of pre-existing craters, partially obliterated by the secondary cratering processes. However, subdued craters emplace secondary craters and other secondary features, so this cannot explain all instances of the subdued morphology. It is more likely that these features are the result of self-secondary or tertiary cratering.

3.4.1.3 Size: 5 m to 80 m

In contrast to the subdued craters, "sharp" craters display sharp, well-preserved rims. Their interior walls are steeper than the walls of the subdued craters. Meter-sized blocks are also frequently observed in association with the sharp craters. The sharp craters overlay the subdued craters. There is also a sub-class of sharp craters with central pits. These "pit craters" share the morphological characteristics of sharp craters, but are also distinguished by the presence of small central pits. As already discussed, these pit craters are the result of a change in target strength with excavation depth.

Based on their morphology, we interpret the sharp craters as fresh primary craters formed since the emplacement of the smooth units. At most diameters on the Moon, primary craters follow a b=-2.0 power-law slope in their size-frequency distributions (SFDs). At b=-3.72 and b=-3.26, the SFDs of the sharp craters observed at Lilius Region 1 and Clavius Region 1 are steeper than expected for typical primary craters (Figure 3.34). However, other evidence for a steep-sloped small-diameter primary crater population has been reported, in particular on the asteroid Gaspra, where local gravity is not strong enough for secondary cratering [*McEwen et al.*, 2005].

3.4.2 Braided Terrains

Numerous examples of braided terrains were observed in our regions of interest. These braided terrains displayed classic morphologies, including v-shaped ridges and

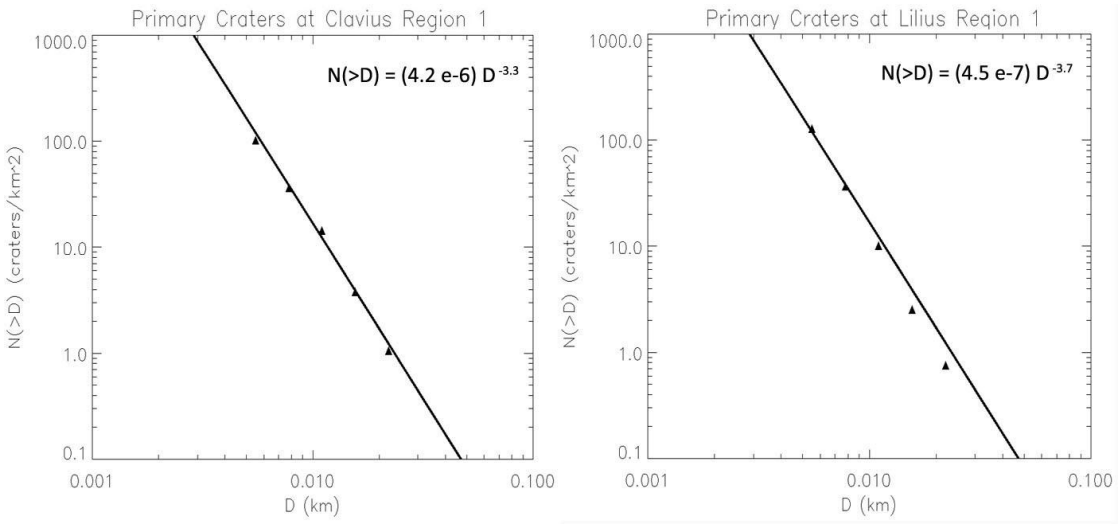

Figure 3.34. Crater SFDs of small craters at Lilius Region 1 and Clavius Region 2.

circular depressions ranging from gouges to fully developed craters. The further downrange in the cluster, the more degraded the craters, until they become more of wedge-shaped gouges than true impact craters. Unlike the impact craters, the gouges appear never to have had fully-formed downrange rims. In some places, the gouges themselves become subdued, giving way to ridges alone. Narrow lineations a few meters across but tens to hundreds of kilometers long were also observed at many of these clusters. Another class of features related to braided terrains was deflection dunes. We attribute the chevron-shaped deposits of smooth material, observed uprange from topographic obstacles, such as raised crater rims, to the deceleration of rapid debris flows as they travelled uphill.

Like other workers before me, I interpret the disturbed terrains as deposits due to interference of secondary crater ejecta and local material reworked by secondary processes. Dunes at high angles to the radial direction are the result of interference between secondary ejecta moving downrange and encountering ejecta from later-forming craters [*Morrison and Oberbeck*, 1976]. Dunes at low angles to the radial direction are the result of interfering ejecta from widely spaced secondary craters at similar radial distances from the parent crater [*Morrison and Oberbeck*, 1976]. Some of the high-angle dunes also appear to have been augmented by material flowing over the surface. This material is deflected by the dunes, forming raised ridges and filling in areas of low topography. As in the case of *Morrison and Oberbeck* (1975), this flow obliterates shallow secondary craters and gouges while augmenting ridges, giving rise to the prominent braided morphologies observed downrange from the full-developed secondary craters. This also occurs at isolated craters, indicating that ejecta

too small to form secondary craters may be significantly clustered even when larger, crater-forming ejecta is well-dispersed.

3.4.3 Smooth Terrain

The smooth terrains are observed in the intracrater regions of these clusters. As an example, consider the intracrater regions at Clavius 1. At WAC resolution, this area displays several examples of concentric ridges and braided terrains. At NAC resolution, the surface around these ridges and between the secondary craters appears very smooth despite the high radar CPR values of this region at both 13-and 70-cm. Where blocks on the 1-10 m size-scale are observed, they are partially buried by the smooth material.

Aside from the dearth of blocky material, these smooth terrains exhibit other interesting properties, namely, evidence of flow. The smooth units make up concentric ridges and braided terrains, morphologies that other workers have interpreted as debris flow deposits [*Morrison and Oberbeck*, 1975; *Lucchitta*, 1975]. The smooth terrains breach secondary crater rims. Figure 3.21 shows an example from Clavius Region 1. In this instance, smooth material breaches a secondary crater rim in two separate places, both of them on the downrange rim. The two smooth units begin outside of the crater and appear to cut channels in pre-existing rim and flow down the interior wall into the crater floor. The channels of smooth material are narrow where they breach the crater rim and broaden out in a fan-shape. Few 1-10 m-sized blocks are present in the smooth units that breach this secondary crater rim. The blocks in this particular area are partially covered in smooth material. None of them

appear to sit on top of the smooth material, as one might expect if the blocky material were simply eroding out of the smooth material.

The smooth materials do not always breach the crater rims. In some cases, they drape over the crater rim to create hummocky deposits on the crater floors. The degree of infilling due to these smooth units varies. In some craters, the smooth material only covers the interior crater walls, though it clearly originates outside of the crater and is not a case of simple mass-wasting along the rim. This is in contrast to what we saw at the primary craters of a similar size, where the material slumping down the interior walls appeared to originate within the crater. In other instances, the infilling due to the smooth material is more extensive, leaving only partial crater rims, usually on the uprange side of the filled craters. Other craters have been completely filled, leaving only slightly raised areas at the rims.

The margins of these smooth terrains vary in height. In some places, they are raised and well-defined. In others, they grade evenly into the surrounding terrain without clear unit boundaries, making it difficult to map margins within the smooth terrains. An example of a sharp, raised margin can be seen at the largest secondary crater in Lilius Region 1. In this instance, the smooth terrain begins outside of the crater and drapes over the crater rim from the northwest. It covers the north interior wall of the crater and reaches to the crater floor. The raised southern margin extends from the crater interior, over the crater rim, and into the intercrater region to the east. On the crater wall interior, a crater a few meters in diameter has formed a near the raised margin, but has not disturbed it. One would expect that a deposit of unconsolidated material would have collapsed along the margin during the formation

of this crater. However, the fact that the margin appears undisturbed suggests that the smooth material may be a consolidated deposit. This is not the only instance in these regions of interest where the smooth material shows signs of being cohesive. There are other examples of small craters forming near margins without disturbing them. In some cases, boulders are perched on steep slopes with no indication that they have moved since the smooth units were deposited. The fact that these smooth terrains appear to anchor these blocks in place also suggests their cohesive nature. The morphology of the subdued craters could also be explained by impact into a cohesive material that has not yet "set." In a cohesive target material with low strength, subdued rims and crater floors would be expected due to rapid relaxation of the target after impact. Recent work by *Robinson et al.* (2010) reported over 3,000 km^2 of potential impact melt deposits near the Tycho antipode which they speculated may be related to a near side Copernican-aged crater. Considering the volume of this melt and the distances it would have been required to travel, it does not seem unreasonable that a small volume of melt could have been ballistically transported to the regions of interest studied in this work. If melt were incorporated into the debris flows, that could explain the subdued morphologies observed at these crater sizes.

3.4.3.1 Flow Depth

As discussed previously, the presence of fresh-looking craters with small central pits are indicative of layering in the smooth terrains [*Melosh*, 1989]. The fine material of the smooth terrain appears to overlay a blockier substrate which is excavated by these small, fresh craters. We have used the size of these pit craters to

determine the depth of the smooth terrains. According to *Melosh* (1989), the depth excavated by a crater is approximately equal to $1/10^{th}$ of the transient crater diameter:

$$d_{exc} \sim 1/10\ D_{crater} \quad \textbf{(4.1)}$$

Therefore, the smallest pit crater observed in a given region is a measure of the maximum layer thickness in that region. The largest crater in a region without a central pit sets a bound on the minimum depth of the smooth layer. Using this method, we mapped the minimum and maximum smooth layer thickness at clusters 1-3 (Figure 3.35). Typical flow depths were measured on the order of 1.5-3.0 meters. No correlation was observed between thick or shallow flow depths and small variations of the CPR value within the areas of CPR enhancement. Due to the nature of the measurement, however, this inconclusive result is unsurprising. The smooth flows themselves are of limited spatial extent and flow depths were typically determined using one or two craters per cell. Therefore, the depth probed by this small number of craters may not accurately reflect the maximum depth of the flow in these regions. Alternatively, expanding the size of the "cells" in which the flow depth is measured would not necessarily improve the accuracy of the measurement, because this would not account for potential variation of flow depth with location.

3.4.3.2 Flow Age

Finally, the small primary craters emplaced on two of the smooth flows were counted to get a measure of the age. Craters with 5 m < D < 60 m were counted, divided into bins of width (2^1/2). Only "sharp" craters were included in these counts. Due to their unusual morphology, I was concerned that "subdued" craters

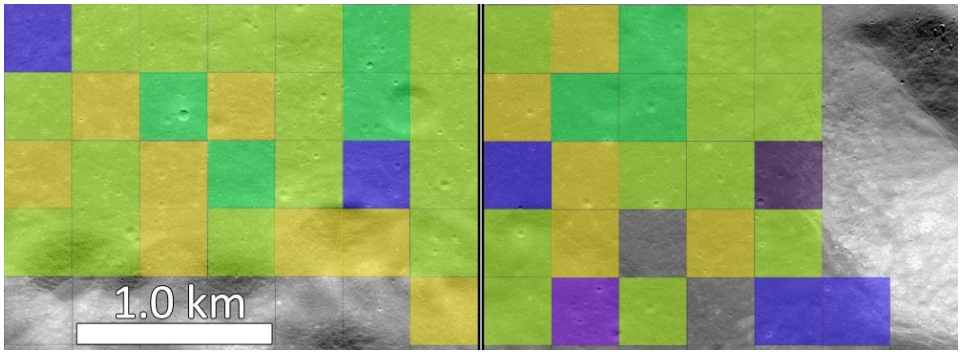

Figure 3.35. Estimated flow depths at Lilius Region1. Yellow = 0.55 m, Yellow-Green = 0.78 m, Green = 1.1 m, Blue = 1.5 m, Light Purple = 2.2 m, Dark Purple = 3.1 m.

might not represent a primary crater population, but rather self-secondary or tertiary cratering. Therefore, they were excluded from the counts. Due to the limited spatial extent and young age of the smooth terrains, it was difficult to achieve sufficiently populated bins at the large diameter end, even only extending them as far as 60 m in size. In order to minimize bias due to imbalances in the number of small and large craters, we also adopted an equal-number counting approach. In this approach, craters in each size bin were counted separately. The counting area of each bin was expanded until it included 30 craters. This way, each bin in the differential SFD was equally weighted. Cumulative SFDs were also compiled and fit to N(1) values from *Neukum et al.* (2001)'s isochrons to estimate age. The size-frequency distributions for Lilius Region 1 and Clavius Region 1 are presented in Figure 3.34. The N(1) values of the smooth terrains are 4.5×10^{-7} and 4.2×10^{-6}, equivalent to ages of <1 Ma and 5 Ma, respectively. These values are considerably younger than the age of Tycho crater (between 96.5 and 107 Myr [*Arvidson et al.*, 1976]). However, I don't mean to suggest by quoting these densities that these flows were actually emplaced in the last few Ma. Due to the steep slopes of these SFDs, extrapolation of counts at these very small diameters to an N(1)-type age does not necessarily accurately reflect the true ages of these smooth units. This is due to the fact that small changes in the best-fit SFD slope at diameters of 10-100 m extrapolate to very different N(1) values, which are a reflection of the cumulative density above 1 km. Therefore, a lack of craters in the largest size bin compared to smaller bins—whether an artifact or a reflection of the true distribution—dramatically reduces the best-fit N(1) value, and thus the age. A

difference in crater retention properties in the smooth terrain could also explain the dearth of observed craters.

3.4.4 Block-rich Terrains

The last morphology group observed was the "block-rich terrain," or BRT. We define BRTs as concentrations of blocky material on the 1-10 m-scale, in contrast to the smooth terrains, which lack blocks of this size. Instances of block-rich terrain were common along the margins of smooth terrains. These contacts often occurred on the interior walls of secondary craters. Lilius Region 1 exhibits a block-rich terrain on the eastern interior wall of a 2-km diameter Tycho secondary crater. This BRT begins at the rim of the secondary crater and extends down the wall to the crater floor. Larger blocks are more common near the rim, with small blocks primarily near the crater floor. The BRT is partially buried from the northwest by one of the smooth terrains described in the previous section. Individual boulders in the BRT are partially buried by or extrude from the smooth terrain. Partially buried blocks are consistently draped with smooth material on the northwest side and bare to the southeast. This is consistent with deposition of the smooth terrain from the northwest, the direction to Tycho crater. We interpret this BRT as a mass-wasting event that took place very shortly after the formation of the secondary crater and subsequently covered by the smooth terrain.

There are other type-examples of BRTs in Lilius Region 1. Unlike the previous example, the contacts between the smooth terrain and these BRTs are not sharp. Instead, the smooth material drapes over individual blocks and grades

gradually toward the crater floors. As before, the smooth terrains consistently drape the blocks from the uprange direction. I stress that these blocks do not appear to be eroding out of the smooth terrain. If they were eroding out of the smooth material, we would expect to see blocks on top of the smooth material on these crater floors. With one or two exceptions, this is superposition relationship is not observed.

3.5 Interpretation

I interpret the smooth terrains as reworked material transported downrange by secondary- crater-initiated debris flow. In keeping with *Morrison and Oberbeck* (1975)'s debris surge hypothesis, I propose that primary ejecta from Tycho crater interacted with the surface, creating a fast-moving surge of material traveling downrange just behind the Tycho ejecta curtain (Figure 3.36). In the first step of the debris flow process, fragments are ejected from the primary crater at a variety of velocities, from low-velocity fragments, which land near the crater, to higher velocity fragments, which will impact at large distances from the crater. These distal ejecta fragments have high internal tension (*Melosh*, 1989), and break into smaller fragments during flight. Because of the long travel times, and the small velocities of these fragments relative to one another after breakup, these fragments are less clustered at impact than ejecta fragments at lower ejection velocities. These loosely clustered fragments impact at slightly different radial distances and slightly different times. Large, secondary-crater-forming fragments and smaller fragments (which may not form craters) are distributed at random along the radial direction in these clusters. Let's consider a cluster in which small fragments impact first, followed by a large

Figure 3.36. A cartoon outlining the initiation of debris flow by primary ejecta fragments. (a) The first ejecta fragment in a given secondary cluster impacts the surface. Downrange momentum from the fragment is transferred to loose material on the surface, causing it to flow downrange. (b-d) Additional primary fragments impact the surface and initiate downrange flow of loose surface material. The debris flow is slower-moving than the primary ejecta curtain, so secondary craters form downrange before they are reached by the flows originating uprange. (e-f) Debris flow moves downrange through the cluster of newly-formed secondary craters. The flow is deflected by topographic highs, carrying block-rich secondary ejecta downrange as it travels. Small secondary craters are eroded by the flow. Interference of material within the flow (i.e. from different points of origin) contributes to the braided and lineated features observed at many Tycho secondary craters studied in this work.

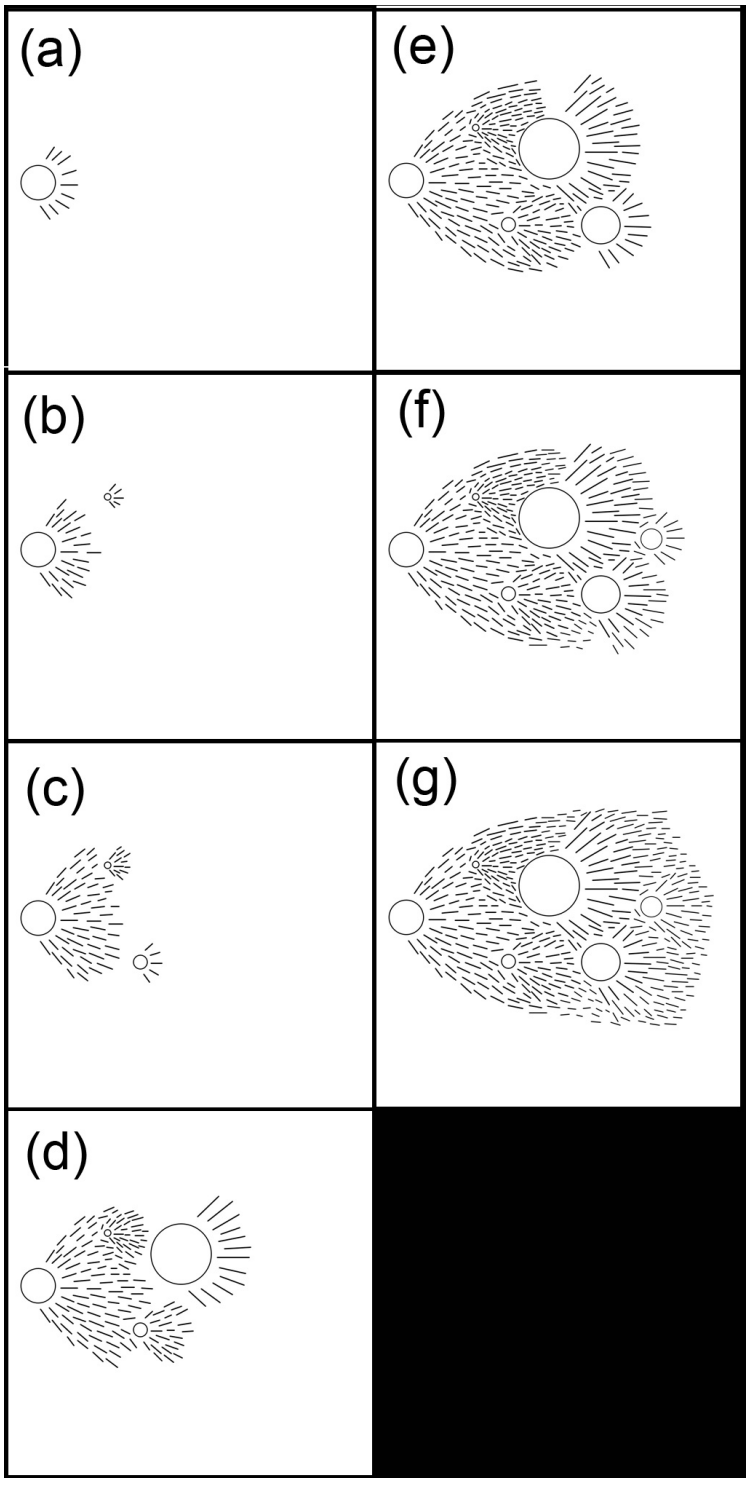
(a)
(e)
(b)
(f)
(c)
(g)
(d)

fragment which forms an isolated secondary crater. Following the hypothesis of *Oberbeck* (1975), I hypothesize that when the small fragments impact the surface, they transfer downrange momentum to loose material on the local surface. This transfer of momentum initiates debris flow in the downrange direction. The velocity of this flow is almost certainly less than that of the expanding ejecta curtain [*Melosh*, 1989], so downrange features, such as the isolated secondary crater in this example, will form before the debris flow reaches them. Where the debris flow encounters secondary crater rims, there are two possible outcomes. The debris can flow over the rim, or it can be diverted around it. In the first case, the result are the smooth, dark deposits that we see "draping" over the rims of secondary craters and burying or partially burying the block-rich terrains. When the debris is diverted around the crater rims, it contributes to the v-shaped dunes, braiding, and lineations observed at these clusters—patterns similar to those observed when water is diverted around a cluster of rocks in a rapids. I emphasize that this is not a continuous process extending from the parent crater out to these clusters, but rather isolated flows associated with secondary craters or crater clusters.

When the secondary craters form, they eject both fine and blocky material. This material is subsequently entrained by the debris flow and transported in the downrange direction, explaining the downrange asymmetry of the elevated radar CPR features in these regions. This interpretation also explains the existence of the small pitted craters and the location of the block-rich terrains. The flows swept bock-rich material downrange, depositing it in regions of low flow velocity, such as topographic high points and the leeward sides of obstacles to the flow. These regions are

consistent with the areas in which BRTs were most frequently observed. The existence of blocks extruding from the flow suggests that the smooth terrains are a thin layer covering a block-rich substrate of material excavated by the secondary craters. The small-pitted craters also support this interpretation. This buried layer of block-rich material probably contributes to the radar CPR enhancements at 13-and 70-cm. At NAC resolution, it is unclear whether the 13-cm scatterers are located primarily on the surface or if they are buried by the smooth material. Whether buried or on the surface, transportation of radar scatterers downrange by debris flow explains the source and orientation of the radar CPR enhancement observed at Tycho secondary crater clusters. These observations revealed evidence of these debris flow not only in areas of clustered secondary craters, but also at relatively isolated craters revealed to be secondaries by the presence of the signature radar CPR enhancement.

3.5.1 Comparison to Other Work

The assertion that debris surge is an important part of lunar secondary cratering not only at clusters of secondaries but also at relatively isolated secondary craters has important implications for secondary crater identification. If isolated secondary craters typically exhibit debris flow morphologies at the 10-100 m scale, then these features can serve as an identification tool for differentiating between this elusive class of secondary events and kilometer-sized primary craters. The Tycho secondary craters that we observed indicated that debris flow occurs at clustered and isolated secondary craters out to distances of 50 crater radii from the parent. Does this hold true in general, or is there some bias in the selected regions that make debris flow appear

more common than it really is? In order to address this question, we selected several regions of Copernicus and Tycho secondary craters studied by other workers to see if debris flow morphology were visible in these areas on the NAC scale. These regions are LC Copernicus 1-2, LC Ptolemaeus 1-3, and LC Zollner. These regions were initially investigated by *Lucchitta* (1976).

3.5.1.1 LC Copernicus Region 1

LC Copernicus Region 1 covers a region of isolated Copernicus secondary clusters in the south-central portion of the Imbrium basin (Figure 3.3, Table 3.10). The areas that correspond to the secondary clusters have radar CPR enhancements at 13-cm. At the WAC scale, the Copernicus secondary craters can be identified by their linear clustering radially away from Copernicus. As we have seen at the Tycho clusters, the craters in these clusters are characterized by sharp uprange rims and heavily degraded or non-existent downrange rims. They have well-developed herringbone dunes and the terrain downrange from these clusters is disturbed for several kilometers by braided lineations pointed in the Copernicus direction.

As we observed in other debris flow regions with elevated radar CPR, the braided terrains appear very smooth on the NAC scale. Again, blocky material is very common on the rims and interior walls of the secondary craters, particularly near the front of the cluster. It is less common downrange, grading into the smooth braided areas. Where block rich material is prevalent, it is confined to inside of the herringbone ridges. These are the same locations where BRTs were common in the Tycho secondary clusters.

Table 3.10. NAC product data for *Lucchitta* (1976) Comparison Regions

Product ID	Group	Resolution (m/pixel)	Center Latitude	Center Longitude
M116472761L	LC Copernicus 1	0.96	24.18	335.84
M116472761R	LC Copernicus 1	0.96	24.17	335.76
M116574450L	LC Copernicus 2	0.99	28.47	320.53
M116574450R	LC Copernicus 2	0.98	28.46	320.45
M106870568L	LC Ptolemaeus 1	1.1	-9.37	1.01
M106870568R	LC Ptolemaeus 1	1.1	-9.36	1.18
M113948971L	LC Ptolemaeus 2	0.51	-9.32	1.03
M113948971R	LC Ptolemaeus 2	0.51	-9.32	0.96
M122203814L	LC Ptolemaeus 3	0.49	-9.21	1.09
M122203814R	LC Ptolemaeus 3	0.49	-9.21	1.16
M122088464L	LC Zollner	0.90	-7.41	18.59
M122088464R	LC Zollner	0.90	-7.4	18.66

3.5.1.2 LC Copernicus Region 2

LC Copernicus Region 2 also covers an isolated Copernicus secondary cluster in the Imbrium basin several hundred kilometers northeast of Aristarchus crater (Figure 3.3). This cluster has a radar CPR enhancement at 13-cm. The Copernicus secondary crater cluster is obvious at WAC scales. The craters in this cluster are tightly grouped, trending from large craters to small craters from southeast to northwest. The largest craters in this cluster have well-defined up-and downrange rims, with instances of well-developed herringbone ridges. The center of this cluster is characterized by braided terrain. The braided terrain is very smooth, but blocky material is common on the rims of the craters in the cluster, typically confined to within the v-shaped dunes, where we would expect to find them if they had been transported downrange by debris flow.

This region is also crossed by a cluster of Aristarchus secondary craters, trending from southwest to northeast. These clusters are also characterized by smooth braided terrains with blocky material confined inside of the dunes on the interiors and rims of the craters themselves. In some instances, the locations of this blocky material have clearly been slipstreamed by smooth material.

3.5.1.3 LC Ptolemaeus Regions 1-3

LC Ptolemaeus Regions 1-3 cover a section of the eastern rim on Ptolemaeus crater (Figure 3.3). Two clusters of what appear to be Tycho secondary craters (based on their orientation) are visible at the southern and central portions of these products.

At the WAC scale, the craters in these clusters generally grade from largest to smallest progressing uprange to downrange. These craters typically have sharp uprange rims and heavily degraded or nonexistent downrange rims. Herringbone dunes are very well-developed in these clusters, grading into braided terrains as described by *Lucchitta* (1976).

At the NAC scale, these clusters are characterized by very smooth terrain. Smooth, hummocky deposits fill the floors of the craters. Small, fresh craters appear to excavate blockier material. Deceleration dunes have also formed around what appear to be pre-existing craters in LC Ptolemaeus Region 2, which indicates ground flow rather than ejecta blanket interference as a deposition mechanism.

3.5.1.4 LC Zollner Region

The LC Zollner Region covers an isolated secondary crater cluster near Zollner crater (Figure 3.3). At WAC scales, the craters in this cluster grade from large to small as you go from uprange to downrange. The downrange rims of the craters in this cluster are less well-developed the further downrange they are located within the cluster. These features become gouges which grade to braided terrain furthest downrange. At NAC scales, these craters have very subdued rims and are characterized by smooth material.

3.6 Conclusions

In this chapter, we have examined high-resolution morphologies associated

with lunar secondary craters in order to hypothesize the origin of radar CPR enhancements related to secondary cratering. This investigation revealed that evidence of high-speed debris flow, as proposed by *Oberbeck* (1975) and *Morrison and Oberbeck* (1975), is common at clustered and isolated Tycho secondary craters out to distances of 50 crater radii. The debris flow areas were characterized by smooth terrains (lacking blocks on the 1-10 m size-scale) with disturbed textures on the 100 m scale extending downrange from the craters. These disturbed textures included v-shaped dunes circumscribing the uprange rims of craters and "braided" patterns of v-shaped ridges and gouges extending downrange. Small lineations meters thick and tens to a hundred meters long were also frequently observed associated with these smooth terrains, extending downrange parallel to the braided textures.

In addition to their disturbed textures on the 100 m scale, these smooth terrains frequently breached or draped over the rims of Tycho secondary craters. In these cases, smooth material would form channels cutting the crater rims, typically from a general uprange direction. The smooth units that draped over the crater rims were often observed to have raised margins. The presence of these smooth flows gave the secondary crater rims a rounded and heavily degraded appearance on the scale of LROC NAC images, even when they appeared sharp and well-preserved at the WAC scale.

Block-rich terrains, or BRTs, were observed in isolated patches in relation to the smooth terrains. The location of these BRTs was consistent with deposition by the smooth debris flows. BRTs were most-commonly observed on the leeward sides of topographical obstacles to the flow or at the smooth unit boundaries. Both of these

regions would be areas of low flow velocity and thus regions of preferential block deposition. In general, the smooth flows also overlaid the BRTs, consistent with the blocky material having been transported downrange and deposited by the otherwise smooth flows.

In keeping with the debris surge hypothesis by *Oberbeck* (1975) and *Morrison and Oberbeck* (1975), I propose that these debris flows were initiated by swarms of primary ejecta fragments imparting downrange momentum to the local surface in the areas of these CPR enhancements. The braided or disturbed nature of the downrange terrain is thus explained by interference in a flow with multiple points of origin. Textured terrains are augmented by the diversion of the flow around the raised rims of recently formed small secondary crater clusters. The small craters downrange in secondary clusters are heavily eroded by these debris flows, explaining the progressive gradation from fully-formed craters to v-shaped ridges and wedge-shaped gouges from the front of the cluster to the back.

The debris flows follow behind the primary ejecta curtain. Therefore, the blocky ejecta created by the secondary craters at these regions is entrained by the flows and deposited in elongated streaks downrange from the craters. Scattering from this blocky material on the surface and subsurface is consistent with the elevated values of the radar CPR at 13-and sometimes 70-cm. 13-cm scatterers are below the resolution of the NAC images, so we cannot easily determine if clasts this size are common on the surface in these regions. Concentrations of meter-sized scatterers are not observed on the surface in areas of 70-cm radar CPR enhancements at these craters. The presence of block-rich material extruding from the smooth flows and

excavated by small pit craters is consistent with a layer of blocky material beneath a thin (1.5-3.0 m) layer of fine material.

One of the most important findings in this work is that debris flow morphologies with corresponding radar CPR enhancements are observed at relatively isolated Tycho secondary craters as well as clustered craters with traditional secondary morphologies at the WAC scale. These debris flow morphologies were also observed over a wide range of distances from the parent crater, beginning in the proximal facies 2-3 crater radii from the parent and as far away as the Apollo 17 landing site, a distance of 52 crater radii from Tycho. Therefore, these observations are evidence that debris flow is an important process associated with secondary craters over a broad portion of the lunar surface.

Crater counts of the smooth debris flow yielded young ages, with even younger N(1) ages than Tycho crater, which is dated to ~100 Ma [*Arvidson et al*., 1976]. However, the SFDs of these small primary craters have steeper power-law slopes than the b=-2 values for lunar primary craters with diameters above 1 km. This steep slope appears to be real and not an artifact of small number statistics, but when extrapolated to D = 1 km, it is reasonable that it should yield a lower density than a small crater population with b=-2. Thus, the absolute ages from the best-fit N(1) values are not particularly useful, except to confirm that these flows are at least as recent as the Tycho impact.

The steep slope of these small craters is, in itself, very interesting, as some workers, including *Shoemaker* (1965), predict the presence of a small-diameter primary crater population with a steep SFD slope in addition to the steep secondary

crater population at small diameters. Shoemaker hypothesized that the steep primary craters should dominate below ~200 m. The steep branch here ranges in size from the edge of resolution to ~100m. Above this diameter, small craters appear to have been obliterated due to the debris surges in these regions. Other workers have reported steep slopes for small primary crater populations, most notably on the asteroid Gaspra (*Chapman et al.,* 1996). The craters visible on Gaspra in the 0.2-1.0 km diameter range exhibit similarly steep SFD slopes (*b=-3.1* to *-3.7*) (*Chapman et al.,* 1996). Between 1.0-10.0 km, the YORP and Yarkovsky effects are expected to slightly increase SFD slopes in the near-Earth object (NEO) population compared to main belt asteroids (*McEwen et al.,* 2005; *Morbidelli and Vokrouhlicky*, 2003), but observations indicate that it cannot account for such a dramatic increase in SFD slope for craters in the 0.2-1.0 km size range (*Bottke et al.,* 2005). Further counts of small primary craters on these smooth flows are required to determine whether the SFD steepening observed at these regions is widespread or if some local property has preserved an artificially steepened population.

The observations of prevalent debris flow associated with Tycho secondary craters are also relevant to theories of ray formation and preservation. Workers have established that there are two main factors that contribute to lunar high-albedo rays: composition and maturity [*Hawke et al.,* 2004]. Compositional rays are longer-lived and require rays to contain a larger percentage of primary material than simple maturity rays in order to provide sufficient contrast with the local material [*Hawke et al.,* 2004]. In addition, the ejected primary material must have a sufficiently different composition than the local material. Maturity rays are bright due to short cosmic-ray

and solar wind exposure times of the fresh material reworked when primary ejecta impacted the local surface [*Hawke et al.*, 2004]. The prevalence of ejecta fragment-initiated debris flow, as revealed by this work, supports the findings of *Pieters et al.* (1985) that local material makes up a large percentage of ray material. If this is the case, it may be very difficult to form long-lasting compositional rays, indicating that many lunar rays are likely maturity rays and therefore weather quickly.

The CPR enhancements due to these debris flows, however, are more likely the result of physical scatterers on the surface than the optical properties of the surface material. Therefore, it should take longer for the CPR signature to weather than optical maturation process that degrades high-albedo maturity rays. This means that CPR enhancements can be used to map rays that are no longer visible as albedo signatures. Newton-A is an example of this phenomenon.

This means that, in addition to mixing primary and local material and excavating fresh material that forms high albedo lunar rays, these debris flow scour local highs and fill local lows over large portions of the lunar surface. The erosive power of debris surge was first discussed by *Oberbeck* (1975), but primarily in the context of basin ejecta. This work shows that even moderately-sized lunar complex craters like Tycho or Copernicus can significantly modify large parts of the lunar surface.

Finally, this work highlights the utility of the radar CPR method. By probing the distinctively elongated deposits of blocky material transported downrange from secondary craters by debris flow, the radar CPR method can trace areas which have been modified by ejecta processes and alert workers to the presence of secondary

craters that might go unnoticed without time-intensive searches through high-resolution images where regional context can be difficult to discern. In the next chapter, we will use the radar CPR method to look at the total production of secondary craters by Tycho and Copernicus craters and compare these findings to the results of other workers.

CHAPTER 4

RADIAL DISTRIBUTIONS OF TYCHO AND COPERNICUS SECONDARY CRATERS

4.1 Introduction

We have seen that radar CPR enhancements, particularly at 13-cm, are a good indicator of the presence of Copernican-aged lunar secondary craters. These enhancements occur inside and outside of visible albedo rays. They are observed at secondary clusters and also seen in environments where secondaries are isolated from other secondary craters of a similar size. These CPR enhancements are the result of downrange flow of local material initiated by primary fragments at the base of the ejecta curtain, and are therefore observed out to great distances from the parent crater. All of these properties give the radar CPR secondary crater identification method a unique view of lunar secondary crater populations. Using radar polarization, we can probe a parameter space in which secondary craters are difficult to investigate with photographic methods [*McEwen et al.*, 2005; *Bierhaus et al.*, 2005; *Dundas and McEwen*, 2007].

Having tested and characterized this method, we now employ it in the context of the Tycho and Copernicus secondary crater networks. Tycho crater (D = 86 km) and Copernicus crater (D = 93 km) are two of the youngest large impact features on the Moon [*Arvidson et al.*, 1976; *Bogard et al.*, 1994]. Both of these craters exhibit well-preserved high albedo ray systems which have been studied extensively by

previous workers [e. g., *Shoemaker*, 1965; *Lucchitta*, 1976; *Pieters et al.*, 1985; *Vickery*, 1987; *Campbell et al.*, 1992; *Dundas and McEwen*, 2007].

The aim of the work presented in this chapter is to measure the profile of average secondary crater density with increasing radial distance from the parent crater. Quantifying this density is important for a number of reasons. The first reason is that identifying individual secondary craters in any sample used for age-dating is time-intensive process. A characterization of the statistical secondary crater contamination of a given surface based on the distance from it to the nearest large primary crater allows workers to account for error due to secondary cratering without devoting time and energy to this identification process. Secondary crater identification can also be subjective, so a statistical quantification of secondary contamination with distance standardizes error reporting. One good measure of the level of contamination in a crater population is the cross-over diameter, D_x, below which the crater SFD is dominated by the steep secondary population [*McEwen et al.*, 2005]. Radial profiles of secondary crater production are investigated in this chapter to lead us in the direction of such direct modeling of secondary crater production and contamination.

Several workers have investigated the total production of secondary craters by individual parent primary craters [e. g., *Bierhaus et al.*, 2005; *McEwen et al.*, 2005; *Dundas and McEwen*, 2007]. One of the seminal studies on the relevance of secondary cratering to crater-derived ages is the work of *McEwen et al.* (2005) on the rayed martian crater, Zunil. Zunil is a small, fresh crater with a diameter of 10.0 km [*McEwen et al.*, 2005]. *McEwen et al*. (2005) reported that there is no evidence of the crater or continuous ejecta blanket of Zunil being superposed by younger impact

features. They also searched the martian surface for similar-sized rayed craters and found that Zunil was unique for its size [*McEwen et al.*, 2005]. These two facts led *McEwen et al.* (2005) to argue that Zunil is a very young feature, with an age bracket of 10 Ka – 20 Ma based on the Neukum and Hartmann martian production functions (henceforth: NPF and HPF) [*Hartmann*, 1999; *Neukum et al.*, 2001; *Hartmann and Neukum*, 2001]. *McEwen et al.* (2005) stressed that it is very unlikely that the age of Zunil falls within the young end of this age bracket, with a probability of 0.002 for a Zunil-sized impact occurring in the last 10 Ka.

Zunil secondary craters were identified by *McEwen et al.* (2005) based on membership in clusters of craters with elongated streaks of cold material in nighttime THEMIS IR mosaics of the martian surface. *McEwen et al.* (2005) first noticed the existence of these streaks of low TI material, then recognized that the direction of the streaks converged on a single location on the martian surface: the crater Zunil. They interpreted this as the discovery of the Zunil ray system in the THEMIS IR data [*McEwen et al.*, 2005].

McEwen et al. (2005) used the presence of these nighttime IR rays to map the distribution and size-frequency of Zunil's secondary craters. Their observations yielded large numbers of secondary craters with diameters between 10 and 200 m in diameter [*McEwen et al.*, 2005]. The majority of these secondary craters were observed at large distances from Zunil, with little to no secondary events reported within 16 crater radii of the parent crater [*McEwen et al.*, 2005]. *McEwen et al.* (2005) reported that these craters lacked other defining morphologies beyond the low TI rays. They did, however, report that these craters had very low depth-to-diameter

ratios (d/D from 0.03 to 0.08) compared to the canonical value of 0.2 for bowl-shaped primary craters [*McEwen et al.*, 2005; *Melosh*, 1989]. Some of the craters with low d/D values were neither obviously clustered nor exhibited low TI rays [*McEwen et al.*, 2005]. *McEwen et al.* (2005) speculated that many of these, particularly those which otherwise appeared sharp and very fresh, were also secondary craters.

As a means of corroborating their observational results, *McEwen et al.* (2005) also conducted hydrocode simulations of the Zunil ejecta. Their results indicated that a very large number of secondary craters were produced, upward of 10^9 craters with diameters exceeding 10 m in diameter [*McEwen et al.*, 2005]. However, the spatial distribution of these secondary craters is of even greater importance than their total number. The model of *McEwen et al.* (2005) indicated that, for Zunil crater, 96% of the secondary craters formed at distances greater than 400 km from the parent, while 70% were expected at distances greater than 800 km. At these energies, *McEwen et al.* (2005) warned that nearly all such "background" secondary craters would morphologically resemble small primary craters, thus significantly contaminating the martian cratering record at small diameters.

These results have important implications for the martian chronology. *McEwen et al.* (2005) suggest that a "flattening" of the HPF and NPF martian isochrons needed to be introduced below 300 m diameter in order to accommodate the number of secondary craters identified associated with Zunil. They asserted that the current production functions overestimate the number of small martian craters by as much as a factor of 10^3 in some cases [*McEwen et al.*, 2005]. Observational evidence for this overestimation is provided by *McEwen et al.* (2005). They cite their search for

other bright-rayed craters with diameters between 1-10 km diameters as one example. Based on the number of impacts identified in their global search and the probabilities of these impacts according to the NPF and HPF, *McEwen et al.* (2005) conclude that either Mars has been subject to three very unlikely impacts in the last ~100 Ka (with probabilities less than 0.002), or that the current NPF and HPF isochrons overestimate the frequency of small martian craters.

Another phenomenon cited by *McEwen et al.* (2005) as evidence of the production functions' overestimation of small crater frequency are the frequency of landslides in Vallis Marineris [*McEwen et al.*, 2005]. The frequency of these mass-wasting events grows exponentially toward the present according to gully ages computed with the current martian isochrons [*McEwen et al.*, 2005]. Rather than suggest some process that is progressively accelerating the erosion rate of this canyon, *McEwen et al.* (2005) suggest that the overestimation of the number of small martian craters biases the crater counts on these landslides toward artificially young ages.

The importance of the Zunil and Pwyll secondary crater studies by *McEwen et al.* (2005) and *Bierhaus et al.* (2005) is that they opened the eyes of the community to the influence of secondary cratering raters on other important questions. In particular, the examples of martian gullies and layered deposits provided by *McEwen et al.* (2005) show how inaccurate production functions can drastically alter interpretations of the age.

In this chapter, I compare the radial profiles of Copernicus and Tycho with the Zunil observations. I also compare the radial profile of secondary crater number density with the results of the Zunil hydrocode modeling. McEwen et al. (2005) used

these radial profiles to estimate the cut-off diameter below which secondary craters would dominate the overall crater size-frequency distribution. We can create similar estimates for Tycho and Copernicus for surfaces of varying true age. Additionally, this measurement will confirm or refute the assertion that a large percentage of secondary craters occur at large distances from their parent crater.

A measurement of the production and radial distribution of secondary craters also provides insight on the impact physics of the parent crater, including the properties of the ejecta curtain and the excavation process itself. In the second half of this chapter, I will outline the theory connecting the observed secondary crater distributions to these physical processes. In particular, I will discuss the implications of these measured distributions on the dominant ejection mechanisms of secondary-crater-forming fragments and compare these findings with the earlier work of *Vickery* (1986).

4.2 Data and Methods

The dataset used for counting the secondary crater profiles of Tycho and Copernicus craters was 13-cm ground-based radar obtained in bi-static mode between Arecibo Observatory and the Green Bank Telescope, as outlined in the previous chapters. The secondary craters were identified and characterized using a combination of single channel radar images (typically the SC polarization) and radar CPR mosaics. Craters with characteristic radar CPR enhancements like those described in Chapter 3 were first identified in the radar CPR mosaics (Figures 4.1 and 4.2). Then, the single channel radar images were used to measure the size and location of these craters.

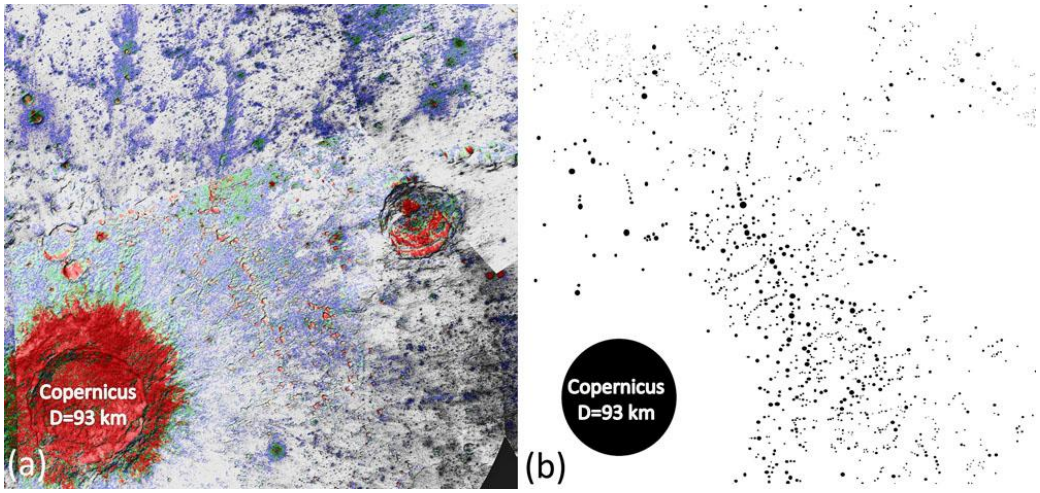

Figure 4.1. 13-cm radar CPR mosaic of the Copernicus region. (a) The area of CPR enhancement were selected to help identify regions where secondary craters could be identified. (b) Secondary craters identified in the northeast quadrant using the radar CPR method. The CPR scale has a maximum value of 2.0.

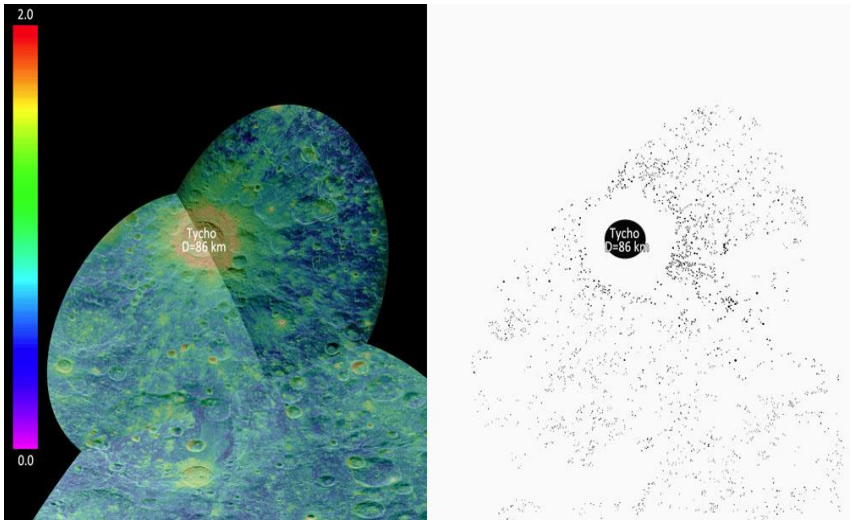

Figure 4.2. 13-cm radar CPR mosaic of the Tycho region. (a) The areas of CPR enhancement were selected to help identify regions where secondary craters could be identified. (b) Secondary craters identified using the radar CPR method.

Specifically, the size of each secondary crater was marked as a filled ellipse in a separated layer in Adobe Photoshop CS4. 5013 secondary craters ranging in size from a few hundred meters to over 2 kilometers in size were identified for Copernicus crater and 2399 secondary craters for Tycho crater. These craters were located within 10 crater diameters of the parent events.

After these secondary craters were marked, the shape layers were exported from Photoshop to the ImageJ program, where a best-fit ellipse was created for each crater and recorded in a CVS file using the "Measure Particles" function. These CVS files were imported into IDL, where the individual craters were re-projected one at a time on the original single channel radar image. Here the ellipse parameters were checked against the crater shape and modifications were made to ensure a good match. This process was completed for all secondary craters down to 1.3 km in diameter for Tycho crater and 1.7 km in diameter for Copernicus. These crater sizes were used for computing the best-fit secondary crater size-frequency distributions.

4.3 Results

After the craters were counted and analyzed to correct for the shapes of the crater rims, the radial profiles were computed. Due to the incomplete azimuthal coverage of the these secondary crater networks in the available 13-cm radar data, the profiles were computed for the NE quadrant extending away from Copernicus and for the SE quadrant surrounding Tycho. These quadrants were chosen because they represented the most continuous coverage. Thus, these profiles should not reflect an artificially low density due to incompleteness, as might have been the case for the SW

Copernicus quadrant or the NW Tycho quadrant. The size-frequency distributions of all the secondary Tycho secondary craters in the SE quadrant are presented in Figure 4.4; the SFD of the Copernicus secondary craters in the NE quadrant is found in Figure 4.3. The slopes of these size-frequency distributions are much like what we would expect for secondary craters; their steep slopes fall between *b=-3* and *-4*, significantly steeper than the *b=-2* "primary" lunar primary crater branch. Additionally, the best-fit density of this average population is very high. At N(1) = 2.3 x 10^{-3} and 5.0 x 10^{-3}, the density of these secondary crater populations (averaged over distances ranging from 1-10 parent crater diameters) are comparable to the density of primary craters expected for 3.5 Ga surfaces according to the *Neukum et al.* (2001) isochrons.

While these averaged populations are intriguing, the purpose of these measurements was to characterize the change of secondary crater density with distance from the parent crater. Therefore, I have also divided the secondary craters measured in these quadrants into radial bins increasing range at intervals of two crater radii from the parent. The size-frequency distributions of these radial bins are given in Figure 4.5 for Copernicus and Figure 4.6 for Tycho. Table 4.1 also compares the best-fit N(1) values for these distributions as a function of increasing range.

The best-fit N(1) values of these secondary crater populations drops dramatically over the first few crater radii, but quickly levels off to values of N(1) ~ 2 x 10^{-3} after about six crater radii. Because the total surface area increases with distance, the actual number of secondary craters that occur in these regions of slightly reduced density are higher compared to the total number of proximal secondary craters

Table 4.1. Best-fit N(1) and b values vs. range.

Range (crater radii)	**Tycho Secondary Craters**		**Copernicus Secondary Craters**	
	N(1)	**B**	**N(1)**	**B**
2	3.5×10^{-2}	-3.7	4.5×10^{-2}	-3.3
4	1.6×10^{-2}	-3.4	2.1×10^{-2}	-3.8
6	2.5×10^{-3}	-2.9	4.7×10^{-3}	-4.1
8	2.3×10^{-3}	-4.6	4.9×10^{-3}	-3.8
10	1.3×10^{-3}	-3.6	2.6×10^{-3}	-3.8
12	9.2×10^{-4}	-4.7	2.2×10^{-3}	-5.6
14	2.1×10^{-4}	-2.6	3.3×10^{-4}	-3.7
16	NA	NA	5.6×10^{-4}	-2.5
18	NA	NA	4.5×10^{-4}	-4.5
1-20	2.6×10^{-3}	-3.8	5.0×10^{-3}	-4.2

Table 4.2. Number of secondary craters vs. range.

Numbers in parenthesis indicate the number of craters used for SFD fitting.
*Radar coverage for this range was incomplete and no SFD was computed

Range (crater radii)	Number of Tycho Secondary Craters		Number of Copernicus Secondary Craters	
	Total Number	Number used for fitting	Total Number	Number used for fitting
2	157	78	313	144
4	188	70	461	92
6	101	59	206	55
10	108	52	595	138
12	144	77	288	87
14	190	140	186	64
16	61	46	102	58
18	NA*	NA*	225	143
20	NA*	NA*	124	57
1-20	951	188	2501	348

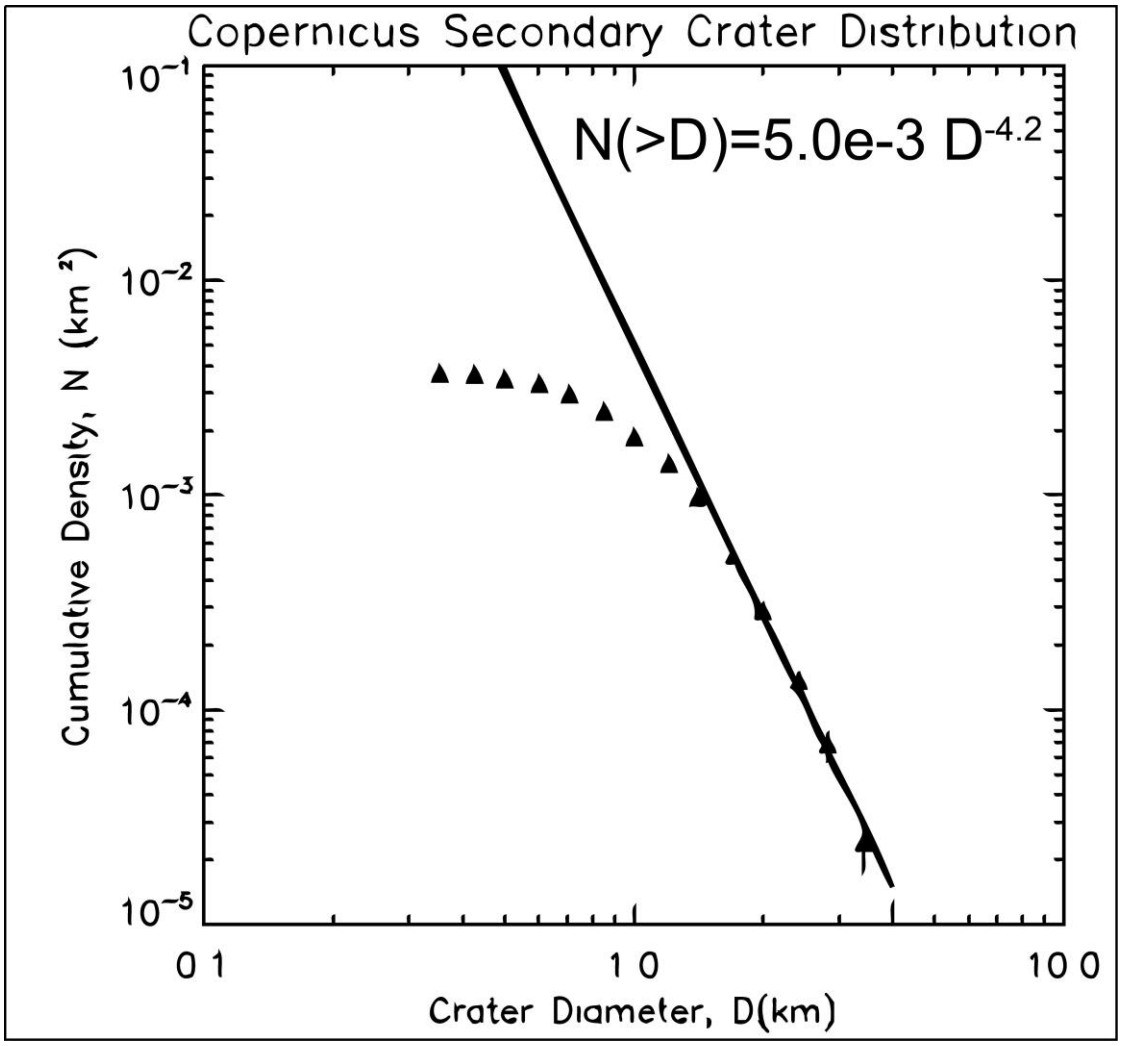

Figure 4.3. The averaged size-frequency distribution of all Copernicus secondary craters in the northeast quadrant.

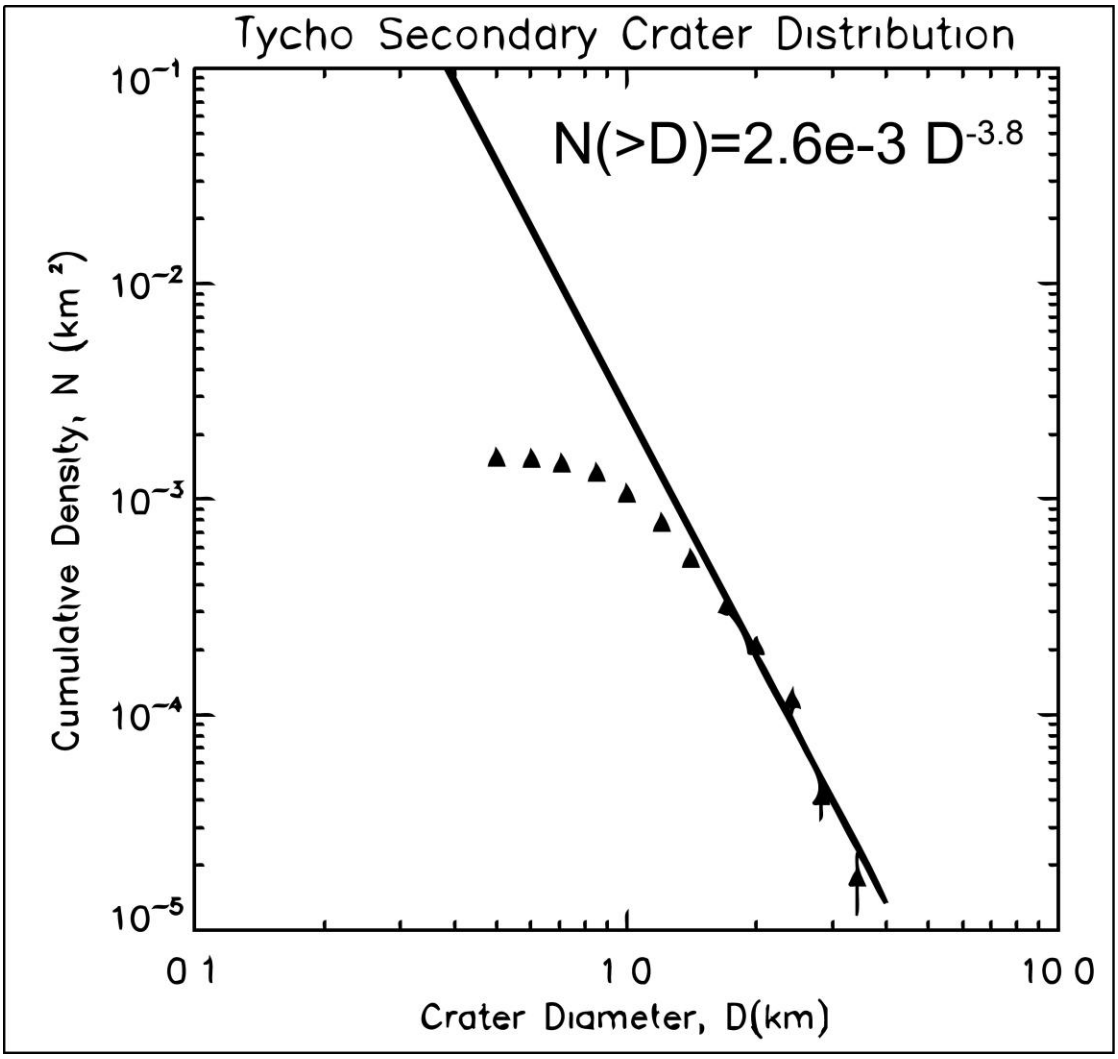

Figure 4.4. The averaged size-frequency distribution of all Tycho secondary craters in the southeast quadrant.

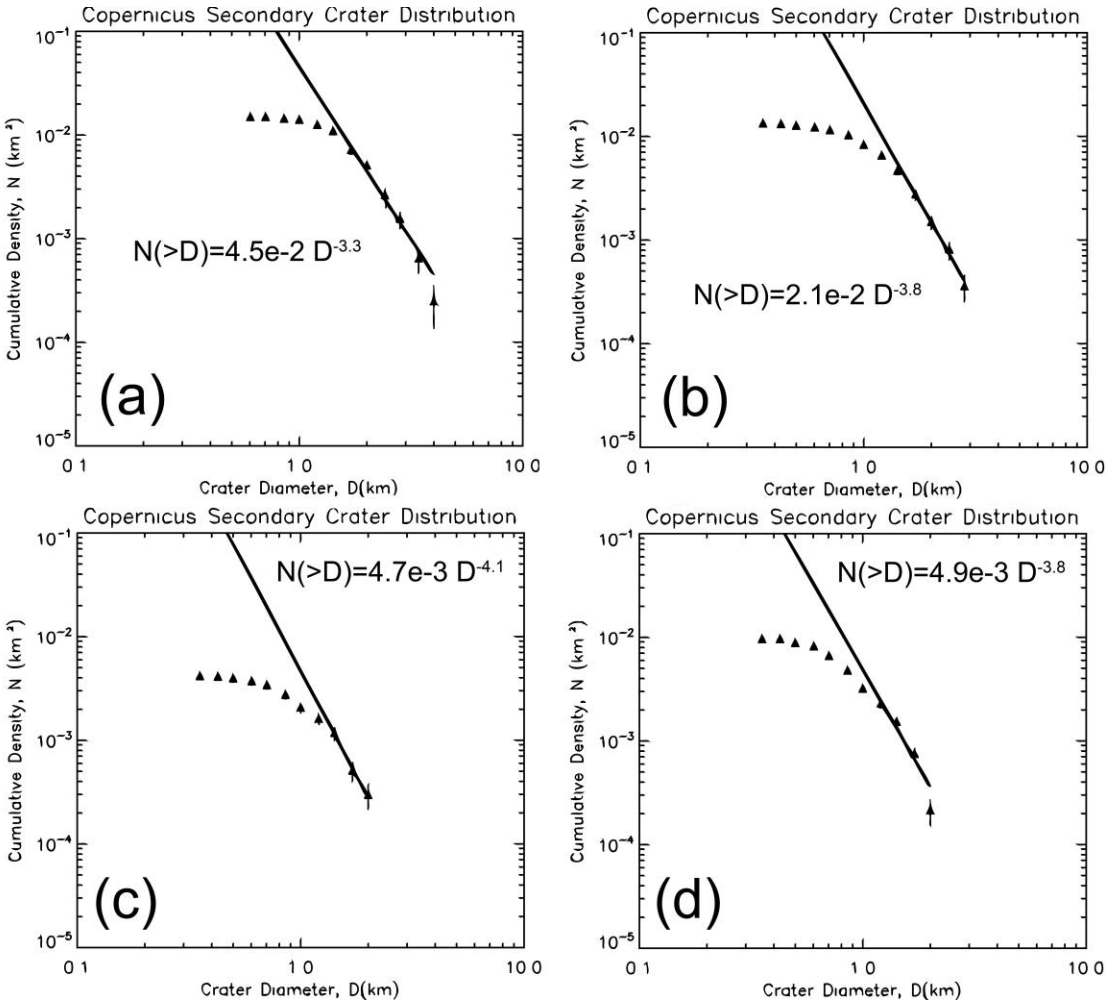

Figure 4.5. Size-frequency distributions of Copernicus secondary craters vs. range: (a) 2 crater radii (b) 4 crater radii (c) 6 crater radii (d) 8 crater radii.

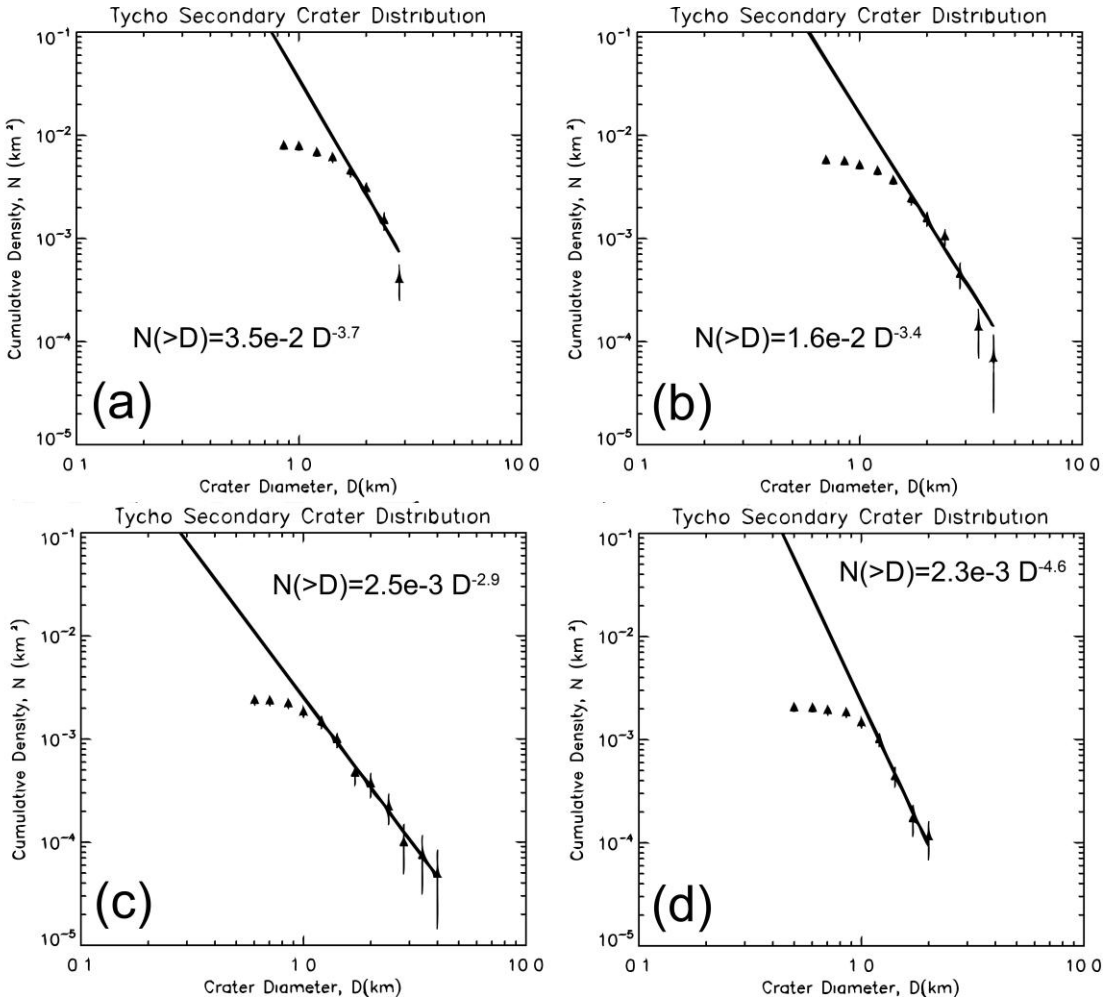

Figure 4.6. Size-frequency distributions of Tycho secondary craters vs. range: (a) 2 crater radii (b) 4 crater radii (c) 6 crater radii (d) 8 crater radii.

(Table 4.1). Therefore, these measurements support the assertions of *Bierhaus et al.* (2005), *McEwen et al.* (2005), *Robbins and Hynek* (2011) and others that distal secondary craters outnumber "obvious" proximal secondary craters.

Using the change of secondary crater density with range measured around Tycho and Copernicus, we can also estimate the cross-over diameter, D_x, as a function of range from these large primary craters. The diameter at which the observed secondary crater densities are equal to primary crater densities for a variety of surface ages are presented in Tables 4.3 and 4.4. The diameter at which the primary density would reach a level ten times that of the secondary crater population, a benchmark for "safe" counting recommended by *McEwen et al.* (2005), is also given. The results in these tables highlight the influence secondary crater populations can have on impact cratering records, even over large distances.

The tables of cross-over diameter are particularly illuminating. They reveal that the measured density of Copernicus and Tycho secondary craters dominated all counts below 1.1-1.7 km on all surfaces younger than 1 Ga in age [*Neukum et al.*, 2001] out to distances of 10 crater radii. Even for ancient surfaces with ages of 4 Ga, the crater population below 170-280 m in diameter is expected to be dominated by secondary craters out to this distance. Within the first six crater radii, all craters below ~1.0 km in diameter can be expected to be dominated by secondary impacts for surfaces of 3 Ga or younger [*Neukum et al.*, 2001]. In general, these results reflect that crater populations surrounding Tycho and Copernicus will be dominated by secondary craters at sizes ranging from 200m – 2.5 km, depending on surface age and distance. These values are slightly less than the 1-4 km transition between the primary

Table 4.3. Cross-over diameter vs. range from Copernicus crater.

*Sizes indicate the second-largest populated bins of the secondary crater SFDs at this range. These values were used because the calculated D_x values were larger than this physical limit.

(a) Equal secondary and primary density

Range (crater radii)	100 Ma	500 Ma	1 Ga	2 Ga	3 Ga	4 Ga
2	2.5 km*	2.5 km*	2.5 km*	2.5 km*	2.5 km*	770 m
4	1.7 km *	1.7 km*	1.7 km*	1.7 km*	1.7 km*	540 m
6	1.7 km *	1.7 km*	1.7 km *	1.6 km	1.3 km	290 m
8	1.4 km *	1.4 km*	1.4 km*	1.4 km*	1.4 km*	240 m
10	1.4 km*	1.4 km*	1.4 km*	1.3 km	1.0 km	170 m

(b) Primary density ten times secondary density

Range (crater radii)	100 Ma	500 Ma	1 Ga	2 Ga	3 Ga	4 Ga
2	2.5 km*	2.5 km*	2.5 km*	2.5 km*	2.5 km*	2.5 km*
4	1.7 km *	1.7 km*	1.7 km*	1.7 km*	1.7 km *	1.7 km*
6	1.7 km *	1.7 km*	1.7 km *	1.6 km	1.7 km *	870 m
8	1.4 km *	1.4 km *	1.4 km *	1.4 km *	1.4 km *	870 m
10	1.4 km*	1.4 km *	1.4 km *	1.4 km *	1.4 km *	610 m

Table 4.4. Cross-over diameter vs. range from Tycho crater.

*Sizes indicate the second-largest populated bins of the secondary crater SFDs at this range. These values were used because the calculated D_x values were larger than this physical limit.

(a) Equal secondary and primary density

Range (crater radii)	100 Ma	500 Ma	1 Ga	2 Ga	3 Ga	4 Ga
2	2.5 km*	2.5 km*	2.5 km*	2.5 km*	2.5 km*	710 m
4	2.5 km*	2.5 km*	2.5 km*	2.5 km*	2.5 km*	380 m
6	1.7 km*	1.7 km*	1.7 km*	1.5 km	1.0 km	30 m
8	1.7 km*	1.7 km*	1.5 km	1.1 km	960 m	280 m

(b) Primary density ten times secondary density

Range (crater radii)	100 Ma	500 Ma	1 Ga	2 Ga	3 Ga	4 Ga
2	2.5 km*	2.5 km*	2.5 km*	2.5 km*	2.5 km*	2.5 km*
4	2.5 km*	2.5 km*	2.5 km*	2.5 km*	2.5 km*	2.0 km
6	1.7 km*	1.7 km*	1.7 km*	1.7 km*	1.7 km*	360 m
8	1.7 km*	1.7 km*	1.7 km*	1.7 km*	1.7 km*	680 m

and secondary branches of lunar SFDs observed by *Shoemaker* [1965], but Tycho and Copernicus are small craters compared to basin-sized events. Contributions due to these larger events may explain the discrepancy. Overall, these predictions of the cross-over diameter, D_x, as a function of range are strong evidence for the importance of secondary cratering to the lunar impact record.

4.4 Ejecta Fragment Size-velocity Distributions

These predictions of the cross-over diameter between primary and secondary crater populations surrounding Tycho and Copernicus craters are useful recommendations, but they only represent the secondary cratering of two relatively similarly-sized primary craters. Can we generalize these observations to provide a broader context for secondary crater contamination of the lunar cratering record? In order to make more general predictions, we must first connect the measured distribution of secondary craters to the underlying impact physics of the parent events. Once we have outlined the connection between the observations and the theory, we can extrapolate to a broader statement about secondary crater production as a function of crater size.

Vickery (1986) investigated the size-frequency distributions of the lunar craters Copernicus and Aristillus (D = 55 km) and compared these distributions to the impact crater scaling relationships derived by *Holsapple and Schmidt* (1982). In this work, *Vickery* (1986) measured the size-frequency distributions of secondary craters of Copernicus and Aristillus as a function of distance from their parent craters. The crater sizes were then converted to ejecta fragment SFDs using their inferred impact

velocities and the *Holsapple and Schmitt* (1982) scaling relations. The impact velocity was computed using the ballistic equation for a spherical body:

$$\tan\varphi = (v_{ej}^2 \sin\theta\cos\theta)/(gR_p - v_{ej}^2\cos^2\theta) \quad \textbf{(4.1)}$$

where $\varphi = R/2R_p$ is the half-angular distance of travel on a sphere with radius R_p, R is the distance from the secondary crater to the parent impact, g is the local acceleration due to gravity, v_{ej} is the fragment ejection/impact velocity, and θ is the impact angle, henceforth assumed to be 45° [*Vickery*, 1986].

Vickery (1986) took great care to determine the appropriate scaling relation for converting the measured crater sizes and impact velocities to realistic fragment diameters. Crater scaling laws are different depending on whether the crater forms in the gravity regime, where the work done against gravity to excavate the crater is large compared to the work done against the target strength, or the strength regime, where the opposite is true. Mathematically, in the gravity regime:

$$Y/g\rho R_c << 1 \quad \textbf{(4.2)}$$

where Y is the target strength, ρ is the target density, and R_c is the transient crater radius [*Housen et al.*, 1983]. Conversely, this approximation no longer holds in the strength regime. As the name implies, the target's internal strength is the dominant factor under these conditions. Therefore, in the strength regime:

$$Y/g\rho R_c \geq 1 \quad \textbf{(4.3)}$$

Based on the scaling laws of *Holsapple and Schmidt* (1982) and typical impact velocities of lunar primary ejecta, the transition between these two regimes occurs for fragments between 17-63 m in diameter [*Vickery*, 1986]. Therefore, both the gravity and strength regime scaling relations were used to convert the crater sizes to fragment

diameters [*Vickery*, 1986]. The relation used by *Vickery* (1986) for the strength regime was:

$$d_f = 0.593\, D_{obs} \sin^{-2/3}\theta (Y/\delta U^2)^{0.236} \quad \textbf{(4.4)}$$

where d_f is the ejecta fragment diameter, D_{obs} is the observed secondary crater diameter, δ is the target/fragment density, U is the fragment impact velocity, and Y is estimated as $\sim 10^7$ Pa. For impacts into a porous target (i.e., lunar regolith) in the gravity regime:

$$d_f = 0.76\, D_{obs}^{1.2} (\sin\theta)^{-0.4} (g/U^2)^{0.236} \quad \textbf{(4.5)}$$

and impacts into non-porous targets (i.e., lunar maria) in the gravity regime [*Vickery*, 1986]:

$$d_f = 0.753 D_{obs}^{1.28} (\sin\theta)^{-1/3} (g/U^2)^{0.277} \quad \textbf{(4.6)}$$

Using these scaling relationships, *Vickery* (1986) computed the size-velocity distributions for the Aristillus and Copernicus secondary crater-forming ejecta. The size-velocity distribution for the ejecta of the martian crater Dv were also compiled, but as this is only an indirect comparison to the observations in this thesis, we will not discuss it here.

The Copernicus and Aristillus results revealed that fragments ejected a low velocities tended to be much larger than predicted by the spallation models of *Melosh* (1984), whereas the fragment size dropped noticeably to match the spall block sizes at high velocity. *Vickery* (1986) concluded that these results were consistent with the domination of the size-velocity distribution by two different ejection processes for low vs. high velocity fragments. In order to understand the difference between these two

processes, we backtrack a moment to discuss the general mechanisms of impact crater excavation.

Melosh (1989) divided the impact cratering process into three stages: (1) Contact and Compression, (2) Excavation, and (3) Modification. The contact and compression stage begins with the initial contact between the target surface and the incoming projectile. On impact, the kinetic energy of the projectile is transferred to the surface in the form of a spherically expanding shockwave [*Melosh*, 1989]. This shockwave moves radially away from the point of impact, compressing the target material. Another shockwave moves backward through the projectile. While it does not play a dominant role in the excavation of the volume of the crater, these shockwaves produce the highest peak pressures in the impact process [*Melosh*, 1989]. The target and projectile materials are loaded to pressures in the 100-1000 GPa range, depending on impact velocity [*Melosh*, 1989]. Because free surfaces cannot maintain non-zero pressure, these shockwaves reflect at free boundaries, creating rarefaction (or "release") waves of equal magnitude but opposite sign, satisfying the boundary condition [*Melosh*, 1989]. The release waves propagate away from the impact point, releasing the compressed materials from high pressure. This rapid depressurization is responsible for the creation of the bulk of the vapor and melt associated with the impact [*Melosh*, 1989].

Another consequence of this shockwave reflection early in the impact cratering process is that high velocity, low-shock material is ejected via a process called spallation. Because the target surface cannot support a non-zero pressure, the rarefaction wave and the shock wave add to zero at all points on the surface [*Melosh*,

1989]. However, at some distance below the surface, the reflected rarefaction wave reaches the target material before the shockwave has fully risen in that location. This decreases the peak shock pressures achieved in a small region just below the surface sometimes called the "interference zone" [*Melosh*, 1989]. In this interference zone, the material closest to the surface is least shocked, with the shock levels increasing rapidly with depth, resulting in a depth where the tensile strength of the material is suddenly exceeded and cracks begin to form in tension. Above the depth at which this fragmentation occurs, the target material is launched in large "spall plates" [*Melosh*, 1989]. Because of the interference of the shock and rarefaction waves in these near surface zones, the ejection velocities in these regions can be very high [*Melosh*, 1989]. Thus, spall blocks are a good source of low-shock, high-velocity ejecta, as is required to explain the characteristics of the martian SNC meteorites [*Melosh*, 1989]. Despite the unique nature of this ejecta, it only comprises a small volume of the total excavated material, on the order of a few percent [*Melosh*, 1989]. Spalled blocks at low velocities have some chance of remaining intact (e.g., the kilometer-sized limestone mega-blocks observed near the 22-km diameter Ries crater on Earth [*Melosh*, 1989]), but the residual elastic stresses in blocks ejected at several hundred meters per secondary is likely to fragment such spall blocks in transit before impact [*Melosh*, 1989; *Vickery*, 1986].

Vickery (1986) compared the measured size-velocity distributions for Copernicus and Aristillus with theoretical maximum spall block sizes computed by *Melosh* (1984). At high fragment impact velocities, the observations were consistent with the maximum predicted spall blocks, assuming 10-20 km/s primary crater impact

velocities [*Vickery*, 1986]. Of the three scaling models used, the gravity regime impacts into a non-porous target best fit the predictions based on the spallation mechanism. These fits were very good for distal secondary craters with higher impact velocities, but both the Copernicus and Aristillus observations reported much larger (up to greater than a factor of two) fragments in the proximal ejecta than predicted by the spallation mechanism [*Vickery*, 1986]. This discrepancy was also observed when the fragment sizes were derived using the strength regime scaling laws [*Vickery*, 1986]. To understand *Vickery* (1986)'s interpretation of the anomalously large fragment sizes at low impact velocities, we consider the behavior of the shockwave in the target.

As it moves away from the point of impact, the shockwave energy decreases rapidly, with numerical simulations predicting an R^{-3} dependence on distance from the impact point [*Melosh*, 1989]. The reason for this steep dependence is that shock energy is not just spread out across a hemisphere of expanding surface area, but is also lost to thermodynamically irreversible processes (for example, pore compression) in the target as it propagates. After a few projectile diameters into the target, the shock energy dissipates to the strength of a strong elastic wave [*Melosh*, 1989]. The arrival of the release wave at the back of the projectile defines somewhat arbitrary end of the compression phase. At this point, both the target and projectile materials are compressed and the projectile energy has been fully transferred into the target [*Melosh*, 1989].

The excavation stage follows the contact and compression stage. True to its name, this is the stage during which the transient crater is excavated. A common

misconception is that the crater is created during the high pressure phase of the impact process, but this is not the case [*Melosh*, 1989]. The fragmentation of the target material is actually accomplished in tension by the rarefaction wave, not in compression by the stress wave [*Melosh*, 1989]. When this fractured material is released from high pressure, it has a residual non-zero velocity directed outward from the target surface. As a rule, this velocity scales as a function of distance from the transient crater rim, with the highest ejection velocities at the center of the transient crater [*Housen et al.*, 1983]. The exact velocity of the ejecta depends on a number of impact parameters, including total energy and target strength. Based on the size-velocity measurements of Copernicus and Aristillus ejecta, *Vickery* (1986) hypothesized that the sizes of the proximal ejecta fragments derived from the scaling relationships actually reflected the effective size of cluster of fragments ejected by this lower-velocity excavation flow.

Using the secondary crater radial profiles measured for Copernicus and Tycho craters with the radar CPR method, I converted the crater sizes to ejecta fragment size-frequency and size-velocity relationships. I used the same scaling relationship as *Vickery* (1986), employing the gravity regime into a non-porous target for the Copernicus ejecta and the gravity regime into a porous target and non-porous target for the Tycho ejecta. The scaling laws for a gravity-regime impact into a non-porous target provided the best fit of the data to the spallation theory for both Tycho and Copernicus. The resulting size-velocity distributions are presented in Figures 4.7 and 4.8. As we can see from the figures, our measurements for Copernicus are in good agreement with those of *Vickery* (1986) with the exception of two large fragments at

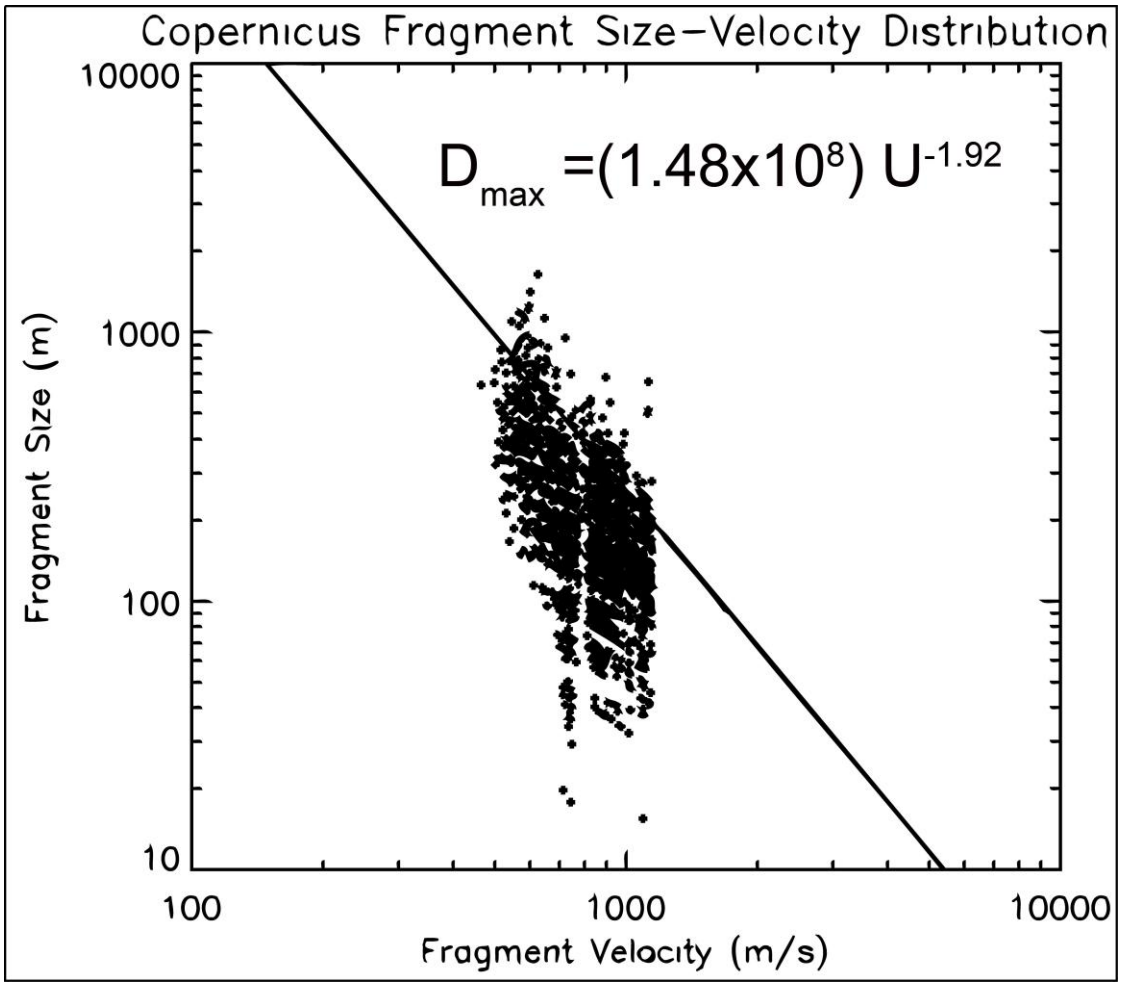

Figure 4.7. Size-velocity distribution of Copernicus ejecta in the northeast quadrant. A scaling relationship for an impact into a non-porous target in the gravity regime was used to convert crater sizes to fragment sizes [*Vickery*, 1986]. The solid line represents the maximum theoretical fragment size as a function of ejection velocity [*Vickery*, 1986]. The apparently discrete curves in fragment size are an artifact of the discrete nature of the size measurements (i.e., the pixel resolution). A similar artifact was observed by Vickery, 1986.

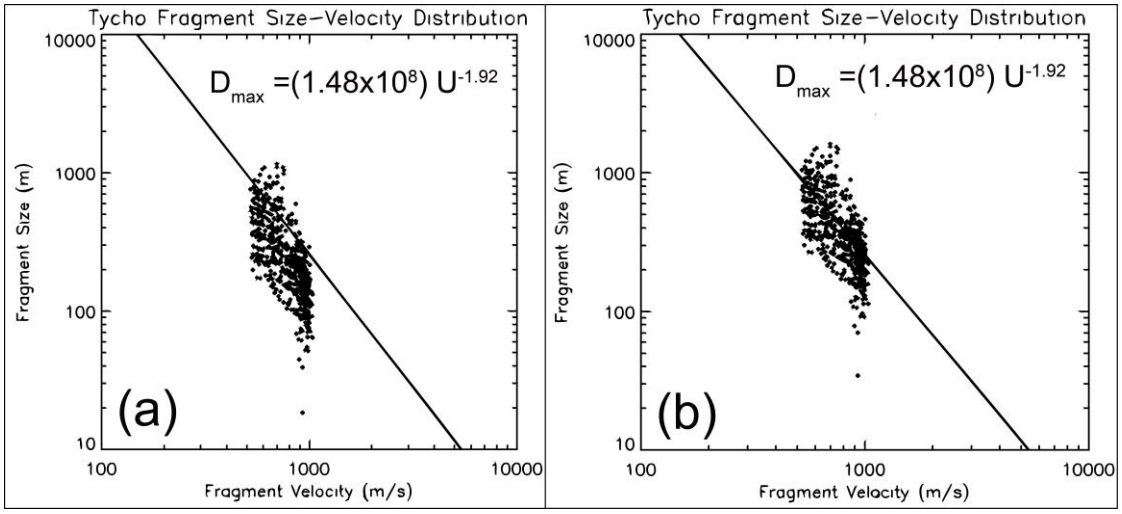

Figure 4.8. Size-velocity distribution of Tycho ejecta in the southeast quadrant. (a) Impact into a non-porous target in the gravity regime [*Vickery*, 1986]. (b) Impact into a porous target in the gravity regime [*Vickery*, 1986]. The solid lines represent the maximum theoretical fragment size as a function of ejection velocity [*Vickery*, 1986].

high velocity, which probably reflect misidentification of small primary craters as Copernicus secondaries. Otherwise, the data measured here fit the theoretical maximum spall block size [*Vickery*, 1987] very well at high impact velocities. For the low-velocity ejecta near the parent crater, however, the fragment sizes inferred from the scaling laws exceed the maximum spall block sizes by more than a factor of two. Following the analysis of *Vickery* (1986), I interpret this change in fragment size with distance as evidence of two separate ejection mechanisms dominating the secondary cratering process at high and low impact velocities. High-velocity secondary crater impacts appear to be dominated by fragmented spall blocks, while low-velocity secondary craters are the result of clusters of material ejected by the excavation flow. This clustering results in the artificially large inferred fragment sizes in this regime, since the diameter of the cluster of fragments is approximately equal to the fragment size derived from the scaling laws.

This interpretation is also consistent with the debris flow morphologies frequently observed at distal secondary craters with radar CPR enhancements. In particular, the tendency of these spall blocks to fragment and disperse with distance from the parent explains the instances of isolated distal secondary craters with flow morphologies. In the previous chapter, it was hypothesized that blocks large enough to form secondary craters might be dispersed at these distances but also accompanied by swarms of smaller ejecta capable of starting debris flow but not large enough to form actual craters. The ejecta size-velocity relationships measured in this chapter provide a source for these small fragment swarms: the break-up of single, dispersed,

large spall blocks into a slightly smaller, crater-forming fragment and a collection of numerous very small fragments.

4.5 Crater Scaling Relationships

Having characterized the ejecta fragment distributions and the corresponding size-velocity distributions, we return our attention to the relationship between these distributions and the impact physics of the parent event. *Housen et al.* (1983) derived a series of impact crater scaling relationships for the gravity and the strength regimes. One of these scaling laws expresses the volume of crater ejecta produced above a given ejection velocity as a function of the target properties and a coupling parameter, *C*. The logic behind the coupling parameter is that the energy and momentum of the projectile that forms the parent crater are coupled into the target early in the impact process, during the aforementioned contact and compression stage [*Housen et al.*, 1983; *Melosh*, 1989]. After this point, the combined projectile properties are reflected through the influence of the coupling parameter, but the influence of individual aspects, such as impact angle or projectile velocity, cannot be separately determined [*Housen et al.*, 1983]. Here, we use this degeneracy to our advantage. The velocity, *v*, of ejecta launched from a distance, *x*, from the rim of a primary crater with radius, *R*, is a function of eight variables [*Housen et al.*, 1983]:

$$v = v(\delta, a, U, \rho, Y, g, x) \qquad \textbf{(4.7)}$$

where δ is the projectile density, *a* is the projectile radius, and *U* is the projectile impact velocity. The coupling parameter, *C*, is a function of these projectile properties:

$$C = C(\delta, a, U) \quad \textbf{(4.8)}$$

By writing the crater radius in terms of this coupling parameter, *Housen et al.* (1983) reduce the original equation of eight variables to six:

$$R = R(C, \rho, Y, g) \quad \textbf{(4.9)}$$

Where the three fundamental dimensions are length, *L*, mass, *M*, and time, *T* [*Housen et al.*, 1983]. The pi-scaling theorem therefore states that the expression can be written in terms of 6-3 = 3 dimensionless ratios:

$$v/\sqrt{gR} = F(x/R, Y/\rho gR) \quad \textbf{(4.10)}$$

where *F* is a function of unknown form [*Housen et al.*, 1983]. Combining the dimensionality of the coupling parameter:

$$C = L^{\psi}M^{\varphi}T \quad \textbf{(4.11)}$$

where ψ and φ are constants, with the three dimensionless ratios from the pi-theorem yields the expression [*Housen et al.*, 1983]:

$$v/\sqrt{gR} = (x/R)^{-ex}\, F(Y/\rho gR) \quad \textbf{(4.12)}$$

Here, the exponent, e_x, is given by:

$$e_x = -(\psi + 3\varphi + 1) = (3-\alpha)/2\alpha \quad \textbf{(4.13)}$$

where α is the scaling exponent derived by *Holsapple and Schmidt* (1982) [Housen et al., 1983]. Using similar reasoning, Housen et al. (1983) derived a general expression for the volume of ejecta, V_e, launched above velocity, *v*:

$$V_e/R^3 = F(Y/\rho gR)\, (v/\sqrt{gR})^{-ev} \quad \textbf{(4.14)}$$

Where e_v is given by:

$$e_v = 6\alpha/(\alpha-3) \quad \textbf{(4.15)}$$

In the gravity regime, where target strength is negligible, we are left with an expression for the volume of material ejected from the parent crater as a function of ejection velocity and crater size [*Housen et al.*, 1983]:

$$V_e/R^3 = q_1 (v/\sqrt{gR})^{-6\alpha/(\alpha-3)} \quad \textbf{(4.16)}$$

Plotting the scaled total volume of ejecta observed above a given velocity, V_e/R^3, against the scaled velocity $v/\sqrt{gR}$, we can test if the Tycho and Copernicus secondary craters obey these distribution laws. The plots of these quantities for Tycho and Copernicus are presented in Figures 4.9 and 4.10.

The measurements of scaled volume vs. velocity reveal that the scaling laws adapted by *Housen et al.* (1983) are not good fits for the volume of material ejected at high velocities to form distal secondary craters. If the data did fit the model, we would expect Figures 4.9 and 4.10 to plot as straight lines with slopes between -1 and -2. Instead, the high velocity ejecta measured at Tycho and Copernicus have very steep slopes (-9.1 and -5.5, respectively), with a kink in the distribution toward shallower negative slopes at lower velocities.

The shapes of these curves do, however, support our interpretation of the size-velocity distributions in the previous section. Because of the use of the coupling parameter, the scaling relationships derived by *Housen et al.* (1983) ignore the early-time spallation process and focus, instead, on the volume ejected by the excavation flow. Therefore, if spallation is the dominant process in ejecting distal secondary crater-forming fragments, it makes sense that the lower-velocity ejecta provide a better fit to the theoretical scaling relationship than the high-velocity ejecta. These results also confirm that spallation, and thus distal secondary cratering, makes up a small

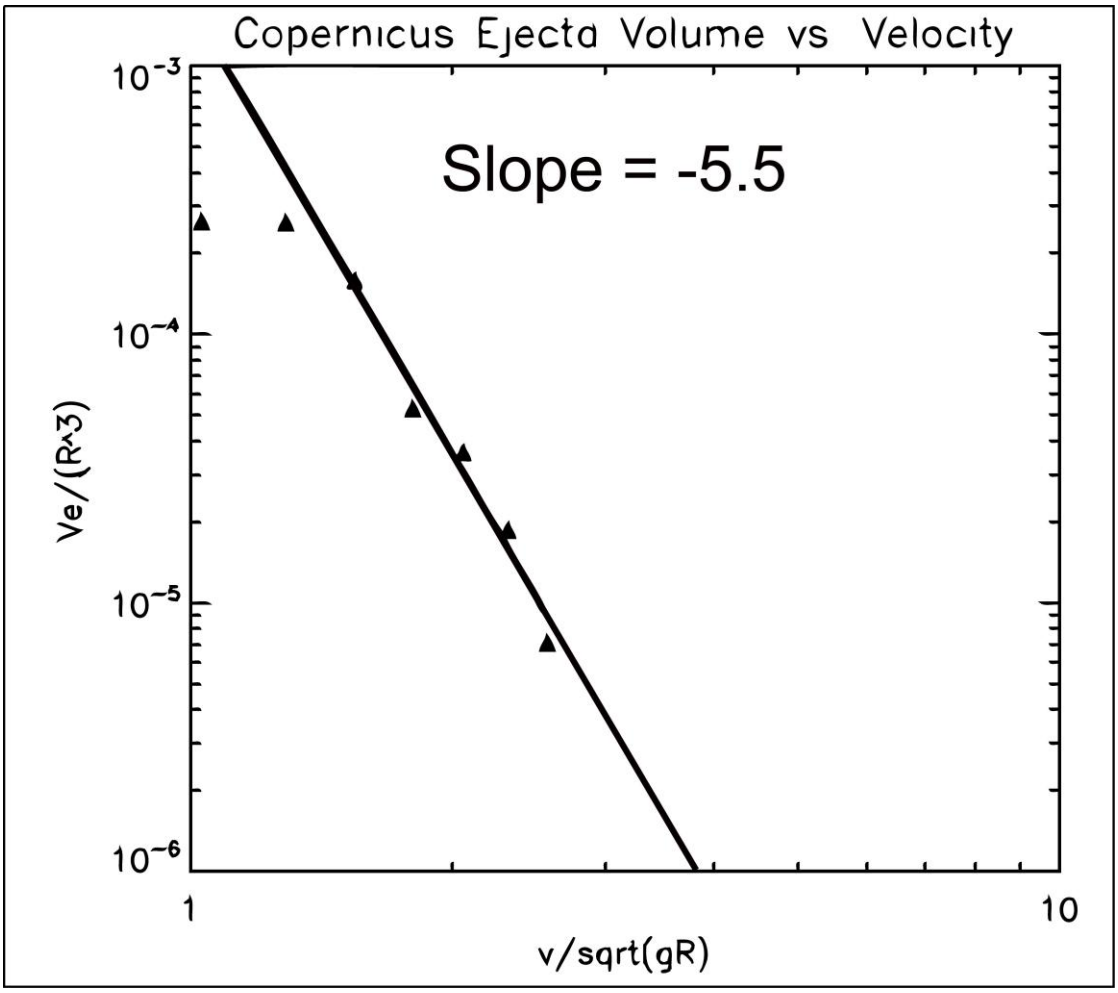

Figure 4.9. Dimensionless volume of Copernicus ejecta launched above velocity, v, plotted against dimensionless velocity.

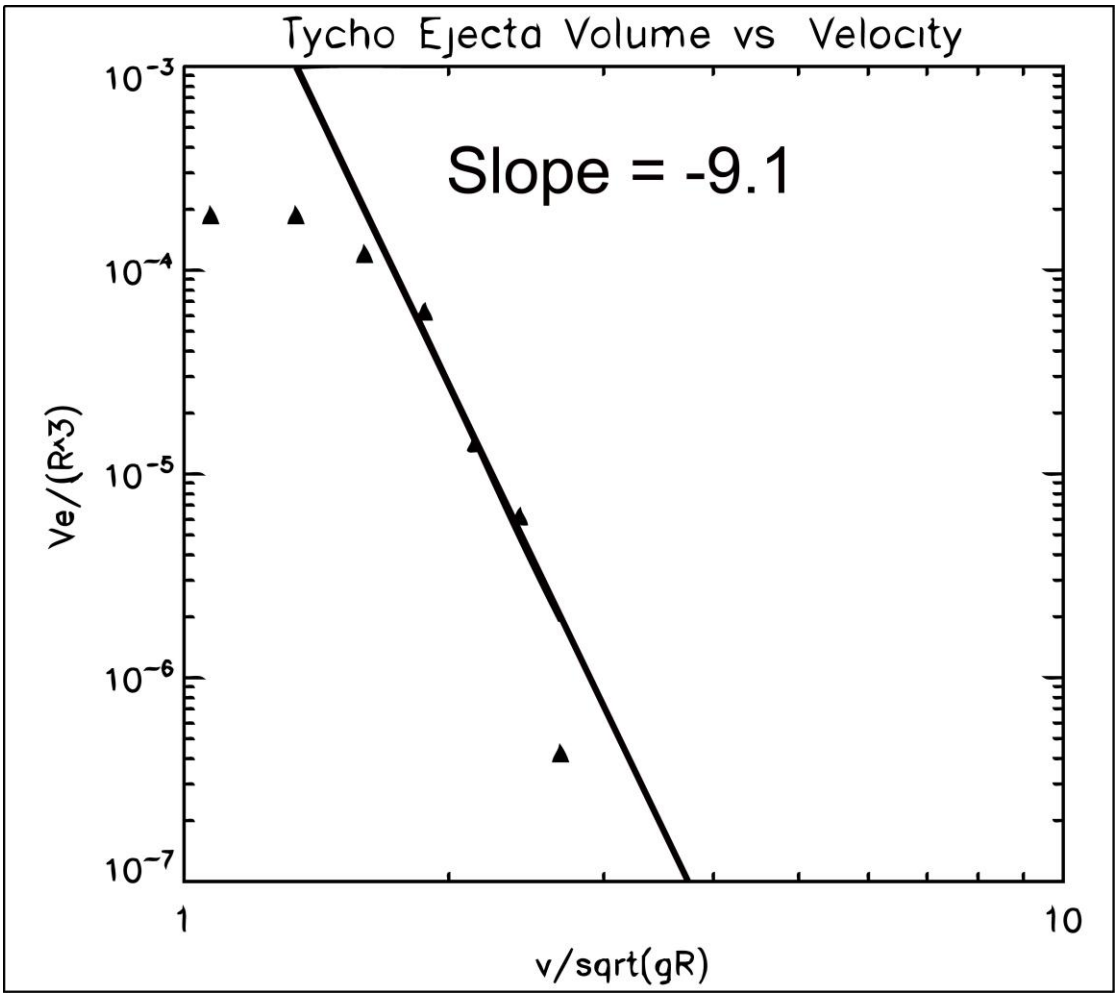

Figure 4.10. Dimensionless volume of Tycho ejecta launched above velocity, v, plotted against dimensionless velocity.

fraction of the volume of total material excavated from the crater, particularly compared to material ejected at low velocity into the continuous ejecta blanket or proximal secondary craters.

4.6 Conclusions

In summary, then, the observations of the radial profiles of Tycho and Copernicus secondary crater production support the claims of previous workers that distal secondary craters comprise a significant fraction of the total population of secondary craters produced by a given impact, though they represent a small volume of total excavated material. Again, the spalled ejecta represent high velocity, low-shock fragments (Melosh, 1989). Although they may not comprise a large fraction of the total ejected volume, this material has a high impact energy to fragment size compared to more proximal ejecta. Measurements of Tycho and Copernicus secondary crater density with distance from the parent using the radar CPR method revealed that the N(1) value of secondary crater populations at these large primary craters decreased rapidly over the first few crater radii but leveled out around $N(1) \sim 10^{-3}$ craters/km^2 for distances out to 10 crater radii. The equivalent N(1) age associated with this density according to the *Neukum et al.* (2001) isochrons is ~1 Ga. These high secondary crater densities provide strong rationale for utilizing multiple secondary crater identification methods, such as spatial clustering [e. g., *Robbins and Hynek*, 2011; *McEwen et al.*, 2005] or the radar CPR method outlined here, to identify potential secondary craters whenever craters are counted for age-dating.

Additionally, the computed distributions of secondary-crater-forming primary ejecta fragments suggests that the majority of high-velocity secondary craters are formed by fragmented spall blocks ejected from the near surface zones of the parent crater. In order to better model the production of "background" secondary craters associated with parent events over a range of sizes, the physics of fragmentation in this interference zone should be researched in greater detail. The analysis of the secondary crater radial profiles of Tycho and Copernicus crater highlight the importance of secondary craters to the overall lunar cratering record. The radar CPR method has proven to be an excellent tool for probing distal secondary crater populations of the Moon, including isolated secondary craters that may be overlooked by photographic methods.

CHAPTER 5

CONCLUSIONS

In this work, we have seen that secondary cratering plays an important role modifying the lunar surface. Using radar CPR enhancements as a proxy for secondary craters, we have investigated the ray systems of Tycho and Copernicus craters. Over the course of these investigations, we have seen that radar polarization is a useful technique for secondary crater identification. Secondary craters identified in this thesis were found inside and outside of high-albedo primary crater rays. They displayed a series of unique morphologies at sub-kilometer scales. Some occurred in tight clusters. Others were relatively isolated and not easily identifiable as secondary craters on the WAC scale. Isolated kilometer-sized secondary craters were observed, but all those with radar CPR enhancements at 13-cm displayed debris flow morphology at the NAC scale.

The presence of distinctive identifying features associated small secondary craters at large distances from the parent crater, both in and outside of very tight clusters, is heartening news for crater counters. As we have discussed at length, one of the great difficulties in determining the extent of secondary contamination of lunar isochrons is the difficulty in distinguishing between small primary craters and distal secondary craters based on crater morphology alone. This work not only provides another way of identifying secondary craters, but, also a method that probes a subset of secondary craters that may be overlooked by other methods.

The radar CPR method has revealed the presence of secondary craters with no obvious clustering or secondary morphologies on the WAC scale. "Hidden ray" regions were identified upward of 1000 km from Tycho crater. Hidden rays were defined as dense clusters of secondary craters which would not have been identified in WAC resolution photographs without the radar CPR method. However, further investigations revealed that, in 50 cm/pixel resolution photographs, debris morphologies were visible in these areas. When high-resolution images are not available, the radar CPR method can alert workers to the presence of secondary craters without obvious secondary crater morphologies. Even if high-resolution images are available, finding these craters without regional context may prove difficult. In these cases, the radar CPR method can be used to screen for subtle secondary craters that can be observed in finer detail with photographic datasets. The hidden ray population of Tycho secondary craters measured at Newton and Newton-A craters had a number density equivalent to a billion-year-old surface below 1 km diameter, as measured by *Neukum et al.* (2001)'s isochrons. Including such a secondary population in the size-frequency distribution of young lunar surfaces, such as fresh crater ejecta blankets or rays, would significantly over-estimate the true age.

Oberbeck (1975) and *Morrison and Oberbeck* (1975) proposed the debris surge as a mechanism to explain the erosion of secondary craters around lunar basins. The debris surge model invokes interactions between primary ejecta fragments and the local surface to create ground-hugging flows of dry material moving downrange at high velocity. As this work affirms, the fragments that initiate these surges need not all be large enough to form secondary craters. This means that, given sufficient

clustering of small ejecta fragments, large, otherwise isolated-appearing secondary craters can exhibit debris surge morphology. We saw this in several instances, including at Tycho secondary craters in the Clavius, Lilius, and Newton regions. Because the debris surge follows behind the ejecta curtain, it modifies the newly created secondary craters, filling in low regions and degrading crater rims [*Morrison and Oberbeck*, 1975]. These surges also create deceleration dunes—uprange deposits of material slowed by obstacles to the flow, such as crater rims.

The secondary crater clusters observed with radar CPR enhancements exhibited distinctive morphologies at the 50 cm/pixel scale of LROC NAC images. These morphologies included prominent v-shaped dunes uprange of secondary craters and braided or disturbed textures downrange from the larger craters in the cluster. These features have been associated with secondary crater clusters, but this work revealed that they are also present at smaller scales at relatively isolated secondary craters as well. We also observed that the intercrater material surrounding these crater clusters was very smooth, lacking blocky material on the 1-10 m scale. These smooth units repeatedly showed evidence of flow deposition, including deflection around topographic obstacles, breached crater rims, and linear and arcuate features indicating flow direction.

Certain morphologies observed in these debris flows indicate that melt may be incorporated into the flows. The flow units were smooth and darker than surrounding terrain, with occasional sharp, raised margins. Impacts near the edge of these units have not disturbed the margins, indicating non-negligible internal strength. Similar morphologies were observed at kilometer scale primary craters, in regions where

impact melt splashed over the crater rim and then flowed back down into the crater. In these instances, smooth, dark material flowed downhill, producing lobate margins with higher concentrations of blocks than the rest of the flow. This same property was observed at the margins of flows at secondary craters, where block-rich terrains were most commonly recorded.

Distal deposits of impact melt have been proposed to explain smooth ponds of dark material near the Tycho antipode on the lunar far side (*Robinson et al.*, 2011). The creation of distal melt ponds may represent scenarios in which melt dominates the ejecta delivered to a given locality. Other clusters may contain no melt. The clusters with arcuate ridges and raised flow margins observed in this work likely represent a scenario somewhere between these two end-members.

Areas exhibiting debris flow morphology were frequently observed in the Tycho ray system and at Copernicus secondary craters in Mare Imbrium. Debris flow, therefore, appears to be a typical by-product of secondary cratering on the Moon, both in the highlands and on the maria, where we would expect thinner regolith to provide a smaller volume of unconsolidated material to contribute to flows. Due to its widespread occurrence, we stress that secondary crater initiated debris flow is an important process for reworking the lunar surface. It plays a major role in reworking local material in recent lunar rays and is undoubtedly important to the global impact gardening rate.

Finally, high concentrations of Tycho and Copernicus secondary craters were measured for tens of crater radii from their parent craters. The best-fit N(1) densities of the Tycho and Copernicus secondary crater decreased rapidly from values of N(1) ~

10^{-2} inside of 4-6 crater radii but leveled out to N(1) values equivalent to those of 1-3.5 Ga primary crater populations [*Neukum et al.*, 2001] between 6-10 crater diameters. These large numbers of distal secondary craters are consistent with the results of previous workers [e. g., *Bierhaus et al.*, 2005; *McEwen et al.*, 2005], who predicted numerous "background" secondary craters at distances of hundreds of kilometers from their parent crater. In addition, the radial profiles of secondary crater density imply large cross-over diameters between secondary and primary populations, even at large distances from the parent crater. The size-velocity distributions of the ejecta that formed these secondary craters also support the theory that distal secondary craters are launched from the parent event predominantly through spallation. Therefore, future attempts to model the production of distal secondary craters by individual primary craters should include the effects of this early-time process of crater excavation. In the meantime, the radar CPR has proven to be an excellent tool to augment our study of secondary cratering on the Moon.

REFERENCES

Arvidson, R., Crozaz, G., Drozd, R. J., Hohenberg, C. M., and Morgan, C. J., (1976), Cosmic ray exposure ages of Apollo 17 samples and the age of Tycho, *Proc. Lunar Planet. Sci. Conf. 7th*, 2817-2832.

Bierhaus, E. B., Chapman, C. R., Merline, W. J., Brooks, S. M., Asphaug, E., (2001), Pwyll secondaries and other small craters on Europa, *Icarus, 153*, 264-276.

Bierhaus, E. B., Chapman, C. R., and Merline, W. J. (2005), Secondary craters on Europa and implications for cratered surfaces, *Nature, 437*, 1125-1127.

Bogard, D. D., Garrison, D. H., Shih, C. Y., and Nyquist, L. E., (1994), ^{39}Ar-^{40}Ar dating of two lunar granite: The age of Copernicus, *Geochim. Cosmochim. Acta, 58 (14)*, 3093-3100.

Bottke, W. F. et al., (2005), Linking the collisional history of the main asteroid belt to its dynamical excitation and depletion, *Icarus, 179*, 63-94.

Campbell, B. A., Bell, J. F., Zisk, S. H., Hawke, B. R., Horton, K. A., (1992), A high-resolution radar and CCD imaging study of crater rays in Mare Serenitatis and Mare Nectaris, *Proc. Lunar Planet. Sci.Conf. 22nd*, 259-274.

Campbell, B. A., (2002), Radar remote sensing of planetary surfaces, University of Cambridge Press.

Campbell, D. B., Campbell B. A., Carter, L. M., Margot, J., and Stacy, N. J. S., (2006), No evidence for thick deposits of ice at the lunar south pole, *Nature, 443*, 835-837.

Campbell, B.A., and Campbell, D.B., (2006), Regolith properties in the south polar region of the Moon from 70-cm radar polarimetry, *Icarus, 180*, 1-7.

Campbell et al., (2010), Earth-based 12.6-cm wavelength radar mapping of the Moon: New views of impact melt distribution and mare physical properties, *Icarus, 208*, 2, 565-573.

Chapman et al., (1996), Cratering on Gaspra, *Icarus*, 120, 231-245.

Crater Analysis Techniques Working Group, (1979), Standard techniques for presentation and analysis of crater size-frequency data, *Icarus, 37*, 467-474.

Cummings, D., (1972), Geologic Map of the Clavius Quadrangle of the Moon, 1-706 (LAC-126), US Geological Survey.

Dundas, C. M., and McEwen, A. S., (2007), Rays and secondary craters of Tycho, *Icarus, 186*, 31-40.

Hartmann, W. K., (1999), Martian cratering 6: Crater count isochrons and evidence for recent volcanism from Mars Global Surveyor, *Meteorit. Planet. Sci., 34*, 167-177.

Hawke, B. R., Blewett, D. T., Lucey, P. G., Smith, G. A., Bell, J. G., Campbell, B. A., and Robinson, M. S., (2004), The origin of lunar crater rays, *Icarus, 170*, 1-16.

Head, J. W. III, (1976), Lunar volcanism in space and time, *Rev. of Geophys. and Space Phys., 14*, 265-300.

Herrick, R. R., and Forsberg-Taylor, N. K., (2003), The shape and appearance of craters formed by oblique impact on the Moon and Venus, *Meteorit. Planet. Sci., 38*, 1551-1578.

Hirata, N., and Nakamura, A., (2006), Secondary Craters of Tycho: Size-frequency distributions and estimated fragment size-velocity relationships, *J. Geophys. Res.*, *111*, E03005, doi:10.1029/2005JE002484.

Holsapple, K. A., and Schmidt, R. M., (1982), On the scaling of crater dimensions. 2. Impact Processes, *J. Geophys. Res., 87*,1849-1870.

Housen, K. R., Schmidt, R. A., and Holsapple, K. A., (1983), Crater ejecta scaling laws: Fundamental forms based on dimensional analysis, *J. Geophys. Res., 88*, 2485-2499.

Hurst, M., Golombek, M. P., and Kirk, R., (2004), Small crater morphology within Gusev crater and Isidis Planitia: Evidence for widespread secondaries on Mars, *Lunar Planet. Sci. XXXV,* Abstract 2068.

Lucchitta, B. K., (1977), Crater clusters and light mantle at the Apollo 17 site – A result of secondary impact from Tycho, *Icarus, 30*, 80-96.

McEwen A. S., Preblich, B. S., Turtle, E. P., Artemieva, N. A., Golombeck, M. P., Hurst, M., Kirk, R. L., Burr, D. M., Christensen, P. R., (2005), The rayed crater Zunil and interpretations of small impact craters on Mars, *Icarus, 176*, 351-381.

Melosh, H. J., (1989), Impact cratering: A geologic process, Oxford University Press.

Morbidelli, A., and Vokrouhlicky, D., (2003), The Yarkovsky driven formation of near-Earth asteroids, *Icarus*, 163, 120-134.

Morrison, R. H., and Oberbeck V. R., (1975), Geomorphology of crater and basin deposits – emplacement of the Fra Mauro Formation, *Proc. Lunar Sci. Conf., 6th*, 2503-2530.

Neukum G., and Wise D., (1976), Mars: A standard crater curve and possible new time scale, *Science, 194*, 1381-1387.

Neukum G., (1983). Meteoritenbombardement und Datierung planetarer Oberflachen. Habilitation dissertation for faculty membership, Ludwig Maximillians, University of Munich, Munich, Germany 186 pp.

Neukum G., and Ivanov, B. A., (1994), Crater size distributions and impact probabilities on Earth from lunar, terrestrial-planet, and asteroid cratering data, in *Hazards Due to Comets and Asteroids* edited by T. Gehrels, pp. 359-416. Univ. Arizona Press, Tucson, Arizona, USA.

Neukum, G., Ivanov, B. A., and Hartmann, W. K., (2001), Cratering records in the inner Solar System in relation to the lunar reference system, *Space Sci. Rev., 96*, 55-86.

Oberbeck, V. R., (1975), The role of ballistic erosion and sedimentation in lunar stratigraphy, *Rev. of Geophys. And Space Phys., 13,* 337-362.

Oberbeck, V. R., and Morrison, R. H., (1973), On the formation of lunar herringbone pattern, *Proc. Lunar Planet. Sci. Conf. 4th,* 107-123.

Pieters C. M., Adams, J. B., Smith, M. O., Mouginis-Mark, P. J., and Zisk, S. H., (1985), The nature of crater rays – The Copernicus example, *J. Geophys. Res., 90,* 12393-12413.

Pike, R. J., and Wilhelms, D. E., (1978), Secondary-impact craters on the Moon: Topographic form and geologic process, *Proc. Lunar Planet. Sci. Conf. 9th*, 907-909.

Preblich, B., (2005), Mapping Rays and Secondary Craters from Zunil, Mars. Thesis, University of Arizona, Tucson, 77 pp.

Robbins, S. J. and Hynek, B. M., (2011), Distant secondary craters from Lyot crater, Mars, and implications for surface ages of planetary bodies, *Geophys. Res. Letters, 38,* L052201.

Robinson, M. S. et al., (2005), LROC – Lunar Reconnaissance Orbiter Camera, *Lunar Planet. Sci. Conf. 36th*, #1576.

Robinson, M. S., Thomas, P. C., Heisinger, H., van der Bogert, C., Bowman-Cisneros, E., Denevi, B., LROC Team, (2005), Impact melts on the Moon: How far will they go, *American Geophys. Union, Fall Meeting 2010,* #P42A-02.

Schultz, P. H. and Gault, D. E., (1985), Clustered impacts – Experiments and implications, *J. Geophys. Res., 90 (10),* 3701-3732.

Shoemaker, E. M., (1965), Preliminary analysis of fine structure of the lunar surface in Mare Cognitum, in *The Nature of the Lunar Surface*, edited by Hess et al., pp. 23-77, Johns Hopkins Univ. Press, Baltimore, Md.

Vickery, A. M., (1986), Size-velocity distribution of large ejecta fragments, *Icarus, 67*, 224-236.

Vickery, A. M., (1987), Variation in ejecta size with ejection velocity, *Geophys. Res. Letters, 14*, 726-729.

Wells, K. S., Campbell, D. B., Campbell, B. A., Carter, L. M., (2010), Detection of small lunar secondary craters in circular polarization ratio radar images, *J. Geophys. Res., 115,* E06008.

Werner, S. C., Ivanov, B. A., and Neukum G., (2009), Theoretical analysis of secondary cratering on Mars and an image-based study on the Cerberus Plains, *Icarus, 200*, 406-417.

Wilhelms, D. E., Oberbeck, V. R., and Aggarwal, H. R., (1978), Size-frequency distributions of primary and secondary impact craters, *Proc. Lunar Planet Sci. Conf., 9th*, 3735-3762.

Wilhelms, D.E., (1979), Relative ages of lunar basins, *Reports of planetary geology program, 1978-1979*, 135-137.